Neuromechanical modelling of *C. elegans* **locomotion:**

proprioceptive feedback in the ventral nerve cord

Jack Denham

Submitted in accordance with the requirements
for the degree of Doctor of Philosophy

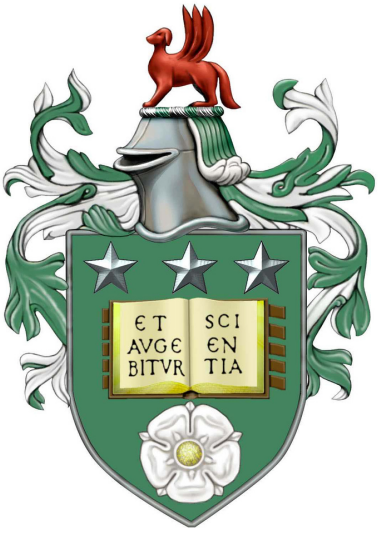

The University of Leeds
School of Computing
March 2021

I confirm that the work submitted is my own, except where work which has formed part of a jointly authored publication has been included. My contribution, and that of the other authors to this work has been explicitly indicated below. Appropriate credit has been given within the thesis where reference has been made to the work of others.

Jack E. Denham, Thomas Ranner and Netta Cohen, Signatures of proprioceptive control in Caenorhabditis elegans locomotion, Phil. Trans. Roy. Soc. B, 373(1758), 2018

My contribution: First author. Integrated neural model to existing mechanical model. Generated all simulations and figures. Majority of writing.

Other author contributions: NC and TR developed mechanical model in previous work and contributed to writing.

Chapters based on this work: Chapters 4 and 5.

Netta Cohen and Jack E. Denham, Whole animal modeling: piecing together nematode locomotion, Curr. Opin. Syst. Biol., 13, 2019

My contribution: Second author. Created the figures, and contributed to discussions and writing in each section.

Other author contributions: NC did the majority of writing.

Chapters based on this work: Chapter 3 refers to this review.

Lan Deng, Jack E. Denham, Charu Arya, Omer Yuval, Netta Cohen, Gal Haspel, Inhibition underlies fast undulatory locomotion in C. elegans, eNeuro, doi:10.1523/ENEURO.0241-20.2020, 2020

My contribution: Second author. Implemented hypotheses in computational model and generated all computational results and figures. Wrote computational methods and contributed to interpretation and results.

Other author contributions: LD, CA and OY contributed to setting up and running behavioural experiments. LD wrote majority of experimental methods and results. GH and NC contributed to writing and provided general guidance throughout.

Chapters based on this work: Chapters 6 and 7 are based on this work.

Acknowledgements

First of all, a huge thank you to my supervisors Netta Cohen and Thomas Ranner for the opportunity to undertake this project. Netta's continual support has developed my ability to think and write critically and independently, and has deepened my understanding of computational modelling and its importance. Tom's friendly and organised temperament helped me turn numerous unnecessary mountains back into molehills, while passing on valuable technical skills which has equipped me for a productive future. I would also like to thank Felix Salfelder for his invaluable presence and useful insights in the lab, and refreshing lunchtime climbing sessions.

The constant love and support from my parents has always motivated my efforts to make them proud. Thank you for always providing the most important things in life. I also thank my sister and brother-in-law Jess and Jez, and auntie Tracey and uncle Martin for all their encouragement, and for making their home my home when I needed it.

Finally, to my fellow PhD students, particularly my housemate Francesco, thank you for sharing your much needed optimism, culture and humour which helped separate work from play, and made my experience at Leeds much more than a PhD. And to the lads... you know who you are.

Abstract

The simple undulatory gait of the small nematode worm *Caenorhabditis elegans*, along with its well characterised nervous system make it an ideal organism for studying the neural control of locomotion. Smooth mechanical propagating waves propel the worm's body through a wide variety of environments as a result of both highly coordinated motor output and finely tuned body mechanics. Inspired by previous modelling efforts, I employ an updated neuromechanical model to identify the effects of neural and mechanical modulation of *C. elegans'* locomotory gait and explore underlying control mechanisms, with a focus on proprioceptive feedback in the ventral nerve cord.

I investigate interactions between body elasticity and fluid viscosity to highlight a fundamental condition for mechanically induced gait modulation, and quantitatively match this modulation with experimental results to predict the worm's material parameters under the model assumptions. By considering characteristics unique to proprioceptive neurons, I show how manifestations of internal gait modulation contrast that of external modulation.

Manipulating the strength of various inhibitory connections within the nerve cord suggest that GABAergic connections impact locomotion in qualitatively different ways depending on location. Inhibition at the neuromuscular junctions may be used to control undulation frequency across multiple environments, while asymmetric neural inhibition supports robust high frequency undulations, in line with existing model predictions.

Recent experimental work evidences simultaneous, independently driven oscillations with different frequencies along the body when anterior and posterior regions are isolated by external inhibition. By inhibiting anterior muscles in model worms, I find that purely proprioceptive control is capable of qualitatively capturing multiple frequency undulations. In such conditions the effects of neural coupling appear to dominate mechanical coupling, at least during crawling.

Contents

List of Figures

List of Tables

Chapter 1

Introduction

1.1 Neural control of behaviour

A major goal of behavioural biology is to understand the manifestation of behaviour in living organisms and its influencing factors. Behaviour involves the continuous integration of external stimuli and internal state in order for an organism to produce some sort of output, often involving coordinated movement. Generally this is a systems level question, and taking a genetics approach, studying neural networks or investigating environmental effects on animal behaviour all provide insight but cannot reveal the full picture independently. It has long been accepted that these three broadly contribute to the moulding of behaviour over time in single celled organisms, plants and animals.

Although movement is common to all organisms in one way or another, the animal kingdom offers a particular solution to sensing, processing and reacting to environmental cues; the nervous system. The size and complexity of nervous systems varies greatly, from simple animals whose entire nervous system consists of only a few hundred neurons, to more complex animals such as humans with approximately 10^{10} neurons in the brain alone. An understanding of neural activity on the cellular and circuit level is key to understanding how behaviour arises since neural networks are responsible for detecting sensory cues and generating motor output. Although large scale studies of the human brain are ongoing [127], animals with comparatively basic nervous systems provide a good opportunity to gain powerful insights into brain-body-environment interactions. Moreover, animals with a simple morphology are more tractable for modellers and provide good opportunity to explore the frontier of whole body modelling, such that theorists and experimentalists can collaborate effectively.

Significant progress has been made in the last century, with electrical recordings of neurons leading to accurate mathematical models of membrane potentials [83], and the mapping of an entire nervous system [191]. Here I intend to pick apart the brain-body-environment loop in

a simplistic yet biologically grounded case, in order to further understand the neural basis of behaviour.

1.2 *C. elegans* as a model organism

Caenorhabditis elegans was originally selected to bridge the gap between molecular biology and animal behaviour [22]. Before these nematodes were studied on mass, pioneering geneticists had established deoxyribose nucleic acid (DNA) as the container for hereditary information. The genomes of single celled organisms such as phages [57] and yeast [69] had been carefully uncovered which, in itself lead to multiple significant discoveries about how genes are arranged. However, behaviour in multi-cellular organisms remained largely untouched from the perspective of genetics, thought by some to be the most sensible way to view the underlying drives of behaviour. The study of animals through a molecular and cellular lens would be equipped to address particularly important questions such as "how do cells arrange themselves during development?" [168], "how does activity within a nervous system coordinate to produce the rich variety of behaviours observed?" [126, 198], and "how do structure-function relations within a neural circuit help shape behaviour?" [151, 12, 195].

C. elegans was an ideal organism to pursue such questions because it ticked so many boxes for biologists. With a 1mm long, slender translucent body, it is small enough to be viewed under an electron microscope yet large enough for its 959 non-gonadal cells [168] to be seen clearly through a conventional microscope [22]. Moreover, it is particularly lab friendly and quite happy to crawl along the surface of agar gel at a moderate 20 degrees Celsius, living on a diet of *E. coli*. As such, this seemingly humble creature has been the subject of intense study for the past five decades and is a model organism for genetics, aging, behaviour and neuroscience and has also influenced the development of robotics [20, 150].

1.2.1 Genetics

In addition to factors listed above, *C. elegans'* short life span and high rate of reproduction make it an ideal organism for genetic studies. An individual worm is either hermaphrodite or male and has a relatively short life cycle of approximately 3.5 days. Hermaphrodites are able to reproduce by self-fertilization such that 100% of an individual's genes can be passed on to ∼300 progeny (of which approximately 0.01% are male [185]) over a period of just a few days. This means that a single hermaphrodite worm could be the proud ancestor of 10,000 progeny in a little over a week. Together, these factors facilitate high throughput studies with strict control over genetic factors. Alternatively, reproduction involving a male can be used to produce genetic crosses, allowing for phenotypic flexibility.

An early landmark achievement was the full sequencing of the *C. elegans* genome, which paved

the way for the sequencing of the human genome shortly after. One noteworthy comparison between the two was their surprising level of similarity; the worm's genome contains approximately $21,000$ genes [63] compared to estimates of the human genome ranging between $20,000-25,000$ [42], and it is estimated that roughly 38% of the worms genes have a homologue, or human equivalent [161].

The next task, which is still ongoing, is to understand the function and phenotypic relation to each of these genes. The approach taken is basically to break the worm in as many ways as possible by silencing individual genes and observing changes in the phenotype or resulting behaviour, thus inferring the function of the gene. It is not surprising then, that the majority of the first genes to be characterised, when silenced, produced phenotypes displaying uncoordinated locomotion, and were therefore labelled "*unc*". By convention, these phenotypes are identified by contrast to the wild type strain known as N2.

A comprehensive archive of genes along with their function, location in the genome and related phenotypes can be found on the online wormbase consortium [163]. By convention, a gene name is given by three italicized letters followed by a hyphen and a number [85]. For example, the first observed mutation resulted in shorter, fatter worms than the wild type. These worms were called dumpy with corresponding gene names "*dpy-1*", "*dpy-2*", "*dpy-3*", etc., depending on which specific gene is affected. The corresponding worm phenotype is referred to similarly, except without italics and a capitalized first letter e.g. Dpy-1. In the literature, a gene may also be given with the mutant allele, signified by a lower case letter, followed by a number, all in italics e.g. *unc-49* (*e456*) [85].

Despite the ongoing success of gene-to-phenotype mapping, there is still a large gap to fill between genes and behaviour in order to gain a full systems level understanding of a multicellular organism. It is therefore essential to view *C. elegans* at the cellular and network resolution in parallel with genes and behaviour.

1.2.2 Neuroscience

The nervous system is a common feature among animals and is responsible for the sensing and processing of information and the generating of coordinated motor output. Rather fittingly then, neurons can generally be separated into the categories sensory, inter and motor, depending on their function. *C. elegans* is no exception, although one consequence of its small and compressed nervous system is that some neurons are assigned multiple roles. From a neuroscience perspective, the main advantages brought about by the worm are (i) an invariant cell lineage and (ii) a relatively small nervous system. The former allows for the comparison of neural activity between individual worms and the latter makes feasible the mapping of all neurons and their connections in order to characterise the nervous system at the cellular and synaptic resolution. In combination, these advantages also provide a platform for detailed and

informative computational models to be built, promoting a synergy between experimentalists and modellers.

White et al.'s seminal research using electron microscopy (EM) to photograph and analyse 20,000 serial cross sections of the worm represents another milestone in *C. elegans* research and neuroscience in general [190, 191]. Through this, and numerous other works including the mapping of the cell lineage by Sulston et al. using Nomarski differential interference contrast microscopy [168, 166], all 959 cells were identified and named and most synaptic, gap-junctional and electrical connections were mapped. I leave the description of the worms anatomy and nervous system structure to a later section (section 2.1) and a more thorough description can be found in the 1976 [190] and 1986 [191] White et al. papers as well as at the online consortium wormatlas: https://www.wormatlas.org/.

In the most general terms, one can infer the functionality of a neuron, or neural network, much the same way as with genes; by breaking it in many different ways. The development of laser ablation technology [13] enables the deletion of one or multiple cells, even during free behaviour, in order to compare behaviour before and after the ablation. One drawback here is accuracy. Laser ablation may also delete nearby cells, or may not fully remove the target cell. Alternatively, more recent optogenetic techniques [16, 45] are now widely utilised, in which opsins (light sensitive proteins) can be expressed in specific neurons, making them sensitive to particular wavelengths of light. This allows for fast, controlled activation or inhibition (depending on the opsin) of the cell, or even multiple cells simultaneously, for precise time periods.

Even a fully mapped connectome still does not reveal exactly how neural network activity serves its function because two individual neurons may respond differently to the same input current. Simplistically, this difference may result from the nature of a particular synaptic connection, or from the composition of ion channels embedded in the cell membrane. As well as an unprecedented control over individual neurons, other techniques allow neural activation to be recorded in real time. The transparent body of *C. elegans* lends itself to calcium fluorescence imaging [102, 32], in which genetically encoded calcium indicators are expressed in specific cells, causing fluorescence upon activation. In a controlled setting, this allows for correlations to be drawn between behaviour and the activation of particular neurons or sets of neurons. The internal dynamics of a neuron can be determined through electrophysiological setups e.g. patch clamps [157], current clamps [136, 41] or voltage clamps [39, 128]. However this is notoriously challenging in *C. elegans* due to its relatively small neurons and the worms high internal pressure [65]. Some successful attempts at voltage recordings have been made in the past two decades [133, 118, 111], which uncovered nonlinear responses to input currents previously thought to be unsupported by the genome, which lacks genes that code for voltage-gated sodium channels [11]. Uncovering the internal dynamics of a neuron can provide insights about its function,

allowing researchers to build an overall picture of network capabilities and its influence on animal behaviour. There are few organisms for which such a breadth of techniques can be so readily applied in order to make promising progress toward a complete, whole-animal understanding of neural control of behaviour.

1.2.3 Behaviour

Equipped with the full genome, cell lineage and connectome and a variety of experimental and modelling tools, the *C. elegans* community is well prepared to undertake the much broader challenge of understanding animal behaviour at the systems level. In its natural setting, *C. elegans* mostly lives in rotten vegetation while in the laboratory setting it is most often studied crawling atop an agar surface. Other assays, however, immerse the worm in droplets of water or in a shallow layer of liquid, or buffer solution. In each of these cases, the simple body morphology and elegant sinusoidal gait of *C. elegans* allows its movement to be rigorously quantified.

Despite its small size and relatively simple circuitry, the worm presents an impressive repertoire of behaviours, including mating and egg-laying [192, 40], avoidance and escape [95], and taxis towards a variety of stimuli including odours [189], heat, oxygen, light and salt [10, 184, 79, 183]. Regular locomotion involves bouts of forward crawling interrupted by regular but brief re-orientations known as omega turns. The worm can also employ the weathervein strategy during a taxis, in which slight and regular asymmetric adjustments in bending amplitude in the head and neck gradually steer the worm. Early experiments demonstrated a touch response, in which tapping the head of the worm (with e.g. an eyelash) initiates a rapid reversal followed by a pause and turn.

Simple behavioural hierarchies are apparent among the circuitry. For example, surrounding the worm with a hyperosmotic barrier (presenting the threat of desiccation) and placing food only on the other side, results in initial avoidance behaviour with an increasingly high probability of crossing the boundary over time [64]. Given that these behaviours are ubiquitous across the animal kingdom, research into such a simple organism can be seen as a gateway to understanding the underlying biological mechanisms in more complex organisms, including humans.

1.3 Why use computational models?

The formulation of models has always been an essential part of the scientific process, as the step between forming a hypothesis and generating an experimental prediction. Computational models generate predictions by reproducing an aspect of a system in a virtual environment, based on physical laws and mechanistic assumptions. In a biological context, a system may be hugely complex and depend on an intractable number of variables, but all biological systems

must ultimately obey mathematical and physical laws. The aim of a model is not necessarily to reproduce the system in all its natural detail, rather to combine the necessary elements in order to answer a relevant research question. Ultimately, it is the explanatory power that makes a model useful. Therefore, a useful model may reduce a system to the essential components required to explain an observation, and in doing so, either support a hypothesis or generate a new one prompting researchers to find previously unseen mechanisms in the real system.

An example relevant to neuroscience is the Hodgkin Huxley model which describes the membrane potential of a single neuron [83]. By mapping principles of electronic engineering to cell biology, the researchers predicted the existence of voltage gating in ion channels which were demonstrated experimentally soon after. Another example has been clearly demonstrated in recent months through the application of SIR models (Susceptible, Infected, Recovered) [9], a species of population model used to interpret data during the Covid-19 pandemic in order to assess the infection rate of the virus and inform decisions on a global scale [1, 43].

Of course, there are additional advantages to using computational models alongside experimental methods such as their low cost, high speed and perfect reproducibility. Furthermore, a modeller is afforded absolute control over a virtual environment, allowing the ability to eliminate confounding variables and focus only on those being tested, resulting in clarity and explanatory power. Modelling is not only convenient - it is an essential component of discovery.

1.4 Thesis outline

This thesis is concerned with the relative contributions of neural and mechanical factors during *C. elegans* locomotion. I take a modelling approach, and assume for the most part that *C. elegans* motor circuitry is primarily driven by proprioceptive feedback, although alternative views are also considered more briefly.

Firstly, chapter 2 covers relevant background material as a basis for the reader's understanding. This includes an overview of *C. elegans* anatomy and nervous system, followed by a description of low Reynolds number physics and a derivation of equations describing the stress experienced by bending elastic beams, which will be useful for what follows.

I then spend chapter 3 reviewing current and relevant literature, focusing separately on hypotheses for mechanisms driving *C. elegans* locomotion, and the impact of body mechanics and external fluid viscosity. This section ends with a short anthology of existing neural and mechanical models which have in some way influenced the current work.

The bulk of the thesis has been separated into three parts; I, II and III, and each contains a methods and results chapter. The first, and most substantial, methods chapter is chapter 4 which describes the full neuromechanical model used throughout the thesis. This begins by

presenting a description of body mechanics and surrounding fluid, drawing on the background material, before explaining the motor circuitry and body wall muscles, with comparisons to similar models and their assumptions. The following set of results in chapter 5 uses this model to characterise the key factors behind gait modulation and their relative effects. The study considers separately the material parameters of the body in order to predict their values in the real worm, and characteristics unique to proprioceptive neurons to compare internal and external sources of gait modulation.

Part II describes a collaborative effort with the Haspel lab (https://web.njit.edu/∼haspel/) to investigate potential roles for inhibitory connections during *C. elegans* locomotion, and is separated into experimental and modelling contributions. Chapter 6 provides an overview of experimental results and their interpretation before a modelling methods section which builds upon the previous methods to incorporate manipulations of various inhibitory connections. The role of each inhibition is then tested in the model, with results presented in chapter 7 followed by discussion.

Part III of the thesis looks into the effects of optogenetic inhibition of the worm's muscles during locomotion as a method of gaining insights as to the underlying control. Chapter 8 reviews recent experimental evidence than anterior inhibition results in simultaneous undulations along the body of multiple frequencies. In the final methods section, which builds on the methods of chapter 4, I describe my implementation of muscle inhibition over different body ranges of model worms. Under the assumption of proprioceptive control, chapter 9 attempts to reproduce elements from the aforementioned experiments to illustrate that such control is capable of supporting multiple frequency undulations.

Finally, chapter 10 summarizes the results and discussions presented throughout the thesis, and outlines potentially fruitful directions for future research.

Chapter 2

Background

2.1 Overview of *C. elegans* biology

What follows is a brief overview of *C. elegans'* anatomy followed by a slightly more detailed look at the nervous system, with particular focus on the locomotive circuitry in the body, which is most relevant to the current work.

2.1.1 Anatomy

C. elegans is a species of nematode (roundworm) and has a slender, non-segmented cylindrical body which tapers towards the head and tail. Typically an adult grows to $1-1.2\,\mathrm{mm}$ in length, with a maximum body diameter of $80\,\mu\mathrm{m}$ (figure 2.1). The body structure can generally be viewed as having an outer tube, consisting of a cuticle, hypodermis and neuromuscular system, and an inner tube which contains the digestive and reproductive systems [3].

The cuticle surrounds the body, forming a tough but flexible $0.5\,\mu\mathrm{m}$ thick shell [44] composed primarily of collagen, offering the body structural support. The cuticle appears to be mostly smooth, with many small circumferential furrows, separated by ridges called annuli [3, 44]. There are two larger, longitudinal ridges embedded in the cuticle on the left and right sides called alae which span the length of the body and are formed by the seam cells embedded in the hypodermis [162]. The hypodermis lies directly beneath the cuticle and is responsible for its secretion. Beneath the hypodermis lie 95 rhomboid shaped, striated body wall muscles (or somatic muscles) which are arranged along the dorsal and ventral sides of the body in pairs. These pairs are slightly offset, rather than contralaterally parallel, and are arranged in rows along the body as follows; dorsal right (24), dorsal left (24), ventral right (24) and ventral left (23) [167]. Excitation of these muscles along the body by motor neurons causes them to contract along the longitudinal axis, producing mechanical bends in the dorso-ventral plane. Each muscle is tethered to the hypodermis across the entire muscle, rather than at either end,

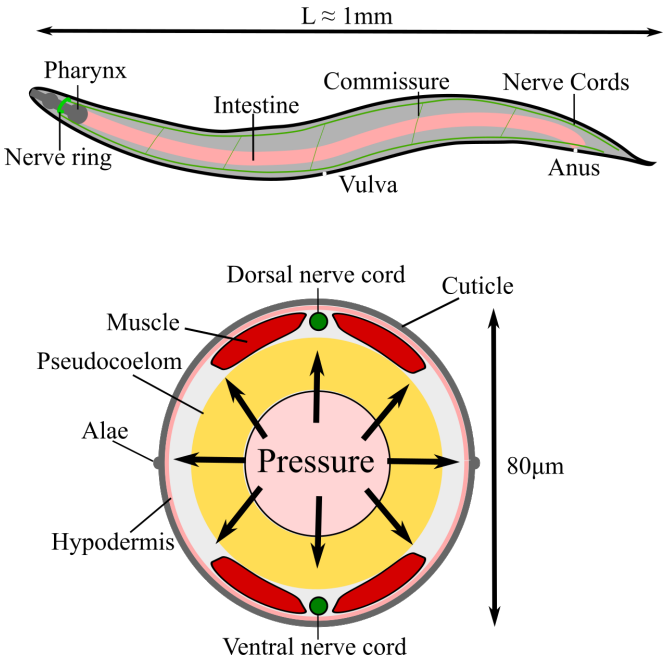

Figure 2.1: Schematic of basic *C. elegans* anatomy showing a side profile and cross-sectional view. The cuticle, hypodermis and body wall muscles are separated from an inner, pressure-filled tube by the pseudocoelom.

which is thought to prevent kinking along the body during movement [26]. The more complex musculature of the head and neck, often defined as the first four muscle pairs and second four muscle pairs, respectively, allow for both dorso-ventral and left-right bending such that the worm is capable of exploring a three dimensional space [191]. However, since the majority of experimental work studies the worm crawling on a two dimensional gel-like surface, or in shallow fluids, three dimensional locomotion is beyond the scope of the current work.

The inner tube contains a structure in the head called the pharnyx, which is shaped like two hollow bulbs connected by a hollow tube. Bacteria are sucked into the pharynx which pumps four times per second during feeding [4], passing food on to the intestine which spans the majority of the body length, ending at the anus at the base of the tail. The inner tube and surrounding pseudocoelom (the volume separating the inner and outer tubes) both contain high hydrostatic pressure which also helps maintain the worms shape [65]. Indeed, even anesthetized worms when forced into a "C" posture will relax back into a straight line upon release [159], although the relative contributions of the internal pressure and the outer shell stiffness on the straightening are not well understood [142].

2.1.2 Nervous system structure

The seminal work on *C. elegans* cellular composition and connectivity was detailed in two papers by White et al. [190, 191], in which electron micrography (EM) was used to image progressive cross sections of several hermaphrodite worms. Through this, 959 non-gonadal cells were identified and the majority of the 302 neuron connectome was mapped. It was not until many years later that the posterior section of male worms were imaged, revealing a more extensive nervous system of 383 neurons, 144 of which appear to be dedicated to mating behaviour [91]. Since male worms are much rarer than hermaphrodites, they are less studied. The model presented in the current work is based on research into the hermaphrodite nervous system, though it is likely that the motor circuitry governing forward crawling (and non-mating behaviours) is similar in the male worm. The hermaphrodite nervous system can be separated into the pharyngeal nervous system which contains 20 almost entirely isolated neurons and regulates the pumping of the pharynx, and the other 282 neurons of the somatic nervous system which occupies the rest of the body [3, 191]. White et al. took a conservative approach in their reporting of synaptic and gap-junctional connections, but since then further efforts to fill in gaps in the connectome have been made by re-analysing the EM slides and White's notes [33, 179]. Thus far, the wiring diagram which is estimated to be 90% complete consists of 6393 chemical synapses, 890 gap junctions, and 1410 neuromuscular junctions [179]. However, detailed slides imaging 39 neurons posterior to the vulva, including 21 motor neurons do not yet exist [190]. All *C. elegans* neurons are prescribed individual two or three letter names indicating their class and position, and in some cases a number indicating their rostro-caudal position within the class [191]. There are 118 such classes, sorted based on similarities in their morphology, connectivity and putative function. For example, VB02 denotes the second ventral B-type motor neuron along the ventral nerve cord. If a class contains multiple neurons positioned with dorso-ventral or left-right symmetry, the name may be suffixed with 'D','V' or 'R','L'. For example, AIAL and AIAR denote the left and right amphid interneurons.

A large proportion of neurons are located in the *nerve ring*, an annulus structure of densely packed neural processes and soma surrounding the posterior section of the pharynx (figure 2.1), which is the closest thing that *C. elegans* has to a brain. This is mainly comprised of interneurons receiving synaptic connections from upstream sensory neurons and from one another. Within the nerve ring, multiple sensory-inter subcircuits have been identified possessing various functionalities including salt chemotaxis [90], odour detection [189] and withdrawal from harsh [31, 114] and gentle [31, 129] mechanical stimuli. The compressed nature of the connectome (as compared with mammalian circuits), and the extensive repertoire of behaviours and functionality it provides suggests that some neurons likely carry out multiple functions and that subcircuits are overlaid [38]. The subcircuits of the nerve ring influence locomotion via the five command interneuron pairs, which are among the most connected neurons in the *C. elegans* wiring diagram [191, 179], demonstrating the importance of movement to the worms

survival. These are AVBL/R and PVCL/R, most linked to driving forward locomotion, and AVAL/R, AVDL/R and AVEL/R, most linked to driving backward locomotion [31]. These interneurons extend processes down the body, forming chemical and electrical synapses with the motor neurons located in the *ventral nerve cord* (VNC), a long fibre stretching from the nerve ring to the tail (see next section). A number of head motor neurons also interact with regions posterior to the head, such as the four SAA and four SMB motor neurons which form neuromuscular junctions onto head muscles [191, 3] and extend processes beyond the neck to assist in coordinating head and body undulations and initiate turns [96].

C. elegans neurons were originally thought not to be capable of producing action potentials since the genome is absent of genes coding for voltage-gated sodium channels typically required for all-or-none responses to input [11]. Indeed, modelling efforts encapsulating the full connectome with linear nodes representing individual neurons show a proclivity for oscillations on multiple modes, some of which match undulation frequencies in the biological worm [107, 108]. This suggests that the ability to produce global oscillations may be embedded within the connectome itself. However, nonlinear calcium-dependent plateau potentials have been demonstrated by RMD head neurons, indicating bistable dynamics [133]. More recently, similar nonlinearities were detected in the B-type [118] and the A-type motor neuron classes of the ventral nerve cord [118, 61]. The internal dynamics have not yet been determined for all neurons, mainly due to small size of *C. elegans* neurons and high internal hydrostatic pressure leading to difficulties in applying current and voltage clamping techniques. Numerous modelling efforts have therefore estimated neural dynamics based on those known to have similar morphology and function [24, 25, 18, 88, 92].

The ventral nerve cord

Of all the 113 motor neurons, 75 are located within the ventral nerve cord and innervate the body wall muscles [190, 191, 3]. All soma are positioned in the ventral cord, but some extend lateral processes called *commissures* (figure 2.1) to the dorsal side, which then extend along the rostro-caudal axis to form the dorsal nerve cord (DNC) to drive dorsal muscles. The VNC motor neurons are divided into 5 classes labelled A, B, D, AS and VC. Some are categorised further depending on whether they innervate muscles on the dorsal or ventral side. There are DA (9) and VA (12), DB (7) and VB (11), DD (6) and VD (13), AS (11, all dorsal) and VC (5, all ventral). The A- and B-types are cholinergic and excitatory [155, 112], as are AS and VC [143], while the D-types are GABAergic and inhibitory [132]. Unlike the more complex circuitry of the head, cholinergic and GABAergic synapses in the body are always excitatory and inhibitory, respectively. The VC class members VC01, VC02 and VC03 solely innervate labial muscles and the latter three members innervate muscles in the tail, whereas all other motor neuron classes span the full length of the nerve cord. The processes of upstream command interneuron pairs AVBL/R and PVCL/R span the full body length, innervating B-type motor neurons via gap

junctions and chemical synapses. Likewise, the AVA, AVD and AVE pairs innervate A-type motor neurons, although the AVE process ends before the vulva [191].

Chalfie et al. were the first to explore neuron function in *C. elegans*, using laser ablation to investigate the touch pathway, including head sensory neurons, premotor interneurons, and the majority of motor neurons in the VNC [31]. Ablating the majority of A-, B- and D-type neurons, respectively resulted in worms that could readily move forward but not backward, readily move backward but not forward, and worms displaying uncoordinated locomotion in either direction. Thus the motor network can be divided into cells dedicated to forward (B-types) and backward (A-types) locomotion, and those responsible for coordinating, but not generating, mechanical waves (D-types). Of the premotor interneurons, ablating PVD or AVD affected touch sensitivity but not locomotion in either direction, whereas ablating AVB (AVA) resulted in uncoordinated forward (backward) locomotion, establishing AVB and AVA as being the primary drivers of forward and backward locomotion, respectively [31, 34]. However, to limit the number of ablations required, they studied newly hatched larvae which possess only dorsal motor neurons, but additional neurons and connections form after the L1 stage. More recent studies ablated all premotor interneurons [101, 61], finding that the worm can still generate local body bends, calling into question the necessity of upstream interneurons and placing more emphasis on downstream motor control.

Calcium imaging of both AVA and AVB during free behaviour show that these neurons do not oscillate during locomotion and instead remain approximately constant [101, 103]. This indicates that, while they may drive directional locomotion, they are not part of a central pattern generator[1] (CPG) or other pattern generating mechanism. Due to mutual inhibitory connections, the activity of AVA and AVB are anti-correlated, even in movement restricted worms, preventing forward and backward locomotion being triggered simultaneously. However, 'shrinker' phenotypes have been found following escape responses in mutants lacking inhibitory connections, where ventral and dorsal muscles contract simultaneously resulting in worms failing to undulate in either direction and shrinking longitudinally [132]. Furthermore, multiple studies also report mixed gap junction and chemical synapses between AVA and A-types which act as a current shunt, biasing neural activity toward forward locomotion [101, 117]. Calcium imaging in the A and B classes during free behaviour show dorso-ventral alternation in the B-types during forward locomotion, and a switch to dorsal-ventral alternation in A-types when the worm reversed directions (and vice versa) [101].

The inhibitory D-type neurons are not directly downstream of AVB or AVA, but are post-synaptic to the A- and B-type neurons, suggesting their role is either facilitating the switch between forward and backward locomotion, or providing contralateral inhibition [138]. The

[1] A central pattern generator is an individual cell or subcircuit capable of producing intrinsic rhythms independent of external rhythmic input.

observation that ablating VD (DD) neurons lead to ventral (dorsal) bias during locomotion supports the latter hypothesis [49]. Closer inspection of the VNC connectivity reveals that most neurons in the A and B class excite D-type neurons on the opposite side of the body, which suppresses antagonist muscle activation [191, 138]. This cross inhibition helps ensure relaxation of opposite muscles while the adjacent side is contracting, increasing bending robustness. However, unc-25 mutants, which lack the necessary enzymes for synthesizing GABA, are capable of almost wild type locomotion [132] which reduces the significance of D-types, at least during forward crawling. For a long time the AS class remained largely unstudied and so their precise role in locomotion was unknown. Recently, laser ablation studies by Tolstenkov et al. revealed that worms without AS showed increased bending amplitude and appeared less coordinated than the wild type, but was nonetheless capable of forward and backward locomotion [173].

2.2 Low Reynolds number environments

This thesis is concerned with the motion of an elongated and undulating micro-scale body within a fluid environment. It is therefore important to gain an intuition of the dominant physical effects at such scales to inform the present modelling approach.

The Reynolds number

Any body surrounded by fluid will be subject to some degree of both inertial and viscous forces. Inertial forces are those which depend on the momentum of the body, whereas a viscous force describes the friction experienced between the body and the fluid (or the fluid with itself). Consider first the simple case of a Newtonian fluid, in which the fluid displacement is linearly proportional to the force being applied. In this case, the viscous forces experienced by the body can be described by the relationship

$$F = -\mu A \frac{dv}{dy}, \tag{2.1}$$

where μ is the fluid viscosity, A is the contact area of the body applying the force and v is the velocity of the fluid at a distance y from the body. Such forces scale as $O(\mu \ell v)$, where ℓ represents the characteristic length. As the body moves through the fluid, the inertial forces it experiences satisfy Newton's second law $F = ma$, which, in the case of fluids is useful to consider in terms of mass per unit volume, or density ρ, so will scale as $O(m\ell/t^2) = O(\rho \ell^2 v^2)$. The Reynolds number is a nondimensional description of a fluid as the ratio of inertial and viscous forces and is defined as

$$\mathrm{Re} = \frac{\rho \ell v}{\mu}. \tag{2.2}$$

From this it is clear that you may experience low Reynolds number physics if either you are very small, move rather slowly or are immersed in a fluid of low density or high viscosity (or any combination of these factors). In the interest of inclusivity, this is not only limited to microswimmers. For example, a human attempting to swim through honey (with $\mu = 10^4$ Pa s, and $\rho \approx 1,400\,\mathrm{kg/m^3}$) may experience Reynolds number of order $O(10^{-1})$. Comparatively, for a bacteria propelling itself through water this number would be more like $O(10^{-3})$ [137]. The characteristic length of *C. elegans* is $\ell \approx 10^{-3}$ m. For *C. elegans* swimming in water with viscosity $\mu = 10^{-3}$ Pa·s and density $\rho \approx 10^3$ kg/m^3 undulating at roughly 2 Hz, the Reynold's number experienced would approach $\mathrm{Re} = 2$. This is just below the limit for which drag is approximately proportional to velocity [17, 5]. Similar steps can be taken for worms crawling on agar for which the effective viscosity is estimated to be approximately one thousand times that of water [17]. If the density of agar is assumed to be similar to that of water and the crawling velocity four or five times lower [14], the resulting Reynold's number estimate is $O(10^{-3})$. In these cases, a consequence of negligible inertia is that the instant a swimmer stops

exerting a force on its surroundings, motion ceases. This sets a challenge for micro-swimmers such as *C. elegans* who must constantly alter their body shape to in order to move, to locomote effectively in an energy efficient manner.

How to make progress

Making consistent and efficient progress is not an uncommon issue for many PhD students. However, microswimmers such as *C. elegans* have had many millions of years of evolution to perfect their strategy. So what are the basic requirements for progress in a low Reynolds environment?

Since progress ceases when motion stops, the total net force and torque acting on a body must be zero at all times [35]. This means that any progress made by a body in low Re can be fully determined by the sequence of shape changes the body undergoes. More than this, there are particular requirements a locomotive strategy must meet in order to make any progress at all, as laid out by Purcell's *scallop theorem* [152]. The scallop locomotes by opening its shell slowly to let water in, then closing it rapidly to push the water away, propelling it forward. However, in low Re environments where inertia is negligible, the difference in speed of the opening and closing phases would not lead to propulsion since only the overall shape change of the body matters. The opening and closing of the shell takes the body through the same sequence of shapes, only in reverse order, meaning the net progress would be zero. The lesson from this theorem is that low Re swimmers must break time reversal symmetry in order to locomote. While bacteria break this symmetry using flagella which rotate in a helical fashion, round worms such as *C. elegans* propagate mechanical waves from head to tail.

Besides temporal asymmetry, an organism must also achieve a spatial asymmetry in the resistance it experiences from the surrounding environment. For example, if a body were to move purely aperiodically to break temporal symmetry, but all body shapes retained spherical symmetry, resistance and all sides of the body would obviously cancel in any given time frame, resulting in zero progress [35]. In the examples of bacteria and worms (and almost all other swimmers for that matter), the body is long and thin such that changing shape displaces less fluid in the direction parallel to the long body axis than in the normal direction, providing a directionality in the resultant force. This second requirement is more general since it is not limited to low Reynolds environments.

Resistive force theory

Focusing now on long, thin bodies locomoting in a planar fashion in low Reynolds number environments, the next task is to sufficiently describe the force interactions involved in a tractable and parsimonious way. The Navier-Stokes equations are often used to describe bodies moving in fluids, but seem too overpowered (and computationally expensive) to describe such a specific case. The additional constraints can be taken advantage of to lead to a more reductive

formulation. One widely used formulation is *Slender body theory*, whose development throughout the 1950s is the result of many contributions including G.I. Taylor [171, 172], J. Gray and G.J. Hancock [76, 72, 71] and H.R. Wallace [182, 181]. This theory is a reduction of the Navier-Stokes equations for long and thin cylinders (width $\ll$ length) in incompressible fluids, imposing a non-slip boundary condition (fluid at the surface of the body matches the velocity of the surface exactly). Applying these assumptions results in linear force-velocity relationships in the directions parallel and perpendicular to the long body axis,

$$F_i = -k_i v_i, \qquad i \in \{\|, \perp\} \tag{2.3}$$

where $k_\|$ and $k_\perp$ are the normal and tangential drag components, respectively. For Newtonian fluid, and assuming the body shape of a prolate ellipsoid, Lighthill showed that the value of each effective drag coefficient can be expressed as

$$k_\| = L\frac{2\pi\mu}{\ln(2q/r)} \tag{2.4}$$

$$k_\perp = L\frac{4\pi\mu}{\ln(2q/r)+0.5}, \tag{2.5}$$

where L is the body length, r is the body radius and $q = 0.09\lambda$ (for undulation wavelength λ). The spatial asymmetry of environmental resistance due to the body geometry can then be expressed as the ratio of these drag coefficients $K = k_\perp/k_\|$, which in Newtonian fluids is usually $K = 1.5$ and cannot exceed $K = 2$ (the limit as L$\to\infty$).

Resistive force theory, due to Gray and Hancock [71], is an approximation to slender body theory in which one discretizes a slender body and uses the $F_i = -k_i v_i$ relationship directly to estimate the force experienced at each point, instead of starting with Navier-Stokes. Then these forces can be integrated over the whole body to calculate overall motion. One potential disadvantage here, is the assumption that all of the important forces are local, neglecting any non-local fluid interactions which can arise under viscous forcing. However, comparisons between the two theories show negligible differences in the forces calculated for large amplitude undulations of slender bodies [93].

Motion in Newtonian and non-Newtonian environments

Consider a worm undulating sinusoidally with wave speed $c \neq 0$ over the surface of a homogeneous viscous fluid, such that the worm travels along a superimposed x-axis. Over a single period, any body point exerts an equal force in the positive and negative y direction, so that the worms centre of mass remains on the x-axis. However, as the mechanical wave propagates from head to tail, intuition tells us that as the wave pushes against the environment, the reactive forces from the leading edge of the wave accumulate, propelling the body forward. Importantly,

this intuition only holds for $K > 1$ (for effective drag larger in the normal component than the tangential); for $K < 1$ the body progresses in the same direction as the travelling wave, and $K = 1$ yields 100% slip such that no progress can be made. Since the least viscous fluid *C. elegans* is often studied in is water, $K = 1.5$ will be the lowest value considered in the current work. Strictly speaking, K cannot exceed 2 in Newtonian fluids, but *C. elegans* is often studied crawling across the surface of agar, or similar viscous gels. These fluids are non-Newtonian and may hold elastic properties or may be governed by some nonlinear stress-strain relationship. In this case, resistive force theory can readily approximate such viscoelastic fluids by increasing the normal component of drag such that ratio K is increased beyond $K = 2$ [72]. In fact, some estimates for drag ratio experienced by *C. elegans* have been as high as 10^4 [137].

2.3 Elastic beam models

As described in a section 2.1.1, *C. elegans'* anatomy can be crudely viewed as a hollow viscoelastic shell, filled with pressurized fluid. Towards the end of the next section I will give an overview of existing models used to describe *C. elegans* body mechanics. Some models, including the current work, elect to employ equations describing the bending of an elastic beam as a suitable approximation. Here I will briefly describe how such equations are formulated, highlighting the necessary assumptions along the way.

2.3.1 Derivation of an elastic beam

Figure 2.2 shows a section of elastic beam of length dx bending under moment M. This results in an angle of bend θ and radius of curvature ρ. The arc length of neutral axis ds does not change due to the deformation, however the arc length changes with rod depth y such that the outer arc length ds' undergoes the largest positive strain. The strain, or change in rod length due to bending moment, can be written as

$$\begin{aligned}\epsilon &= \frac{ds' - ds}{ds} \\ &= \frac{(\rho - y)d\theta - \rho d\theta}{\rho d\theta} \\ \boxed{\epsilon &= -\frac{y}{\rho}}\end{aligned}$$

so that a tighter bend causes higher positive strain on the outside and negative strain on the inside of the beam.

Stress is the force per unit area of a material, and can be calculated here using Hooke's law: $\sigma(y) = E\epsilon(y)$ where E is the Young's modulus of the material, and strain (therefore stress) is dependent on beam depth. To find the relationship between moment and beam depth, we can apply Hooke's law over the cross section of the beam:

$$\begin{aligned}M &= -\int_A \sigma(y) dA \cdot y \qquad \text{(apply Hooke's law)} \\ &= \int_A E\frac{y^2}{\rho} dA \qquad (dx = \rho d\theta) \\ &= \int_A Ey^2 \frac{dx}{d\theta} dA \qquad (E \text{ and } d\theta/dx \text{ constant across area}) \\ &= EI_2 \frac{d\theta}{dx}\end{aligned}$$

where I_2 is the second moment of area of the beam.

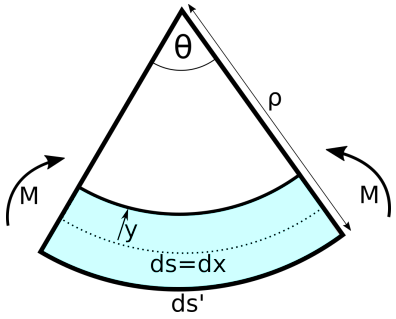

Figure 2.2: Section of an elastic beam with radius y bending under moment M. This creates a bending angle θ with corresponding curvature radius ρ. The arc length ds matches the section length dx in the centre, but is lengthened to ds' at the outer side of the rod.

Now we have an expression for the moment acting on the beam, given it's geometry I_2 and material properties, we can easily invert this relationship to find the slope (or bending angle) of the beam along its length. So, rearranging the above equation to isolate $d\theta$ and integrating gives

$$\theta(x) = \int \frac{M(x)}{EI_2} dx. \tag{2.6}$$

As a standard result in calculus, line curvature can be expressed as follows,

$$\begin{aligned} \frac{d\theta}{dx} = \frac{1}{\rho} &= \frac{d^2y/dx^2}{(1 + (\frac{dy}{dx})^2)^{3/2}} \\ &\approx d^2y/dx^2. \end{aligned}$$

So now we can express the moment about the neutral axis of a beam as a function of curvature $\kappa(x)$, taking into account the material properties and geometry of the beam:

$$\boxed{M(x) = EI_2\kappa(x).} \tag{2.7}$$

Chapter 3

Related literature

The previous section outlined important aspects of the worms anatomy and nervous system. What follows is a review of more recent literature covering key topics and experimental and modelling work relevant to the thesis. Some of the following is inspired by the Cohen and Denham review "Whole animal modeling: piecing together nematode locomotion" [36].

3.1 Network topology and structure-function relations

Upon general inspection, the *C. elegans* connectome follows similar rules and structures as vertebrate nervous systems. Both display hierarchical structure, with global networks arranged into modular subnetworks [105, 178, 134]. *C. elegans* connectivity shows an element of small worldness, with a combination of high local network clustering and high average path length between pairs of neurons compared to randomly generated networks with identical network size and modularity [105]. Small world network topology typically encourages fast communication between nodes, utilising a relatively small number of connections [186], however, the comparatively high average path length suggests that the connectome may not necessarily be optimised for signal speed. Despite high local clustering, *C. elegans* circuitry is not without a degree of central control. The connectome contains of a small number of hub neurons known as the 'rich club' [105, 174] which are disproportionally connected, and inter-connected, providing a great deal of coordination between specialised subcircuits. Both small-world and rich-club organisation have also been identified in the high level connectivity in the human brain [178], indicting their importance to nervous systems in general. Specifically, the *C. elegans* rich club (figure 3.1) consists of nine neurons, five of which are the command interneurons [105, 174] responsible for driving forward and backward locomotion via electric and chemical synapse in the ventral nerve cord. Of the other rich club neurons (figure 3.1), AIB and RIB are first and second layer interneuron pairs responsible for processing chemosensory information and odor detection [176, 180, 30, 3]. RIA is strongly linked with thermotaxis [86] and DVA is a

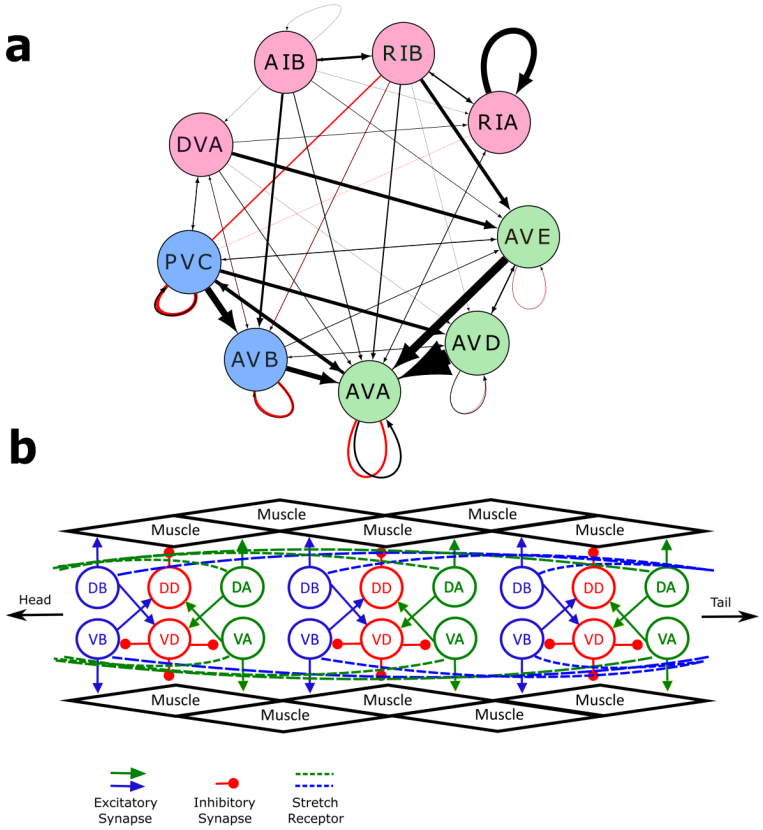

Figure 3.1: (a) Rich club neurons adapted from Towlson et al. [174] including synaptic (black) and electrical (red) connections which promote sensorimotor coordination. Arrow thickness represents the number of synapses between neurons. Blue and green nodes display forward and backward command interneurons, respectively, and pink nodes display upstream sensory/inter neurons. (b) Simplified ventral nerve cord motor circuitry for *C. elegans* locomotion, showing the symmetry between the forward and backward circuits including postulated neural inhibition on the ventral side [18] and stretch receptors.

mechanosensory neuron spanning the body length and regulating bend amplitude [193, 113]. The prevalence of premotor interneurons in the rich club indicates a strong direct coupling between sensory information and motor output [36] and the importance of goal directed locomotion to the worms survival. However, the lens of network topology alone is insufficient to fully elucidate the relationship between network activity and posture control.

Yan et al. [175, 195] take a control theoretic approach to ask how many body wall muscles can be controlled independently. Using a connectome-based linearized model, thus constrained by gaps in connectomic data [33, 179], they found that of the 95 body wall muscles, 89 are independently controllable. Of the 118 neuron classes, only 12 of these classes reduce controllability when ablated and only one of these is not contained within the locomotion circuitry [33, 179, 195]. This suggests robustness in control of the somatic muscles and strict functional partitioning between upstream sensory input and downstream motor control. Although such a high level of controllability suggests a huge number of achievable muscle activation patterns during movement, wild type worms seldom deviate from smooth wave propagation, even throughout the rich repertoire of observed behaviours. This discrepancy between high controllability and observed low-dimensional behaviour suggests that additional factors are at play, for example, the model perceives the nervous system as a directed network with linear nodes and a single governing timescale.

Connectome-based models with linear neurons and nonlinear synapses with a range of timescales have been shown to produce neural output restricted to a small number of dynamic modes [107, 108], some of which display sustained oscillations. This suggests that the connectome structure itself lends itself to particular resonances. Furthermore, statistical analysis of body postures during free behaviour resulted in 95% of postures being reached through combinations of only four principle components, dubbed eigenworms [21, 164]. The use of eigenworms has become a powerful and widely used tool among *C. elegans* researchers. For example, the use of eigenworms contributes to fingerprinting methodology in order to identify different strains of wild type and mutant worms [21, 197, 23]. It has also been used to identify a novel manoeuvre called a *delta turn*, which is behaviourally independent to the previously identified omega turn, suggesting overlaid and multiplexed functionality within the motor circuit [21]. Finally, eigenmodes have proved useful in analysis of neural recordings to demonstrate a close relationship between global neural states and behaviours, with a fairly consistent and predictable directionality between global state switches [100, 97].

3.2 Control paradigms for *C. elegans* locomotion

In order to generate a smooth sinuous gait, *C. elegans'* nervous system must generate oscillations that achieve both robust dorso-ventral alternation and propagation along the body with the

correct phase lag [38, 66]. Despite a rather comprehensive knowledge of the worms connectome [190, 191, 33, 179] and functionality within the motor circuit [31], the neural mechanisms behind wave generation, alternation and propagation are not fully understood. Research over the past few decades has collectively condensed this problem into three hypotheses, laying out potential paradigms for neural control of locomotion [66]: (i) the motor circuit is driven and coordinated by proprioceptive feedback (ii) a head CPG initiates a bending wave which is propagated by proprioceptive feedback (iii) multiple CPGs along the body generate body bends which are then coordinated by proprioceptive mechanisms.

The proprioception hypothesis originated from a personal communication to John White from Russell [190], who suggested that the long undifferentiated asynaptic processes extending from the B-type neurons may detect cuticle stretch in order to generate a current. Niebur and Erdös were the first to test this hypothesis in a computational model [52, 137], showing that proprioception is capable of supporting propagation of oscillations initiated by a head CPG. This was in contrast to a previously held hypothesis that AVB interneurons propagate a wave of excitation which stimulate motor neurons, since biophysical parameter sets rendered neural propagation speeds orders of magnitude higher than observed mechanical waves [52]. There is now strong experimental evidence that the entrainment or phase coordination of oscillations requires proprioceptive feedback [59, 188]. By imposing different midbody curvatures using a physical clamp, Wen et al. [188] showed that the curvature of neighbouring body regions were co-dependent, with posterior regions matching imposed anterior curvature after a short delay, which depended upon the viscosity of the surrounding fluid. Furthermore, when imposing zero curvature using a microfluidic channel of varying length, they found that only clamps of length $\geq 200\mu$m prevented anterior undulations from continuing past the clamp to the tail. Optogenetic silencing of the A-type, B-type or D-type motor neuron classes resulted in suppression of posterior undulations during forward crawling only when silencing the B-types [59]. Together, these findings indicate that posterior regions follow anterior regions with an effective proprioceptive range $\leq 20\%$ of the total body length via proprioceptive activation of the B-type motor neurons [188, 59]. This does seem surprising, however, since the undifferentiated regions of B-types are directed posterior to the somas [190]. Healthy anterior bending is displayed by *vab-7* mutants, whose dorsal B-type neurons have anterior rather than posterior facing processes [53], but show a ventral bias in the tail, alternating between zero curvature and a ventral bend. During clamping, posterior regions in *vab-7* mutants only follow ventral bending and not dorsal [188]. This reinforces the stretch driven hypothesis since reversing stretch receptor directionality would radically shift the phase of periodic forcing, which proprioceptively driven models show effectively reverses the polarity of the neuron [47]. It is worth noting that questions may be raised about the effectiveness of physical clamping on disrupting the wave propagation. For example, it may be the case that physical clamping allows the worm to slip as it undulates, effectively altering the clamping width or unintentionally changing the location of clamping along the body over a period of undulation. Likewise, contraction of the muscles

along the long body axis may still be permitted, potentially triggering a proprioceptive response even within the clamped region. In more recent efforts, Fouad et al. [59] employ optogenetic techniques to effectively clamp midbody regions by inhibiting muscles and various excitatory motor neurons. These manipulations gave rise to a qualitatively different behaviour in which body regions anterior and posterior to the inhibited region undulate at significantly different frequencies, however, a more thorough discussion of these results and their implications will be revisited in chapter 8. To my knowledge, no molecular mechanisms have been identified as mediating a proprioceptive response in B-type neurons. However, transient receptor potential (TRP) channels, 24 of which are encoded by the *C. elegans* genome, have been shown to be required for activation of the DVA neuron by body bends [70, 113]. The DVA neuron runs the length of the body and *trp-4* loss-of-function mutants display abnormally deep body bends, suggesting a role for DVA in controlling body posture via proprioception. Similarly, the PVD neuron (implicated in the harsh touch response) is sensitive to body bends via the mechanically gated MEC-10 channel and also influences bending amplitude [2]. Despite these observations, extensive ablation studies show that neither neuron are required for generating coordinated body bends [61].

Multiple recent modelling efforts demonstrate the possibility of hypothesis (i) [24, 25, 18, 194, 92] (section 3.4) showing that stretch feedback is sufficient to maintain robust mechanical wave propagation even in absence of a head CPG. This does, however, require a strong nonlinearity within the circuit to ensure dorso-ventral alternation in reversals of membrane potential, whether in the stretch receptors [24, 25] or the B-type neurons themselves [18, 47, 92]. In particular, the hysteresis inherent in such dynamics provides robustness to minor fluctuations in input [38]. Moreover, neural nonlinearity also helps maintain wave amplitude of undulations along the body, as compared with similar models with linear neurons [194]. Feedback driven models also have the advantage of readily producing smooth gait modulation under increasing fluid viscosity [18, 47, 194, 92], as observed by Berri et al. [14] and Fang Yen et al. [55], although to be quantitatively accurate requires the existence of very particular mechanical relationships [47] (section 3.3).

In most undulatory locomotors studied to date including leech [187, 51, 106, 126] and lamprey [104], chains of central pattern generators (CPGs) can be found in the spinal cord or nerve cord, producing endogenous oscillations which persist when removed from the body. While the CPGs are sufficient to generate body bends, they are often coordinated by sensory feedback mechanisms [135, 73, 28]. Early inspection of *C. elegans* ventral nerve cord circuitry reveal a surprisingly small number of inhibitory connections, which are typically essential for rhythm generating circuits [52, 24, 25, 18]. Instead, it is dominated by excitatory neurons and gap junctions [75]. This along with the observation that the D-type neurons, the only inhibitory class in the VNC, are not essential for body bends [31, 59, 61] weakens the hypothesis of CPG driven locomotion in the body. This is a distinguishing factor from the head circuity, which is

dominated by inhibitory connections, some of which appear to be essential for head oscillations [148, 143]. Olivares et al [139] recently considered combinations of neural motifs within the nerve cords, based on a simplified connectome [77, 78]. The resulting model, parametrized using evolutionary algorithms, is capable of supporting distributed oscillations generated by three classes of motor neurons, including the then uncharacterised AS class [139]. However, these motifs still required inhibition in order to produce oscillations, emphasising the need for either CPGs or proprioception to generate locomotive patterns. Since then, direct recordings of AS activity suggest their role is related to mediating switches between forward and backward locomotion and overall bending amplitude, rather than generating body bends [173].

In absence of any obvious distributed pattern generating motifs, single neurons may be responsible for intrinsic oscillations via auto-regulated membrane potentials [117, 198]. Current clamp studies have been performed in the backward circuit, revealing rhythmic activity in individual A-type neurons, independent of premotor interneurons or other motor neuron classes [61]. Furthermore, sparse ablation of A-type motor neurons does not fully abolish backward undulations, and an increase (decrease) in A-type activity is correlated with an increase (decrease) in backward crawling velocity [61]. These results support the hypothesis that a chain of local, perhaps single cell, CPGs drive backward locomotion in the worm, and further demonstrate an emphasis on downstream, localized control within the connectome.

Recent studies employing extensive optogenetic manipulations [59, 194] probe for intrinsic oscillators in the VNC. Fouad et al. [59] used optogenetic inhibition of the muscles and cholinergic neurons in anterior body regions in order to disable proprioceptive mechanisms from propagating body bends. This revealed a novel observation that the posterior region undulates at a significantly higher frequency than the anterior region, with lower anterior frequencies and lower posterior frequencies compared to unperturbed worms. Through systematic ablations of VNC motor neurons, the authors suggest that the B motor neuron class contains multiple distributed oscillators whose natural frequency increases along the body, which accounts for the separation of frequencies upon wave disruption near the neck [59]. However, even through careful manipulations it is difficult to separate the effects of intrinsic and proprioceptive mechanisms while the circuits are embodied. Comparing similar optogenetic manipulations in the forward [59] and backward circuits reveals a potentially key behavioural difference. Backward undulations appear to be resilient to muscle and neuron inhibition in different body regions [61], whereas during forward locomotion, inhibition in the neck and midbody result in multiple frequency undulations and tail paralysis, respectively [59]. While the former result is expected of a chain of endogenous oscillators, the latter requires further study to understand the underlying mechanisms.

3.3 Mechanics matters

Locomotion depends not only on motor output, but on a balance between mechanical forces of the body and resistive forces from the surrounding environment. Indeed, inhomogeneities in the environment have been shown to influence turning and other complex manoeuvres [123] and muscular dystrophy mutants, with weaker muscles, show significantly reduced speeds during crawling [80] and swimming [81]. Due to the worms small size and slow undulations, the worm experiences low Reynolds numbers in which the inertial forces experienced during crawling are negligible compared to the viscous forces [137, 181], so progress is halted immediately after undulations cease. This permits a simplified view of the physics using the lens of resistive force theory [171, 172, 115], in which the resistivity from surrounding fluid can be approximated by tangent and normal drag coefficients. Estimates for drag values were made as early as 1958 by H.R. Wallace [181] who measure the force required to drag glass fibres of similar size to the worm across agar. From this, early modelling efforts [137] estimated drag ratios as high as $K = 10^4$, which were later reduced to $K \leq 200$ [17, 18]. Even the higher end estimates were insufficient to support propagating waves in absence of internal activation of muscles along the body [137], suggesting that waveform is not solely shaped by the groove left by the head in agar.

Studies also demonstrate coordinated wave propagation in much less viscous media such as water and buffer solutions [144, 130, 14, 55, 81], resulting in fast dorso-ventrally alternating C-shaped postures. Goal directed behaviour such as chemotaxis has been demonstrated in water [122] suggesting that head circuits are well adapted to both crawling and swimming. Placing worms in environments with incrementally increasing gelatin concentrations reveal a smooth, rather than discontinuous, gait transition between water-like and agar-like environments, with the former yielding a frequency of 1.6 Hz and wavelength of 0.65 times the body length [14]. This not only demonstrates a strong influence of the environment on behaviour, but suggests that a single neural circuit is responsible for driving locomotion throughout the transition. Increasing the viscosity of Newtonian fluid, with drag ratio approximately fixed at $K \approx 1.5$, over three orders of magnitude (10^1 and 10^4 mPa·s) show a similar gait transition [55]. Several viscoelastic rod models suggest that the primary benefit of this transition is to maintain thrust [55, 37]. Throughout the transition, the maximum angle of attack (the angle between locomotion velocity and midline tangent), shown to be proportional to thrust, remains approximately constant [55]. Furthermore, parameter sweeps of undulation wavelength and fluid viscosity in a feedforward mechanical model show that the wavelengths which give rise to optimum speed negatively correlate with viscosity [37], closely matching observed values [14]. In both high [177, 84] and low [55, 47] Reynolds number swimmers, phase lag between peak muscle torque and peak body curvature increases in more viscous environments, particularly towards the posterior. When muscle forces are low relative to fluid forces, this phase lag may admit zero or negative work in the muscles during the lengthening phase, which may increase the energy efficiency of

locomotion [177].

Understanding the interplay between neural activity and environment depends heavily on the material parameters of the body. From the anatomy, significant mechanical contributions come from the elasticity of the cuticle and muscle [55, 169, 142, 7, 8, 37], internal viscosity of the body [169, 7, 8], internal hydrostatic pressure [65], and activation-dependant muscle tone [146]. Beyond determining the mechanical manifestation of motor command, the material parameters are also shown to impact the sensitivity of mechanosensory neurons [145]. In *C. elegans* research, the understanding of the relative contributions of these factors is developed through iterations between modelling and experimental efforts.

The worms outer shell broadly consists of 3 layers; cuticle, hypodermis and muscle, each of which may contribute to an overall passive resistance to body bending. As with most biological material, each layer may contribute both elastic and viscous effects during free behaviour, and separating the effects of each layer when taking measurements can prove difficult. Park et al. [142] used a peizoresistive displacement clamp to find test force-displacement relationships of the cuticle, estimating a Young's modulus of 380 MPa. They also note a linear force-displacement relationship and very little variation between the head, midbody and tail, suggesting that it is sufficient to model the worm as a pressure-filled, uniform elastic shell. Puncturing the body to reduce internal pressure reduced the Young's modulus by $\approx 20\%$, suggesting that although hydrostatic pressure does contribute overall, the bulk body properties are dominated by the outer shell [142]. Using a viscoelastic beam model with an imposed muscle activation profile, Sznitman et al. [170] fit values of bulk elasticity and viscosity to videos of freely locomoting worms. This resulted in a much lower estimate for the Young's modulus at ≈ 3.77 kPa, with a cuticle viscosity of $\approx -860\,\mathrm{Pas}$, arguing that the negative value indicates that body tissue is generating, rather than dissipating, energy. Fang-yen et al. [55] also use a viscoelastic rod model following Guo and Mahadevan [74] to reach a much higher estimate of 13 MPa, but this is still an order of magnitude smaller than the Park et al. measurements [170]. However, since these are modelling estimates, they greatly depend on the estimated resistance from the environment, and the imposed muscle activation profile. Finally, more recent experiments by Essman et al. use the relatively new technique of atomic force microscopy (AFM) in an attempt to measure the Young's modulus of the outer layer (the cuticle), repeating measurements throughout the worms lifespan [54]. They find estimates of roughly 500 kPa for 1-5 day old worms, which decreases linearly to 50 kPa for 15-18 day old worms. Though this is also lower than earlier experimental estimates, the addition consideration of the muscles may increase bulk elasticity. Furthermore, the roughness of the cuticle increases with age due to deformations of furrows [54], which may increase the effective drag experienced from the environment.

The body wall muscles, also appear to contribute to overall stiffness [146, 145]. Petzhold et al. used both optogenetic and pharmacological manipulations of the muscles to contract and relax

all muscles simultaneously [146]. Using measurement apparatus consistent with Park et al. [142] to measure elasticity yielded a 20% increase in stiffness after forced contraction compared with before. This resulted in a 40-fold decrease of previous Young's modulus estimates to 10 MPa [146]. The same treatment was given to worms with *dpy* and *lon* mutations, which disrupt genes involved in the construction of collagen proteins, which primarily form the cuticle, dramatically altering the body shape [94, 3]. 'Dumpy' (dpy) mutants are shorter and fatter than wild type worms whereas 'Long' (lon) mutants are longer and thinner. Results showed that *dpy* mutants are fractionally more than half the wild type stiffness, while the stiffness of *lon* mutants is only slightly lower than that of wild type, showing that although of the cuticle structure significantly impacts the material properties, the dimensions of the worm also determine bulk elasticity. In particular, Rahman et al. [153] report that body diameter, not length, strongly affects muscle strength.

Although experimental work sees the worm placed in many environments including water-like media [144, 130, 122, 147, 135, 6, 81], and micropillar arrays [48, 81], the majority of studies to date take place on the effectively two-dimensional surface of agar gels. This approach narrows our view of worm behaviour and may miss key behavioural markers revealing mechanisms behind neuromechanical control. For example, the neuromechanical model due to Boyle et al. [17, 18] proposes an additional role for D-type inhibitory motor neurons. In addition to suppressing muscles of the non-contracting side, D-types may also inhibit B-type neurons on the ventral side in order to avoid simultaneous activation of dorsal and ventral muscles during forward movement (figure 3.1). Crucially, the model predicts no behavioural change for GABA deficient mutants in agar-like environments, but severely uncoordinated, shrinker-like behaviour in water, in which muscles on both sides contract causing paralysis. Either faster undulation timescales, longer waveform or difference in neuromechanical phase lag leads to unique manifestations of deficient neural mechanisms. A range of fluid viscosities were also used in optogenetic inhibition studies inspired by Fouad et al. [59, 194]. Here, Xu et al. inhibited cholinergic neurons in the neck to test the effect on gait modulation, showing that midbody frequency showed very little modulation when decoupled from head oscillations [194]. This points to a hypothesis in which fixed frequency posterior oscillators are entrained by slower head oscillations. Finally, gait modulation studies in Newtonian media [55] reveal a saturation in both frequency and wavelength at lower and higher limits of fluid viscosity, indicating separate kinematic regimes in which the force-balance is dominated by either physical or neuromuscular timescales. These results serve to guide future estimates of material properties and increase our understanding of brain-body-environment interactions and paradigms of neural control.

	Description	Reference	Value
Environment			
	Drag coefficients (water)		
	$(k_\parallel, k_\perp)$	[115, 18]	$(3.3, 5.2)\cdot 10^{-3}$ kg m^{-1} s^{-1}
	Drag coefficients (agar)		
	$(k_\parallel, k_\perp)$	[181, 18]	$(3.2, 128)\cdot$ kg m^{-1} s^{-1}
Anatomy			
	Body length	[191]	1 mm
	Cuticle width	[142, 170]	0.5 μm
	Maximum radius along body	[191]	40 μm
Material parameters			
	Young's modulus (E)	[142]	380 MPa
		[170]	3.77±0.62 kPa
		[55]	13 MPa
		[7]	1.3 ± 0.3 MPa
	Internal viscosity (η)	[170]	-860.2 ± 99.4 Pas
		[55]	≤ 68 kPas
Waveform			
	(Frequency, Wavelength) - water	[14, 55]	(1.6 Hz, 1.6 mm)
	(Frequency, Wavelength) - agar	[14, 55]	(0.5 Hz, 0.6 mm)

Table 3.1: Experimental and modelling estimates for physical, material and kinematic measurements related to *C. elegans*.

3.4 Summary of existing models

Since modellers first turned their attention to *C. elegans*, aspects of worm mechanics or neural dynamics have been formulated in many different ways. These include disembodied connectome-wide models [107, 195, 108, 99, 58], simplified neural models [24, 25] and purely mechanical models of the body [123, 37, 154] including particle system descriptions [156, 141]. In particular, the open worm consortium has undertaken the task of digitally recreating *C. elegans* at full 3-dimensional cellular resolution [67, 29, 158], embedded within a particle simulator for body-environment interactions [140, 141]. Indeed, the field has seen a steady evolution of models which integrate the nervous system within a mechanical body capable of interacting with a surrounding environment [137, 18, 88, 47, 92]. The purpose of this section is to recap particular models whose development has provided key insights that have, in one way or another, guided the current work.

Niebur and Erdös

Niebur and Erdös provided the first models focusing on both the mechanical [137] and neural [138] aspects of *C. elegans* locomotion. Firstly they sought to find patterns of coordinated muscle activation sufficient to produce thrust in a resistive environment. Their purpose was to formulate equations describing the more significant physical forces acting on the worm body. This included internal hydrostatic pressure, cuticle elasticity, active contractile forcing from

the muscles and drag forces due to the surrounding medium. The simple mechanical model has realistic dimensions (80 μm diameter and 1mm length) and is comprised of a series of rectangular units formed by pairs of laterally connected springs, although the body radius is constant rather than tapered. Lateral springs in the ventral and dorsal sides represent cuticle elasticity and contralateral springs connecting them provide a fixed internal pressure. Strong resistive forces ($K = 10^4$) represent a stiff groove in an agar surface such that muscle actuation in the head initiates a propagating wave, and the body follows the groove created in the agar.

Initial simulations of worm locomotion saw the body straightening out after just a few undulations and ceasing to progress. To remedy this, the authors considered the hypothesis proposed by R.L. Russell (personal communication to John White), that the asynaptic distal regions of B-type processes sense body bends, stimulating these motor neurons so that bending directly posterior to the soma drives local bending. This contrasted the alternative notions that upstream inter neurons impose global control over muscle activation, or that the body simply follows a groove created by head undulations. Implementing this sensitivity to body bends in model worms produced sustained forward movement, indicating that muscle excitation due to proprioception is a sufficient and plausible mechanism for driving locomotion. These results set the stage for future models to further investigate the role of proprioceptive feedback in locomotion.

Following this, Niebur and Erdös took a closer look at the motor circuit, looking for a specific circuit motif to explain local control [138]. Taking from experimental knowledge including the Chalfie et al. ablation studies [31], and inspired by similar circuitry in the closely related but larger Ascaris lumbricoides [165], the authors propose a minimal network to provide stable dorso-ventral oscillations [138]. In the proposed circuit, VB and DB neurons are the primary actuators of the muscles on their respective sides, and excite DD and VD, respectively, which then inhibit muscles on the opposite side. Only B-types are excited by connections from inter neurons AVB and PVC [138], which are assumed to be continuously depolarised during forward locomotion. The establishing of the minimal circuit represents a significant contribution to our understanding of *C. elegans* locomotion, and has been inherited by a large number of more recent models.

Bryden and Cohen

Niebur and Erdös demonstrated how oscillations in the head may be successfully propagated along the body via stretch feedback in a neuromechanical framework. Following this, Bryden and Cohen produced a model intended to strip away the mechanical forces [25, 24], instead focusing on the neural circuitry within the VNC and asking whether proprioceptive feedback alone is sufficient to coordinated realistic wave propagation. The body consists of a series of line segments, between which a bending angle evolves over time depending on neural drive. The neural circuit matches the minimal neural circuit for forward locomotion proposed by Niebur

and Erdos [138], consisting of one dorsal and one ventral B-type neuron, each receiving tonic activation from AVB, and one dorsal and one ventral D-type neuron providing muscle inhibition. For spontaneous oscillations to arise, a system requires a sufficiently strong nonlinearity, which is included here in the stretch receptors. This minimal circuit uses cross-inhibition by implicit D-type neurons as a mechanism for dorso-ventral alternation and feedback of the inter-segment angle to provide wave propagation with a realistic phase lag between adjacent body segments [25, 24].

The model was incrementally built up using one, two and eleven coupled neural units, training additional parameters using fitness functions at each step. Simulations showed that circuitry with both local and posterior stretch receptor feedback is capable of propagating oscillations down the body and are robust to external perturbations. The authors report that local feedback provides robustness to additional noise while distal feedback influences the phase lag between segments, equivalent to modulating undulation wavelength [25]. This represents a key departure from Niebur and Erdös [137] who implement only distal feedback. This addition assumes that mechanically-gated ion channels exist all along the B-type processes rather than being limited to the undifferentiated region.

Another consequence of the model is that a CPG is not required to sustain qualitatively realistic activation patterns, though this hypothesis is not ruled out. However, one concern was that the undulation frequency was unrealistically high. The level of AVB input was shown to modulate frequency, but no biologically feasible parameter sets were found to lower the frequency to experimentally observed values before model instabilities arose. The authors suggest that embedding this circuit in a mechanical model would reduce this frequency in a more stable manner and produce more realistic movement since body mechanics operate on slower time scales. Finally, due to the lack of mechanics, the model does not account for smooth gait modulation. However, this can be forgiven since the result had not yet been observed in the real worm.

Boyle, Berri and Cohen

The results from Berri et al. [14] showing smooth gait modulation as the viscosity of surrounding fluid was gradually increased indicated the existence of a single circuit governing forward locomotion throughout the transition. This, and similar data from Fang Yen et al. [55] showing smooth modulation in Newtonian media, represented an opportune basis for the construction of the next generation of computational models.

Inspired by Niebur and Erdös [137], Boyle, Berri and Cohen [18] constructed an articulated mechanical worm body consisting of 48 (matching the number of muscle pairs) passive lateral springs in parallel with dampers to represent the viscoelastic cuticle. Contralateral rods of fixed length set the worms radius which varies along the body to approximate the worms tapered body, and diagonal springs approximate the effect of internal pressure. Environmental drag

resists the motion of nodes connecting each lateral element, described by resistive force theory and parametrized by findings from Wallace [181] and Neibur and Erdös [137] to find appropriate drag coefficient values to represent water and agar environments (section 3.3). The passive mechanical parameters were then set by replicating the relaxation experiments of Sauvage et al. [159], in which anaesthetized worms were manipulated into a "C" posture and allowed to relax to a straight posture, measuring relaxation timescales across different fluid viscosities. Body wall muscles, also modelled as springs in parallel with dampers, apply lateral contractile forces to the passive elements upon neural stimulation. Contractile muscle forces and passive cuticle forces act on the same lateral elements to incoorporate the tethering of the muscles to the cuticle. Model muscles follow a nonlinear force-length and force-velocity relation which qualitatively agree with the Hill muscle model [82], such that the spring constant, damping coefficient and rest length all depend upon the neural activation.

The muscles are driven by twelve repeated neural segments of the core circuit [138]. However, unlike the model due to Bryden and Cohen [25, 24], the nonlinearity is placed in B-type motor neurons, which are modelled as binary bistable elements, rather than in the synapses. This decision followed the Mellem et al. [133] recordings of RMD neck motor neurons, which have a similar morphology and function to the B-types. Each dorsal and ventral motor neuron possesses separate state-dependant on and off thresholds, separated by a hysteresis band which serves to prevent arbitrarily fast state switching and provides stability. In order to initiate a state change, the neural threshold must be exceeded by the sum of input currents, which consists of a constant AVB current and dynamic proprioceptive input. Rather than using inter-segment bending angle [25], proprioceptive input is defined as the normalised difference between the rest length and instantaneous length of the lateral elements (averaged cuticle or muscle stretch). This is then summed over a range of half the body length posterior to the neuron. The neural model also includes a number of additional functions to achieve particular nuances of *C. elegans* locomotion as follows:

- Stretch receptors become more sensitive towards the posterior to account for the decrease in stretch feedback towards the tail.
- Muscle efficacy decreases linearly along the body to achieve a realistic decay in curvature amplitude
- A dorso-ventral asymmetry in stretch sensitivity ensures that the worm locomotes in a straight line.
- An additional inhibitory connection from VD to VB motor neurons acts as a neural reset such that VB does not remain activated upon DB activation.

As will be discussed a later section (section 4.1.2), some of these functions are preserved in the current work whereas others are neglected for parsimony.

This model produced numerous interesting results, but I shall limit my description to the two most relevant to the current work. First and foremost, this model was able to quantitatively reproduce the full range of experimentally observed gait modulation [18]. In particular, this was achieved without a CPG or adjusting any parameters other than environmental drag, suggesting that a single proprioceptive circuit with bistable neurons is sufficient to produce smooth gait modulation. Secondly, removal of the VD to VB inhibition within the motor circuit resulted in no significant change during crawling, but led to severely uncoordinated swimming. This suggested that this asymmetric neural inhibition may be functionally significant and increases robustness of forward locomotion in low viscosity environments. Experimentally, GABA-deficient mutants which display the shrinker phenotype should also exhibit uncoordinated swimming, or lack of undulations, in water. Boyle et al. [17] did report that GABA pathway defective *unc-25*, *unc-30* and *unc-47* mutants display uncoordinated swimming, but it is not clear whether specifically the VD to VB inhibition is responsible. More specifically, they suggest that *unc-49* may form GABA receptors in VB neurons, however, to my knowledge no conclusive results have been drawn from *unc-49* mutant swimming.

Despite the successes of this model, there remains opportunity for development. Although the model reproduces gait modulation for changing environments between water and agar, some intermediate values of drag coefficients induce uncoordinated locomotion in the model worm. Since this is not observed in wild type worms, the model may require some additional mechanism to improve robustness within these environments. Alternatively, it may be that numerical instabilities arise due to the highly non-smooth nature of the articulated mechanics, or from the binary neural control. Gait modulation in the model worm also shows non-monotonic changes in wavelength towards agar which are not observed in experiment, the cause of which remains undetermined [17].

As mentioned in section 3.3, the material properties of the worm are difficult to measure to a satisfactory degree of accuracy. A neuromechanical model could significantly contribute to *C. elegans* research by suggesting likely parameter sets for mechanical and neural properties, initiating the iterative process of narrowing down estimates through experiment and computational models. However, this model has unitless parameters which, although they represent meaningful properties, are difficult to translate into measurable quantities.

Finally, the multiple additional functions within the motor circuitry helps reproduce a more realistic waveform. However, at the current level of analysis of *C. elegans* neuromechanics, it may be more desirable to simplify the circuitry as much as possible to elucidate the source of coordinated undulations. I therefore intend to simplify this circuitry and adopt a more incremental approach, perhaps re-introducing these functions if necessary.

Ranner and Cohen

The mechanical model due to Ranner and Cohen [37, 154] forms the mechanical component of the model presented in this thesis. Therefore I will give a detailed description including a discussion about its advantages and disadvantages in the coming methods section 4.1.

Johnson, Lewis and Guy

This research [92] is a good example of how making reductive model assumptions can be useful in understanding the fundamental relationships between the competing mechanisms of a complex system. As in numerous previous models [37, 55, 98], the authors begin with a smooth viscoelastic rod description of the body mechanics and apply resistive force theory to approximate the drag imposed by the surrounding fluid. The neuromuscular circuitry is similar to that implemented in Boyle's model [18, 17], with the exception of continuous rather than binary neural states and the inclusion of gap junction connections between neighbouring VBs and neighbouring DBs. Also, rather than an extended posterior proprioceptive field [18, 17], this model implements local and anterior proprioception following Wen et al. [188] such that the local and anterior feedback have inverse polarities (mathematically equivalent to posterior feedback of matching polarity [47]). Finally, the neural circuitry is divided into six 'segments' following the connectomic analysis of Haspel and O'Donovan [77].

The model reproduces the full range of wavelength modulation under observed changing environmental viscosity [14, 55]. The model also shows that if the body timescale, defined as the ratio of internal viscosity to cuticle elasticity, becomes smaller than the timescale of muscle contraction, model worms fail to produce directionally consistent travelling waves [92]. In fact, a relatively narrow band of ratios between 0.07-1 seconds produce reliable and robust travelling waves. This highlights a key relationship between physical and mechanical timescales and emphasises the role of physics in undulatory locomotion.

To understand this relationship, the authors go one step further and reduce the neuromechanical model to a series of coupled phase oscillators. This allows the nature of coupling between body regions to be clearly broken down into three competing factors: mechanical coupling due to body-environment interactions, gap-junctional coupling between segments and proprioceptive coupling. Analysis of the individual effects of each factor on inter-segment phase difference (as a proxy for undulation wavelength) revealed that stronger mechanical coupling promotes antiphase oscillations (and therefore shorter wavelengths), while gap junction coupling synchronises adjacent segments (promoting longer wavelengths) and proprioceptive coupling pulls the phase difference toward a quarter of a cycle period (promoting a stable travelling mechanical wave). They highlight the regimes of relative coupling strengths that give qualitatively correct trends. Importantly, when the body timescale is sufficiently smaller than muscle timescale, the stable attractor of the mechanical coupling function flips from antiphase to synchrony, such

that it now promotes longer rather than shorter wavelengths. This results in an incorrect correlation between wavelength and changes in environment viscosity, and a qualitative mismatch with experiment [14, 55].

Using phase oscillator theory, this model demonstrates how the competition between neural and mechanical coupling results in wavelength modulation. As mentioned, the Boyle et al. model [18] required a physiologically unrealistic proprioceptive range to achieve larger undulation wavelengths, particularly in less viscous environments. The JLG model achieves long wavelengths, most likely due to the addition of the gap junction coupling which synchronises adjacent segments. However, as the authors point out, this model captures a significantly smaller frequency modulation ($1.6 - 1.7$ Hz), and it is possible that a larger range of undulation timescales would affect this success, since frequency and wavelength positively correlate under changing mechanical load. The model also neglects the potential effects of internal hydrostatic pressure which may also impact the body's resistance to bending and the undulation timescales [142].

Chapter 4

Methods I - A Neuromechanical model of *C. elegans* locomotion

4.1 A continuum mechanical model

The neuromechanical model of Boyle et al. [18, 17] was a valuable contribution and represented a landmark in *C. elegans* modelling, successfully combining elements of the nervous system, body mechanics and environment in order to reproduce experimental results and generate novel predictions. However, as discussed in the previous section 3.4, the model is not without certain limitations which may be remedied by using a different modelling approach. One motivation for this is to address the estimates of the body's material parameters such as cuticle and bulk elasticity, which currently vary over several orders of magnitude [55, 169, 142, 7, 8, 37]. This is not possible in the Boyle, Berri and Cohen model because the body is comprised a series of one-dimensional rods with associated unitless spring constants, not readily translatable to physical quantities. Furthermore, the Boyle et al. model [18] displayed instabilities in model worms moving through environments of intermediate viscosities (between that of water and agar). This may be due to the nonsmooth description of the body mechanics or neural activation, or may point to novel findings about nematode locomotion. Either way, investigating a model with smooth mechanics will shed light on this problem. As previously mentioned, the Boyle et al. [18] model also employs various functionalities in the neuromusculature such as a decreasing muscle efficacy along the body, increasing stretch sensitivity along the body, dorso-ventral asymmetry of neural activation and nonlinear muscle forcing. Simplifying these model components to take a more parsimonious approach could increase the predictive power of the model. Finally, and slightly less related to the current work, one motivation of Cohen and Ranner was to extend the model to include 3-dimensional behaviour [154]. Transitioning to a 3D description using articulated rods and dampers is not straight forward, whereas elastic beam models are readily extendable.

With this in mind, the current work aims to continue the study of *C. elegans* neuromechanics using an updated mechanical model put forward by Cohen and Ranner [37] which is described in detail in this section. It is worth noting that this mechanical description was recently updated by Ranner [154] to incorporate the twisting of the body, allowing for 3-dimensional motion. The full model described in this section integrates a motor circuit, inspired by Boyle et al. [18], and simple musculature to Cohen and Ranner's mechanics [37]. The resulting neuromechanical model was published in Denham, Ranner and Cohen (2018) [47] and results related to this publication are presented in chapter 5. More recently, collaborative efforts saw modifications to the neuromusculature in order to explore the role of inhibition during locomotion in parallel with experiment [46] (see chapter 6). In this chapter I first describe the mechanical model from Cohen and Ranner, [37] used throughout the thesis. I then present the neuromuscular component of the model and its integration to the mechanics, making comparisons to the circuitry of Boyle's model [18, 17]. I then describe the nondimensionalization of the full neuromechanical model, specifying the default parameter set.

4.1.1 Body and environment

Rather than articulated springs and dampers, the cuticle is represented by a smooth, continuous tapered viscoelastic shell with finite thickness, more akin to the real worm. This mechanical model supports a wide range of postures, including those with unphysical curvatures, which places a requirement on the neuromuscular component to restrict the body to manifest feasible and experimentally observed postures during locomotion.

Geometry and parameterisation

The model worms body is parameterised by $u \in [0, 1]$, the proportion along the midline from head ($u = 0$) to tail ($u = 1$) and $\boldsymbol{x}(u, t) = (x(u, t), y(u, t))$ gives the position of body at u in physical space. Unit vectors in the tangent and normal directions to the midline ($\boldsymbol{\tau}$ and $\boldsymbol{\nu}$, respectively) are defined as:

$$\boldsymbol{\tau} = \frac{1}{|\boldsymbol{x}_u(u,t)|}\frac{\partial \boldsymbol{x}}{\partial u}, \qquad \boldsymbol{\nu} = \boldsymbol{\tau}^{\perp} = (-\tau_y, \tau_x), \tag{4.1}$$

where the subscript u denotes a partial derivative and the normal vector is defined as the tangent vector rotated anticlockwise by 90°.

From this the midline curvature $\boldsymbol{\kappa}(u, t)$ can be defined as the change in the tangent along the midline,

$$\boldsymbol{\kappa}(u,t) = \frac{1}{|\boldsymbol{x}_u(u,t)|}\frac{\partial \boldsymbol{\tau}(u,t)}{\partial u}. \tag{4.2}$$

Note that this curvature points in the direction normal to the midline, so scalar curvature is written as $\kappa(u, t) = \boldsymbol{\kappa} \cdot \boldsymbol{\nu}$ and will be considered extensively throughout the thesis as a proxy

for body posture. By convention, the normal unit vector points in the dorsal direction so that positive (negative) scalar curvature corresponds to a dorsal (ventral) bend. This parameterisation allows the forces experienced by the worm to be collapsed onto the midline, reducing the problem to the displacement of a viscoelastic beam embedded in three-dimensional space. Note, however, that the binormal vector $\boldsymbol{\tau} \times \boldsymbol{\nu} = \hat{\boldsymbol{z}}$ is absent in the model equations since the model assumes zero twisting of the body, which restricts undulations to a two-dimensional surface, sufficient to capture common experimental environments such as an agar plate or shallow fluids. The body shape is a tapered cylinder with radius $R(u)$ matching that of Boyle's model, given by

$$R(u) = \bar{R}\,\frac{2\sqrt{(\epsilon+u)(\epsilon+1-u)}}{1+2\epsilon} \tag{4.3}$$

for small ϵ (which sets the width of the body at the tip of the head and tail) and maximal radius $\bar{R} << L$. This tapered cylinder approximates the outer shell of the worm (cuticle, hypodermis and muscles), which is assumed to have constant finite thickness $r_{\text{cuticle}} \leq \bar{R}$ over which the material properties are calculated. From the equation for displacement of a bending elastic beam (section 2.3), the bending moment is proportional to the second moment of area

$$\begin{aligned} I_2(u) &= \int_0^{2\pi}\int_{R^-}^{R^+} r^2\; r dr d\theta \\ &= \frac{\pi}{2}\left[\left(R(u)+\frac{r_{\text{cuticle}}}{2}\right)^4 - \left(R(u)-\frac{r_{\text{cuticle}}}{2}\right)^4\right] \\ &\approx 2\pi R(u)^3 r_{\text{cuticle}}, \end{aligned} \tag{4.4}$$

where $R^{\pm} = R(u) \pm r_{\text{cuticle}}/2$, using the approximation $r_{\text{cuticle}} \ll R(u)$. The rigidity of the body is partially maintained through high internal hydrostatic pressure p coming from the inner tube containing the reproductive and digestive systems. This is responsible for the relaxing of the body back to a straight configuration in the absence of muscle activation. The internal pressure is represented as a line tension directed along the midline, which is chosen to satisfy an inextensibility constraint $\frac{d}{dt}|\boldsymbol{x}_u| = 0$ such that the total body length is fixed at $L = 1\,\text{mm}$, approximating the size and shape of the biological worm. This, along with the fixed radius, means that a local change in length on one side of the body at u is equal and opposite to a change in length on the opposite side.

Bending moments

To initiate a body bend in the biological worm, body wall muscles on one side of the body contract while adjacent muscles on the opposite side relax, creating a net moment about the midline. In the current model this bending moment consists of a passive component $M^{\text{p}}(u,t)$, due to the mechanical properties of the cuticle, and an active component $M^{\text{a}}(u,t)$ provided by muscle forcing which are expressed in terms of midline curvature $\kappa(u,t)$ and a preferred

curvature $\beta(u,t)$, respectively. At any given point in time, the preferred curvature sets a posture that the midline curvature will then tend towards over some timescale, which will depend on the material parameters of the body and any additional constraints from the surrounding fluid.

The passive moment at u is found by calculating the total force applied over the cross sectional area, or stress. Assuming that the stress follows a linear Voigt model, a purely elastic spring and purely viscous damper connected in parallel [116], with fixed radius and no rotational deformations about the midline, the passive moment is expressed as

$$\begin{aligned} M^{\mathrm{p}}(u,t) &= \int_0^{2\pi} \int_{R^-}^{R^+} r\sigma \; r dr d\theta \\ &= \int_0^{2\pi} \int_{R^-}^{R^+} r^2 (Er\kappa + \eta r \kappa_t) dr d\theta \\ &= EI_2\kappa + \eta I_2 \kappa_t, \end{aligned} \tag{4.5}$$

where σ represents cross-sectional stress and r is the distance from the midline. Parameters E and η represent the Young's modulus and internal viscosity of the outer shell, respectively, although they may also be interpreted as bulk properties of the body since the model does not explicitly distinguish between the different anatomical layers. Furthermore, this representation of the mechanics is effectively a continuous version of the discrete model by Boyle et al. [18], where the solid and fluid properties of the cuticle resist body bends in a manner proportional to the magnitude and rate of local bending, respectively. The active moment is derived in a similar manner, with body curvature replaced by preferred curvature which represents forcing from the muscles: $M^{\mathrm{a}} = -EI_2\beta$. The magnitude of viscosity η represents the bulk internal viscosity of the body, accounting for both the muscles and the cuticle since they are deformed at the same rate due to the tethering of muscle to cuticle [26].

Locally, the forcing due to β is analogous to a time-dependent rest length in a spring, whose response is proportional to its displacement as captured by equation (4.10). Keeping with this analogy, the spring constant corresponds to the Young's modulus E which encapsulates the elasticity of the worm's outer shell. This, along with the radius of the body, determines how readily the body wall muscles can overcome external resistance. In the original formulation of the model, the preferred curvature takes the form of a travelling sine wave, where the midline curvature follows after some delay which depends upon the relative effects of the material properties and the resistance imposed by the surrounding environment. For the current work, I replace this simplistic feedforward description of the active moment with a dedicated neuromuscular model component whose output is calculated at each time point based on the current body posture, rather than imposing predetermined postures (see section 4.1.2 below).

Environment

The worm generates a net forward thrust by propagating mechanical waves from head to tail in order to push against the surrounding environment which may vary from soil, rotting vegetation and viscous gels to water or buffer solution. Collectively, the viscosity (or 'effective viscosity' for non-Newtonian media) of such environments may span several orders of magnitude, but due to the small size and relatively low undulation frequency, the physics experienced by the worm remain in the low Reynolds number regime (at most Re $\approx$ 1 in water [137]). As a consequence, the drag forces imposed by the environment can be modelled using resistive force theory, neglecting inertial effects and separating drag forces into components tangential and normal to the surface of the body:

$$\boldsymbol{F}_{\text{env}} = K_\nu v_\nu \boldsymbol{\nu} + K_\tau v_\tau \boldsymbol{\tau}, \tag{4.6}$$

where $K_\nu \geq K_\tau$ and v_τ and v_ν denote tangent and normal velocity components. The model allows *C. elegans* locomotion to be simulated in a wide range of environments by changing the value of the drag coefficients, which for the current purposes will be restricted between the values corresponding to water and agar. Using Lighthill's equations [115] (section 2.2), taking into account the dimensions of the worm and the viscosity of water ($\mu \approx 1\,\text{mPa s}$) gives

$$K_{\tau,\text{water}} = 3.3\cdot 10^{-3}\ \text{kg m}^{-1}\text{s}^{-1}, \qquad K_{\nu,\text{water}} = 5.2\cdot 10^{-3}\ \text{kg m}^{-1}\text{s}^{-1} \tag{4.7}$$

with ratio $K_{\text{water}} = K_{\nu,\text{water}}/K_{\tau,\text{water}} \approx 1.5$ as expected in a Newtonian fluid [115, 18]. The drag coefficients of agar-like environments are less well characterised. Neibur and Erdos [137] estimated the tangential drag coefficient of agar to be $K_{\tau,\text{agar}} = 3.2\cdot \text{kg m}^{-1}\text{s}^{-1}$ based on measurements by Wallace [182] of the force required to drag glass fragments of a similar size and mass to *C. elegans* across an agar surface. Later, Berri et al. [14] used video footage of *C. elegans* crawling on agar and a simple 2D mechanical worm model with an initial estimate for the ratio of normal to tangential drag, K, to iteratively minimize the discrepancy between real and model worm displacement. Through this, they estimated the drag ratio in agar to be $K \approx 40$. These estimates, combined with relation $K_\nu = K\cdot K_\tau$, result in

$$K_{\tau,\text{agar}} = 3.2\ \text{kg m}^{-1}\text{s}^{-1}, \qquad K_{\nu,\text{agar}} = 128\ \text{kg m}^{-1}\text{s}^{-1} \tag{4.8}$$

to describe an agar-like environment (Table 4.1). Given the above definitions, Cohen and Ranner then impose conservation of linear and angular momentum:

$$\begin{aligned} \frac{1}{|\boldsymbol{x}_u|}\frac{\partial}{\partial u}\boldsymbol{F_{int}} + \boldsymbol{F_{env}} &= \boldsymbol{0} \\ \frac{1}{|\boldsymbol{x}_u|}(M_p + M_a)_u + \boldsymbol{\tau}\times\boldsymbol{F_{int}} &= \boldsymbol{0} \end{aligned} \tag{4.9}$$

where internal force resultant $\boldsymbol{F_{int}} = p\boldsymbol{\tau} + N\boldsymbol{\nu}$ can be separated into tangential line tension

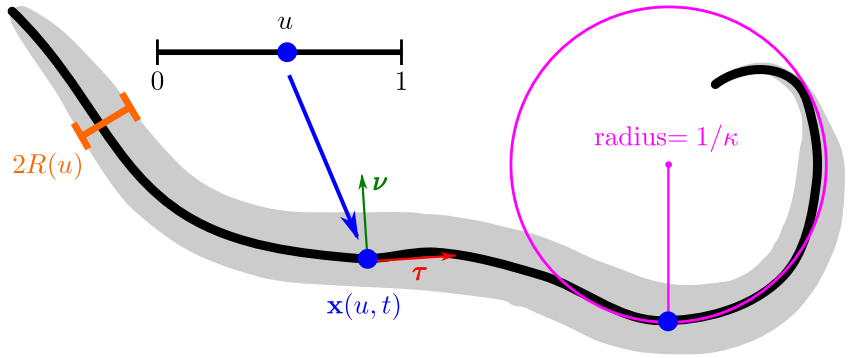

Figure 4.1: Schematic of mechanical model taken from Cohen and Ranner (2017) [37]

p and transverse shear force N [37] Combining equations (4.9) and taking into account the inextensibility constraint results in the full model equations, which balance the environmental resistance, internal pressure and viscoelastic bending moment as follows:

$$\begin{aligned} \boldsymbol{F}_{\text{env}} - \frac{(p\boldsymbol{\tau})_u}{|\boldsymbol{x}_u|} + \frac{1}{|\boldsymbol{x}_u|}\left(\frac{EI_2}{|\boldsymbol{x}_u|}(\kappa-\beta)_u\boldsymbol{\nu} + \frac{\eta I_2}{|\boldsymbol{x}_u|}\kappa_{tu}\boldsymbol{\nu}\right)_u &= \mathbf{0}\,, \\ \boldsymbol{\tau}\cdot\boldsymbol{x}_{tu} &= 0 \end{aligned} \tag{4.10}$$

where zero force and zero moment are imposed at each boundary ($u = 0, 1$):

$$\begin{aligned} -p\boldsymbol{\tau} + \left(\frac{EI_2}{|\boldsymbol{x}_u|}(\kappa-\beta)_u + \frac{\eta I_2}{|\boldsymbol{x}_u|}\kappa_{tu}\right)\boldsymbol{\nu} &= \mathbf{0} \\ EI_2(\kappa-\beta) + \eta I_2\kappa_t &= 0. \end{aligned} \tag{4.11}$$

This model formulation allowed a seamless translation between units of torque and body curvature such that bending moment can be interpreted as a direct forcing of the worm's posture.

4.1.2 Neural control

The neural drive behind *C. elegans* body bending comes from the activity of motor neurons whose cell bodies are located in the ventral nerve cord. Studies of neural ablation reveal that the only class of motor neurons essential for generating forward undulations are the cholinergic B-type motor neurons [31, 59]. Upstream interneurons, primarily AVB, tonically activate the forward circuit [31, 56]. Rhythmic patterns such as locomotion are produced by central pattern generators within the motor circuits in the large majority of organisms studied to date [51, 50, 126, 87, 15, 60]. However, there exists no strong evidence that CPGs exist within the forward locomotion circuitry of *C. elegans* [190, 33, 138, 77]. In particular, CPGs rely on neural inhibition which in the VNC could only be provided by GABAergic inhibitory D-type motor

neurons [190, 33], but generation of rhythmic body bends has been reported in worms whose D-type neurons were ablated [31, 61, 59]. The A-type motor neurons of the backward control circuit have recently been shown to produce rhythmic patterns outside of the body using whole-cell voltage clamping techniques [61]. Although there are clear morphological and connectomic symmetries between the backward and forward circuits, reversals during locomotion are infrequent, brief and are considered to be used only during escape and reorientation behaviours. Thus it is conceivable that the neurons within the two circuits may not be primarily driven by the same mechanisms or have the same dynamics. Although evidence has also been shown that B-type neurons are activated by body bending [188], the overall dominant driving mechanism in the forward circuit is not well established. Therefore, the current model accommodates the two extreme cases of purely CPG driven or purely feedback driven neural control, of which the latter is the main focus, leaving combinations of the two paradigms for future work.

Central pattern generated control

In absence of an explanatory connectome-based explanation for the existence of CPGs, I consider a minimal model in which the action of the motor circuit on the musculature is captured by continuous unit amplitude oscillations with an imposed frequency, f_f, and undulation wavelength, λ_f, propagating from head to tail. Thus, the input to the muscles is given by a travelling sine wave

$$A(u,t) = \sin(2\pi u L/\lambda_\mathrm{f} - 2\pi f_\mathrm{f}\ t)\ . \tag{4.12}$$

This choice is motivated by its simplicity, to serve as a basis for comparison between circuits whose activity is shaped by feedback from body posture, and those which simply drive body wall muscles in a regular predetermined pattern. This comparison could ultimately lead to predictions regarding the relative contribution of both control paradigms in the biological worm [47]. Cohen and Ranner used this form of drive in their model mechanics to demonstrate that experimentally observed waveforms in different environments may maximise locomotion speed, and that the material properties of the cuticle play a role in determining the optimal waveform in environments with lower viscosity but not high viscosity [37, Figure 7].

Proprioceptively driven control

B-type motor neurons are the primary excitatory motor neurons implicated in forward locomotion [31]. Here, B-type motor neurons are modelled as bistable elements, following Boyle et al. [18] and inspired by electrophysiological recordings, initially of RMD head motor neurons [133] but later from B-type neurons themselves [118]. Fitting with the continuous representation of the body mechanics and a simplistic, incremental modelling approach, the motor neuron states occupy values for all u and can be viewed as spatially continuous. Although the membrane potential of a neuron evolves continuously in time, I follow the simplifying assumption that these neurons essentially act as binary switches [18, 17] using the fact that depolarisation of

these neurons occurs over short timescales relative to the body mechanics [52, 138].

The activation of B-type motor neurons is determined by current inputs from command interneurons I_{AVB}, neighbouring motorneurons and proprioceptive input I_κ (figure 4.2). At a given time, the state of a neuron is determined by comparing these current inputs to activation thresholds. The "on" and "off" thresholds of the B-type neurons (θ_{on} and θ_{off}, respectively) are separated by a hysteresis band of finite width (figure 4.2) in order to prevent rapid state switching and allow time for the mechanics to respond to changes in neural output. Similarly, the inhibitory D-type motor neurons are made implicit in the model circuit by assuming linear dynamics on a sufficiently short timescale. Since the B-type neurons directly excite D-type neurons on the opposite side, DB and VD activity is assumed to be synchronous, as is VB and DD activity. Therefore, including the inhibitory connection from VD to VB - reported in Chen et al. [33] and shown by Boyle et al. [18] to improve swimming robustness - requires a state-dependence in the VB switching thresholds. The effects of the VD to VB inhibition, $I_{\mathrm{VD}}(u,t) = wV_{\mathrm{VD}}(u,t)$ are considered separately in a later chapter (6), but for now are neglected in favour of the simplifying symmetry argument that ventral and dorsal B-type neurons switch states simultaneously. This also comes from the fixed length assumption of the mechanical model. The neural state is therefore determined as follows,

$$\begin{aligned}
V_{\mathrm{DB}}(u,t) &\to 1 \quad \text{if} \quad I_{\mathrm{AVB}} + I_\kappa > \theta_{\mathrm{D}}^{\mathrm{on}} \\
V_{\mathrm{VB}}(u,t) &\to 1 \quad \text{if} \quad I_{\mathrm{AVB}} - I_\kappa - I_{\mathrm{VD}} > \theta_{\mathrm{V}}^{\mathrm{on}} \\
V_{\mathrm{DB}}(u,t) &\to 0 \quad \text{if} \quad I_{\mathrm{AVB}} + I_\kappa < \theta_{\mathrm{D}}^{\mathrm{off}} \\
V_{\mathrm{VB}}(u,t) &\to 0 \quad \text{if} \quad I_{\mathrm{AVB}} - I_\kappa - I_{\mathrm{VD}} < \theta_{\mathrm{V}}^{\mathrm{off}}
\end{aligned} \tag{4.13}$$

where $V_D, V_V \in \{0,1\}$ and neural inhibition strength $w = 0$. Since the AVB command interneuron activation is approximately constant during forward locomotion [101, 103], this current can be absorbed into the switching thresholds. When the proprioceptive input $I_\kappa(u,t)$ (equation (4.16)) surpasses an on (off) threshold, the adjacent neuron switches on (off). The symmetry assumption means that $\theta_{\mathrm{on}}^V = \theta_{\mathrm{off}}^D$ and $\theta_{\mathrm{off}}^V = \theta_{\mathrm{on}}^D$, making state switching simultaneous on both sides of the body. Otherwise, the neural inhibition with strength w effectively raises the VB on threshold upon activation of DB which, for sufficiently large w, prevents VB activation from occurring. If $V_{\mathrm{VB}} = 1$ when DB is activated, raising the off threshold causes VB to become deactivated, thus implicitly providing the role of the VD inhibition (see section 6.3).

Modelling the motor circuit as a continuum is a choice intended to simplify the model and focus on the workings of the neuromechanical feedback loop during locomotion. This also comes with the advantage of spatially smooth muscle activation which facilitates the calculations of gait kinematics as compared with implementing a small number of discrete neural units. It should be noted that this choice is not biologically grounded since neurons are discrete elements and

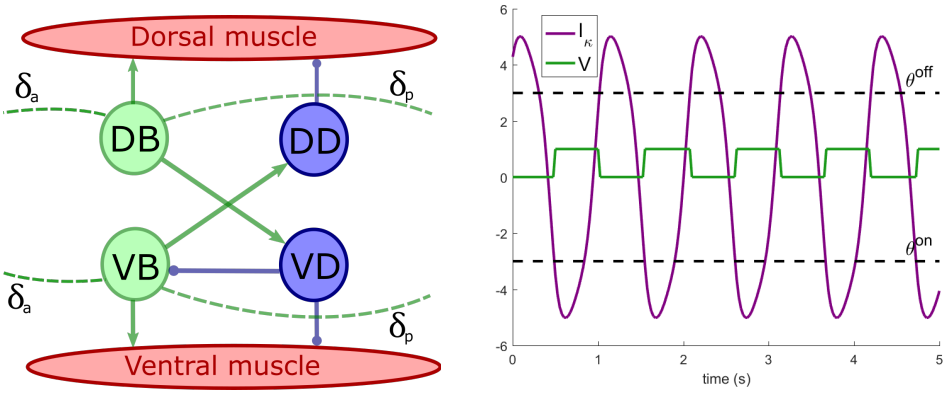

Figure 4.2: Left: Schematic of a single unit of the forward locomotion motor circuit of *C. elegans*, including cholinergic B-type neurons, GABAergic D-type neurons and body wall muscles. Right: Traces of neural activation for a B-type neuron when driven by proprioceptive input. Dotted lines represent on and off thresholds.

the B-type class is asymmetric, with 11 neurons on the ventral side and 7 on the dorsal side [190]. This description of the motor circuit is therefore not fit to address questions regarding the impact of this asymmetry on locomotion. Discretising the neuromusculature is a feasible step within the mechanical model framework, but with this step comes additional decisions about the locations of the neuromuscular junctions. One may opt to implement connections based on the known connectome (which is not yet complete [179]) or to assume that each neuron drives a small number of adjacent muscles, in keeping with assumptions made by multiple existing models [18, 92].

Proprioceptive current

In previous models proprioceptive input is formulated as a muscle or cuticle stretch summed over a body region [18] or as a function of bending angle between adjacent body segments [24, 25]. In the fixed radius geometry of the current mechanical model, this measure of stretch can be reformulated as a measure of curvature, which allows the use of the midline parameterisation of the body. In fact, during forward locomotion the undulation wavelength and curvature amplitude typically scale with body size (during development for example) [98], suggesting that the neural sensing of posture scales similarly such that relative, rather than absolute length is the important factor. Midline curvature captures such length-invariant deformation due to stretch along the body when normalized by the length over which such curvature is detected. Accordingly in this model, the total proprioceptive input current $I_\kappa(u)$ is given by the mean body curvature over a specified proprioceptive range, represented as a fraction of the body length. The model accommodates the possibility of proprioceptive input from both posterior and anterior body regions, labelled $I_{\kappa,\mathrm{p}}(u)$ and $I_{\kappa,\mathrm{a}}(u)$, respectively. The posterior

input current, which matches that used in the published model [47], is defined as

$$I_{\kappa,\mathrm{p}}(u) = \frac{\int_u^{u+\Delta_\mathrm{p}} \kappa(u')|\boldsymbol{x}_u(u')|\,\mathrm{d}u'}{\int_u^{u+\Delta_\mathrm{p}} |\boldsymbol{x}_u(u')|\,\mathrm{d}u'} \qquad \text{where} \qquad \Delta_\mathrm{p}(u) = \begin{cases} \delta_\mathrm{p} & \text{if} \quad u < 1-\delta_\mathrm{p} \\ 1-u & \text{if} \quad u \geq 1-\delta_\mathrm{p}. \end{cases} \tag{4.14}$$

Here, the proprioceptive range $\Delta_\mathrm{p}(u)$ is set to a constant δ_p along a large proportion of the midline, however, towards the tail the range decreases linearly with u since there is no bending to detect posterior to $u = 1$. Similarly, anterior proprioceptive current is defined as

$$I_{\kappa,\mathrm{a}}(u) = \frac{\int_{u-\Delta_\mathrm{a}}^{u} \kappa(u')|\boldsymbol{x}_u(u')|\,\mathrm{d}u'}{\int_{u-\Delta_\mathrm{a}}^{u} |\boldsymbol{x}_u(u')|\,\mathrm{d}u'} \qquad \text{where} \qquad \Delta_\mathrm{a}(u) = \begin{cases} u & \text{if} \quad u \leq \delta_\mathrm{a} \\ \delta_\mathrm{a} & \text{if} \quad u > \delta_\mathrm{a} \end{cases} \tag{4.15}$$

The total input current to a B-type neuron is then defined as

$$I_\kappa(u) = -I_{\kappa,\mathrm{a}}(u) + I_{\kappa,\mathrm{p}}(u). \tag{4.16}$$

The input current represents the effective stretch of each side of the body arising from dorso-ventral bending. As a consequence of calculating proprioceptive input using midline curvature, rather than muscle or cuticle stretch as in the Boyle, Berri and Cohen model [18], dorsal and ventral neurons are polarised by a proprioceptive input of opposite signs, therefore a convention is required to set the dorsoventral directionality. By convention of the model, positive curvature κ and positive preferred curvature β both correspond to dorsal bending, whereas negative values correspond to ventral bending. Unless otherwise stated, I will limit the proprioceptive range to be strictly posterior, consistent with the observed B-type morphology [190] and Boyle et al. [18]. Anterior facing processes are found in the A-type motor neurons associated with backward locomotion [191, 31, 61], which are not the focus of the current work.

Note that equations (4.14) and (4.15) state that sensitivity to body posture is uniform along the B-type processes. It is worth noting that the original proprioception hypothesis postulated that stretch receptors are only found on the distal ends of these processes. The neural model of Bryden and Cohen [24, 25] adhered to this notion and was capable of producing sustained oscillatory neural activation with realistic phase lags. However, the neuromechanical model of Boyle et al. was not able to reproduce gait modulation without an extended proprioceptive field. Assuming the existence of stretch receptors along the entirety of the B-type processes may be reasonable, as is the possibility that their sensitivity decreases further from the cell body, or is at least non-uniform. Furthermore, precisely how the distribution of sensitivity along the processes might impact the locomotive gait is not well understood. The current model is well equipped to shed light on this question by altering the above equations, for example, by taking a weighted average of midline curvature which decreases linearly with distance from the soma. There are numerous possible ways to implement this, all of which require introducing at least

one additional free parameter. Due to this and a lack of experimental data, I have opted to keep the neural model as simple as possible and leave such questions to future modelling efforts.

On a similar note, equation (4.16) appears to suggest that the input current generated by anterior proprioception is either inhibitory, or sensitive to stretch on the opposite side of the body. As demonstrated in Denham et al. [47], restricting the proprioceptive field to be anterior only (as in A-type neurons) and setting this current to be positive produces healthy backward locomotion in the model. Thus, if the proprioceptive field is bidirectional and the polarity of anterior and posterior receptors are the same, the resulting mechanical waves disrupt one another, leading to unhealthy locomotion and zero net progress. Imposing a negative current here contributes positively to the overall proprioceptive input current since switching both the polarity and directionality of the receptors is mathematically equivalent (except at each extreme of the body). Again, experimental data on the location and polarity of stretch receptors in these neurons is lacking.

The imposed anti-phase activation of the motor neurons means that the neural activation of the muscles at position u can be reduced to the difference between the dorsal and ventral activation

$$A(u,t) = V^{\mathrm{D}}(u,t) - V^{\mathrm{V}}(u,t) = \pm 1,$$

which is consistent with previously mentioned models [24, 25, 18, 89, 92]. This activation then feeds into equation (4.17) to drive the muscles.

Body wall muscles

The model muscles serve as an interface between the neural and mechanical model components. For simplicity model muscles respond linearly to the current input received from the motor neurons in order to output the muscle torque $\beta(u,t)$, which acts directly on the viscoelastic shell. The model does not distinguish between muscle torque and preferred curvature since the muscles of the biological worm are tethered to the inside of the cuticle [27]. Rather than discrete body wall muscles, our model uses spatially continuous muscle forcing, fitting with the continuous representation of the body and approximating the effect of biological muscles which overlap one another on the dorsal and ventral sides. Muscles respond to neural activation over a biologically grounded muscle time scale τ_m (table 4.1), and so can be expressed as

$$\tau_m \frac{d\beta(u,t)}{dt} = -\beta(u,t) + \beta_0 A(u,t)\ , \tag{4.17}$$

where A represents a neural activation or muscle input, β is the torque experienced by the midline due to the difference in contractile force produced by dorsal and ventral muscle pairs,

	Description	Label	Value
Geometric constants			
	Body length	L	1 mm
	Cuticle width	r_{cuticle}	0.5 μm
	Maximum radius along body	$\bar{R}$	40 μm
Muscle constants			
	Muscle timescale	τ_m	0.1 s
	Curvature amplitude	β_0	10 mm^{-1}
Nondimensionalization			
	Young's modulus	E	100 kPa
	Internal viscosity	η	10 kPas
	Tangential drag coefficient	$K_{\tau,\text{agar}}$	3.2 $\text{kg m}^{-1}\,\text{s}^{-1}$
		$K_{\tau,\text{water}}$	$3.3\cdot 10^{-3}$ $\text{kg m}^{-1}\,\text{s}^{-1}$
	Normal drag coefficient	$K_{\nu,\text{agar}}$	128 $\text{kg m}^{-1}\,\text{s}^{-1}$
		$K_{\nu,\text{water}}$	$5.2\cdot 10^{-3}$ $\text{kg m}^{-1}\,\text{s}^{-1}$
	Characteristic time scale	T_0	3.3 s
	Characteristic length scale	x_c	L
	Pressure	p_c	$K_{\nu,\text{agar}} x_c^2/T_0$
Feed-forward control			
	Imposed wavelength	$\lambda_{\text{f,agar}}$	0.6 mm
		$\lambda_{\text{f,water}}$	1.6 mm
	Imposed frequency	$f_{\text{f,agar}}$	0.5 s
		$f_{\text{f,water}}$	1.6 s
Proprioceptively-driven control			
	Proprioceptive thresholds	$\theta^{\text{D}}_{\text{on}}$, $\theta^{\text{V}}_{\text{off}}$	-3 mm^{-1}
		$\theta^{\text{D}}_{\text{off}}$, $\theta^{\text{V}}_{\text{on}}$	3 mm^{-1}
	Proprioceptive range	δ_{a}	0.0 mm
		δ_{p}	0.5 mm

Table 4.1: Default parameters used in model, given in dimensional form.

and β_0 is the amplitude of the preferred curvature which relates to muscle strength and dictates the amplitude of undulations (or maximal curvature, equation (4.10)).

Nondimensionalization

The model of Cohen and Ranner was nondimensionalized in order to further simplify by reducing the number of free biomechanical parameters, and to select an appropriate scaling by which the numerical method will operate. A detailed description of this process for the mechanical component can be found in [37]. Quantities to be rescaled include geometrical quantities (the length and radius of worm), a time scale, estimated material properties of the body (the Young's modulus and internal viscosity) and external drag coefficients. The dimensions of the wild type worm are consistent between individuals, with a length $L = 1\,\mathrm{mm}$, maximum diameter $\bar{R} = 40\,\mu\mathrm{m}$ and cuticle thickness $r_{\mathrm{cuticle}} = 0.5\,\mu\mathrm{m}$. Estimates of the Young's modulus vary from $E \approx 3.7\,\mathrm{kPa}$ [170] to $E = 380\,\mathrm{MPa}$ [142]. In order to nondimensionalize the elastic modulus, Cohen and Ranner select a mid-range estimate of $E = 10\,\mathrm{MPa}$ [37] which is closer to that given by Fang-Yen et al. [55]. Using a time scale and drag coefficients matching the undulation period of *C. elegans* in agar-like conditions and corresponding drag coefficients (Table 4.1), yields a reduced non-dimensional model in which the mechanics can be expressed in terms of three dimensionless parameters

$$K = \frac{K_\nu}{K_\tau}\,, \qquad e = \frac{I_\mathrm{c}\,T_0}{L^4}\,\frac{E}{K_\tau}\,, \qquad \mu = \frac{I_\mathrm{c}}{L^4}\,\frac{\eta}{K_\tau} \tag{4.18}$$

where $I_\mathrm{c} = 2\pi\bar{R}^3 r_{\mathrm{cuticle}}$. This yields the dimensionless model equation for the balance of forces

$$K\tilde{v}_\nu\tilde{\boldsymbol{\nu}} + \tilde{v}_\tau\tilde{\boldsymbol{\tau}} - \frac{(\tilde{p}\tilde{\boldsymbol{\tau}})_u}{|\tilde{\boldsymbol{x}}_u|} + \frac{1}{|\tilde{\boldsymbol{x}}_u|}\left(\frac{eI_\mathrm{c}}{|\tilde{\boldsymbol{x}}_u|}(\tilde{\kappa}-\tilde{\beta})_u\tilde{\boldsymbol{\nu}} + \frac{\mu}{|\tilde{\boldsymbol{x}}_u|}\tilde{\kappa}_{ut}\tilde{\boldsymbol{\nu}}\right)_u = \mathbf{0}. \tag{4.19}$$

Where the tilde denotes the new set of nondimensionalized variables, which are rescaled as follows [37] (see Table 4.1):

$$\tilde{\boldsymbol{x}} = \boldsymbol{x}/x_\mathrm{c} \quad \tilde{p} = p/p_\mathrm{c} \quad \tilde{\kappa} = \kappa/x_c \quad \tilde{\beta} = \beta/x_c.$$

In relation to the neuromuscular component, one would ideally think of the proprioceptive current I_κ and proprioceptive thresholds θ in terms of picoamperes, and neural states $V_{\mathrm{VB}}, V_{\mathrm{DB}}$ in terms of millivolts. However, since the aim of the model is to incrementally gain understanding, building from the simplest case, the neural component interprets proprioceptive current and thresholds directly in units of body curvature. Therefore, these variables are simply scaled by L in the same way as curvature κ. The key advantage here is the seamless integration between neuromuscular control and body mechanics, providing numerical stability and computational efficiency. The binary neural states (equation (4.13)), and by extension the activation function, are already nondimensional so do not require any scaling. For the mechanical model, Cohen and Ranner provide proof of numerical stability, with convergence for reasonable mesh size and time stepping robust over a wide range of parameters [37, 154]. The full non-dimensional model is solved using a finite element method with 128 mesh points.

Chapter 5

Results I - Mechanical and neural modulation of gait

5.1 Mechanics of gait modulation

It has long been observed that *C. elegans* smoothly adapts its gait in response to changes in the resistivity of the surrounding environment [14, 55, 110]. Gait modulation as a result of changing external load was first demonstrated in *C. elegans* by Berri et al. [14] who recorded worms undulating in non-Newtonian media (solutions with different concentrations of gelatin), finding a correlation between undulation frequency and wavelength during forward locomotion. Using resistive force theory, they estimated the ratio of drag coefficients $K = k_\nu/k_\tau$ (equation (4.18)) to be in the range $1.5 \leq K \leq 40$, approximating water on the lower end and stiff gels ($\geq$2% gelatine solution) at the higher end. Their results showed that gait modulation in *C. elegans* is smooth rather than discrete, suggesting that a single neural circuit governs this transition rather than multiple discrete circuits. Shortly after, Fang-Yen [55] performed similar experiments using Newtonian fluid ($K \approx 1.5$), and also reported a correlation between wavelength and frequency, and a smooth transition, when varying fluid viscosity over six orders of magnitude. This suggests that both drag ratio and fluid viscosity can be used to approximate mechanical load acting on the worms body since both correlate with a change in gait.

In both sets of experiments, higher mechanical load results in low frequency undulations and short undulation wavelengths compared to body length L ($\leq$ 0.5 Hz and $\approx$ 0.6 L on thick gel or agar) and lower loads result in more rapid undulations with a longer wavelength ($\approx$ 1.5 Hz and $\approx$ 1.5 L in water or buffer solution) [14, 55]. The definitions and methods used to calculate metrics such as frequency and wavelength from my simulations can be found in the Appendix section A.1. Briefly, frequency is measured as the reciprocal of the mean time between crossing of zero curvature 10% down the midline, and wavelength is the gradient of curvature contours,

multiplied by the period of undulations and averaged over an undulation period. In particular, it should be noted that this 'arc length' definition of wavelength differs from the conventional definition in physics (the distance between two crests of a wave) and is intended to be more physiologically intuitive. Here, wavelength can be thought of as the distance along the midline required to cover a full span of body curvatures, as a fraction of the total body length.

Before the current work, only the model due to Boyle et al. [18] has succeeded in quantitatively reproducing modulation of both wavelength and frequency by external load. The model achieved this through changes in either fluid viscosity ($K \approx 1.5$ fixed) or effective fluid viscoelasticity ($K \in [1.5, 40]$), without requiring other parameters to be altered e.g. within the neural component or body mechanics. The model suggests that proprioceptive feedback, along with a sufficient nonlinearity in the neuromuscular circuitry, is sufficient to produce gait modulation. This set a new standard for models intending to explore the neuromechanics of locomotion in *C. elegans*, and modellers have since added to this framework to ask questions about aspects of locomotion such as steering [88] and omega turns [58].

Although this model is enlightening, it is not without particular drawbacks which limit explanatory power, as discussed in previous sections 3.4 and 4.1. For example, the model implements the core circuit with nonlinear dynamics to reproduce gait modulation, but includes multiple additional functions within the neuromusculature such as a linearly decreasing muscle efficacy along the body, and an asymmetric state-dependent membrane conductance in DB but not in VB. One such function compensates for the head to tail asymmetry in proprioceptive feedback by rescaling in a manner proportional to the ratio of neural 'units' and muscles. This function is necessary for the model to produce coordinated output, but poses an additional biological assumption that stretch sensitivity of a B-type neuron depends on the number of muscles posterior to the soma. Moreover, while some parameters such as drag coefficients are directly comparable to experimental measurements, material parameters such as the Young's modulus are defined over a one dimensional spring [18], making direct comparison to the biological worm challenging. Finally, a feature of the model pointed out by Boyle is a region in drag coefficient space in which locomotion was uncoordinated and therefore did not yield definitive wavelength measurements [18]. The cause of this model behaviour remains unknown but it is possible that its discontinuous geometry leads to instability in particular postures, or that the nature of the proprioceptive feedback makes the motor circuit vulnerable to deviations from smooth wave propagation. Further steps need to be taken in order to fully understand the relationship between mechanics and neural dynamics in different environments.

An advantage of the current model is the simplification of the neuromuscular component down to the minimal requirements for locomotion, and embedding this within a mechanical framework more readily interpretable in the context of the biological worm. Through this I can meaningfully interpret the relative contributions of mechanical properties such as the material

parameters and cuticle thickness, while probing the effects of neural input, either from upstream control or B-type sensitivity and morphology, on posture control during locomotion. The simple interface between the neural and mechanical components, represented by preferred curvature $\beta(u,t)$, allow me to test for behavioural distinctions between proprioceptive and endogenous control.

In this section I use the updated model formulation to investigate neuromechanical relationships on gait kinematics. I show that locomotive gait partitions into separate regimes determined by dimensionless parameter e (equation (4.18)), suggesting a fundamental relationship between body mechanics and environment. I consider, incrementally, the effects of body elasticity and internal viscosity on locomotion under the assumption of purely feedback driven locomotion, finding that viscosity is not essential for sustained undulations but constrains undulation frequency, particularly in environments imposing low mechanical load. I also discuss the implications of these results on aging and cuticle-affected mutant worms. Finally, I investigate the ability of proprioceptive neurons to modulate waveform in order to show how minimal circuitry can produce significant changes in gait within fixed environments.

5.1.1 Purely elastic model reproduces gait modulation

Initially I will neglect internal viscosity of the body by setting $\eta = 0$. This is in line with my incremental approach to modelling, intended to build an understanding of each model component step by step. Furthermore, previous beam models of *C. elegans* locomotion have incorporated body elasticity and viscosity from the outset [169, 55, 92]. In particular, no purely elastic, feedback driven model has yet been characterised; the Cohen and Ranner model assumes viscosity to be negligible, but the neural control is imposed [37]. Given that among experimental estimates it is common for the viscosity estimate to be much lower in magnitude than the elasticity estimate, it is plausible that viscosity plays no significant role in locomotion, or may play a role depending on the worms surrounding environment. I note that Boyle et al. [18] required damping components in the cuticle and muscles to reproduce experimentally observed waveforms, particularly in low viscosity media. I will test for gait modulation by simulating the model worm and sweeping over the same drag coefficient values as Boyle et al., accounting for the fact that the current model applies drag per unit length [37]).

Using the simplified proprioceptive control embedded within the continuum elastic shell, the model qualitatively reproduces the observed relationship between undulation frequency and wavelength, confirming that these kinematic parameters are tightly coupled under proprioceptive drive (figure 5.1). Quantitatively, the model displays realistic undulations in agar-like conditions but unrealistically high frequencies as drag coefficients approach values corresponding to water. This issue will be revisited after including internal viscosity (section 5.1.3). It is worth noting that both the Boyle et al. model, and the current model have now demonstrated proprioceptively facilitated gait modulation, suggesting that these results emerge from

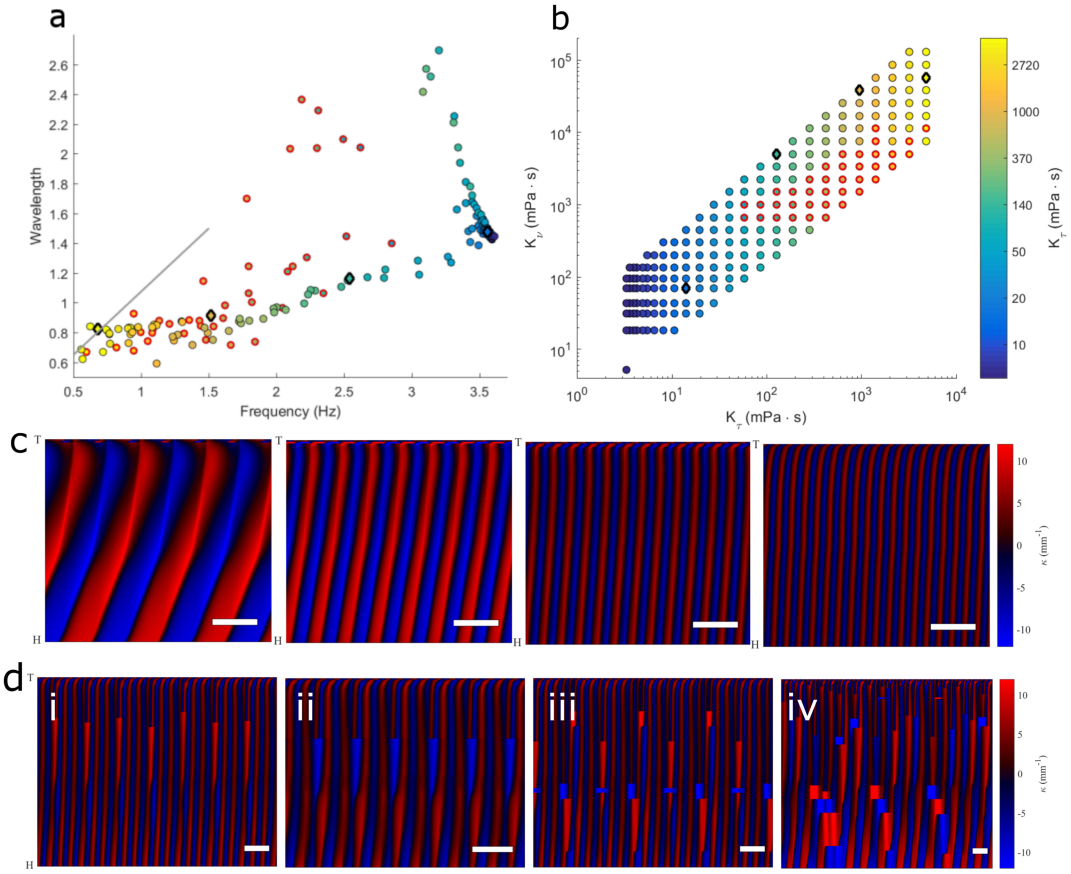

Figure 5.1: (a) Frequency and wavelength of undulation both increase when the drag imposed on the body by the surrounding fluid is reduced, represented here by decreasing tangential and normal drag coefficients (K_τ and K_ν, respectively). Grey line represents gait modulation data from Berri et. al [14]. Red circles highlight simulations showing uncoordinated locomotion. (b) Drag coefficients used. Black diamonds highlight simulations shown in the kymograms below. (c) Kymograms showing midline curvature over time for progressively decreasing drag coefficient values from left to right. The y-axis represents the body coordinate from head to tail, and the x-axis is time - the white bar represents one second. One can clearly see more tightly packed and vertically oriented stripes indicating a higher frequency and higher wavelength as the drag values are lowered. See also the corresponding simulations in the supplemental movies 1(a-d) (Appendix section A.4) (d) Similar kymograms displaying characteristic examples of uncoordinated locomotion with varying severity. (i) Mostly healthy, with occasional but repetitive phase skips in the midbody. (ii) One side dominates bending (this can be dorsal or ventral), with double frequency undulations in the tail. (iii) More complex repeating patterns with phase-skips both in the midbody and the tail. (iv) Non-repeating, chaotic deviations from healthy wave propagation. See also supplemental movies 2(a-d) (Appendix section A.4).

the underlying model assumptions rather than from the specifics of the implementation such as discontinuous articulated body [18] versus continuous elastic shell [37, 47]. Together, these models suggest that proprioceptive feedback to the core motor circuit [138, 24] along with bistability are sufficient components for smooth gait adaptation under changes in the physical environment.

One of the motivations for deriving a continuum mechanical model was to eliminate any uncoordinated dynamics that may result from the mechanical discreteness of an articulated model. The limits of the continuous viscoelastic model were analyzed by Cohen and Ranner [37] under feedforward neural control, with a proof of convergence for the purely elastic body and numerical validation for the complete viscoelastic implementation. It was therefore informative to observe similar uncoordinated locomotion under proprioceptive control to that found in Boyle et al. [18], and for similar intermediate drag coefficients. Furthermore, the nature of this uncoordination appears to be similar, in that undulations mostly appear healthy except for a phase skip in which an area of the midbody pauses once every few undulations for one period before resuming undulations (figure 5.1 and discussion section 5.3). This means that despite the common success of the assumptions underlying both models, they also seem to carry this pathology. Either this is a reflection of locomotion in the real worm and the trajectory through drag space in experiment happened to avoid this problem, or neuromechanical models to date exclude an important mechanism which provides robustness in such environments. To my knowledge this issue has not previously been confronted, and although there are many strains of mutant worms that display uncoordinated behaviour, wild type worms display smooth continuous wave propagation in all experimentally tested environments. It therefore remains to uncover the cause of this uncoordinated behaviour in the model worm, and suggest potential mechanisms to provide robustness to environmental constraints to inform our understanding of motor control in the real worm. In order to keep track of the parameter sets for which uncoordination occurs, simulations deemed to display uncoordinated locomotion are highlighted in red throughout this section. However, the process of identifying these simulations is to observe each kymogram individually and is therefore subject to human error. It is also apparent from figure 5.1 that as drag coefficient values approach the lower end of those tested, undulation wavelength becomes non-monotonic: as the frequency continues to increase beyond $\approx 3\,\mathrm{Hz}$, the wavelength values from some simulations take on unusually high values before decreasing. Rather like the uncoordinated simulations, similar behaviour is exhibited by the Boyle et al. model but does not appear in the experimental data and the cause for this is currently unclear.

5.1.2 The importance of being elastic

Both Berri et al. [14] and Fang-Yen et al. [55] provide experimental data on gait modulation and, although only Berri et al. investigated both Newtonian and non-Newtonian fluids, the

upper and lower bounds of fluid viscosity in both experiments are comparable; from 1 mPa.s (for water) up to $\approx 10^4$ mPa.s. In both data sets, frequency and wavelength appear to saturate when viscosity approaches these upper and lower bounds. It is interesting that gait modulation is only permitted within these bounds because it suggests a balance between competing forces or timescales such that when one factor becomes dominant, gait modulation is prevented. Since I begin by assuming that the shell is purely elastic, I investigate the relationship between elasticity and gait in a range of environments to shed light on this question. From the nondimensional parameters e and K (equation (4.18)), one expects an inverse relationship between the effect of the body elasticity E and the external viscosity. However, it is possible that the effect of the feedback loop, with the spatially extended proprioceptive field would complicate this relationship.

I repeated the simulations shown in figure 5.1 with four different elasticity values selected across two orders of magnitude and the results are shown in figure 5.2 in terms of dimensional parameters; Young's modulus E (Pa) and tangential drag K_τ ($\mathrm{kgm^{-1}s^{-1}}$). For identical drag values, an increase in elasticity results in an increase in both frequency and wavelength of undulation. Intuitively, a stiffer body is more readily able to push against the surrounding fluid such that peak bending amplitude is reached within a shorter timeframe. Therefore the proprioceptive feedback, detected by the B-type neurons, reaches the neural switching threshold in a shorter time, resulting in the observed frequency increase. The cause of the wavelength response is not as intuitive. Higher elasticity increases the mechanical coupling strength between local body regions which increases the bending wave speed down the body. An increase in wave speed is equivalent to an increase in wavelength (this is demonstrated nicely by kymograms, where wave speed is a function of the angle between a curvature contour and the time axis).

This result is generally consistent with the most relevant experimental findings thus far. Multiple studies [68, 125] report a decrease in undulation frequency in worms as they age, which in turn is tightly correlated with a decrease in cuticle elasticity [54]. To my knowledge, there are no direct experimental measurements of frequency or wavelength in mutant worms whose elasticity differs significantly from wild type worms. However, since dumpy mutants reportedly have approximately half the body stiffness of wild type worms [142, 145], one would expect a lower undulation frequency if feedback plays a significant role in locomotion.

Underlying factors of mechanical gait modulation

Consistent with experimental data, the model shows two separate regimes; a modulation regime in which the kinematics depend upon the drag coefficients, and a saturation regime in which drag no longer influences gait (figure 5.3). Previous studies have suggested that gait can be characterised as a function of numerous variables including drag ratio K [14], individual drag coefficients [18], and fluid viscosity μ [55]. It is evident that the boundary between these

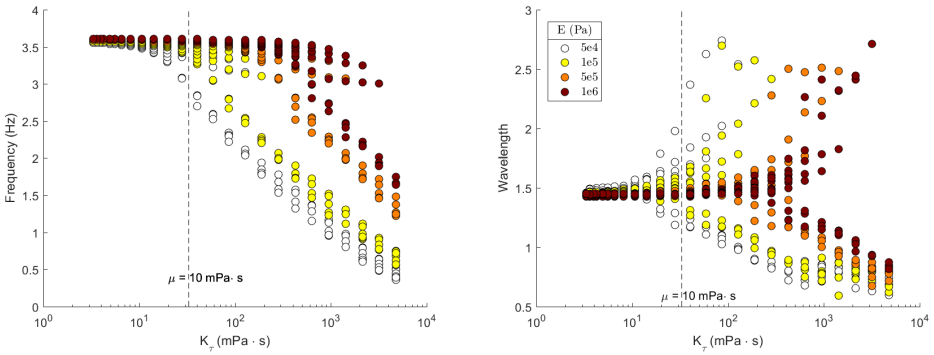

Figure 5.2: Frequency and wavelength modulation with increasing values of the Young's modulus, plotted against tangential drag. Dashed vertical line shows drag value corresponding to the minimum external fluid viscosity value required for gait modulation from Fang-Yen et al. [55].

regimes also depends on body elasticity, but not immediately clear what relationship determines the onset of transition. Figure 5.3 shows the model data plotted against the nondimensional parameter e, which symbolises the ratio of tangential drag with elasticity, scaled by the body geometry and the characteristic undulation timescale (equation (4.18)). Here, the kinematics collapse into a single curve with the modulation and saturation regimes separated by $e \approx 1$, suggesting that this is the control parameter of interest. This reveals a more general picture beyond a reaction to changes in external drag. From this perspective, lower elasticity simply shifts the kinematics to the left along the same function. The elastic model suggests that the viscosity of the surrounding fluid and body elasticity form the key fundamental relationship describing mechanical modulation of gait. For $0 < e < 1$ the fluid viscosity dominates, but as this value increases toward the saturation regime $e > 1$, the new dominant time scale comes from the internal dynamics, which emerges from the wave propagation, as determined by proprioceptive threshold and range, combined with the time scale of muscle contraction.

By presenting the model data as in figure 5.3, the emergence of non-monotonic wavelength values is seen more clearly and is consistent across the different values of the Young's modulus. Here, as e decreases, a bifurcation occurs in which most wavelength values decrease as would be expected, but some appear to increase asymptotically. There does not seem to be a clear relationship between the mechanical parameters to account for this, but wavelength values follow the asymptote in environments with intermediate tangential drag values and low normal drag values (see also figure 5.7). Since lower drag values induce higher wavelengths in general, it is tempting to postulate that a disproportionately high tangential drag causes the body posture to straighten out along the long body axis. However, this does not explain why the behaviour persists only for mid-range K_τ values and not the entire lower end of tested values.

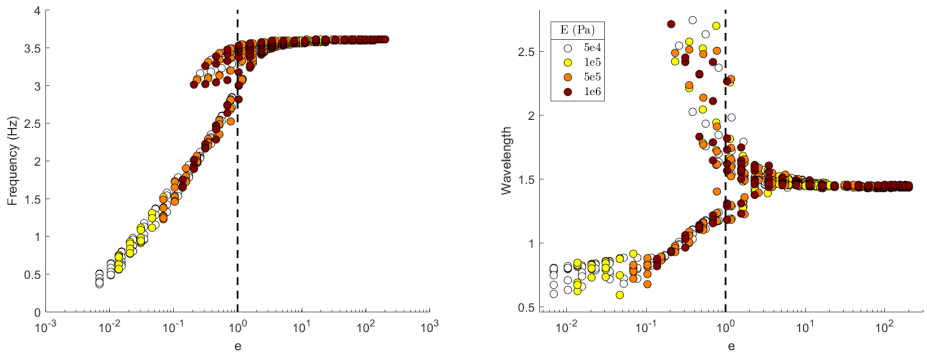

Figure 5.3: Frequency and wavelength modulation with increasing values of the Young's modulus, plotted against nondimensional parameter e. Simulations now collapse onto the same curve with saturation and modulation regimes separated by e= 1 (dashed line).

Model prediction of Young's modulus

Reinterpreting e in terms of physical variables can provide new predictions of the elasticity of the worm under the assumption of feedback dominated control. The requirement $e \leq 1$, implies an upper bound of $E \leq 5$ MPa. However, considering the lower viscosity values at which the frequency and wavelength appear to saturate in the Fang-Yen et al. data ($\mu \approx 10$ mPa.s - figure 5.2), and matching them with the model data gives a lower estimate of $E \approx 100$ kPa. Taking the drag coefficient values used by Boyle et al. to describe water and agar environments, Young's moduli within the range $E \in (50, 100)$ kPa allow for the full range of modulation. 50 kPa serves as an appropriate lower bound, since anything below this renders the model worm unable to undulate in higher viscosity environments such as agar, in which free movement is abundantly recorded. This prediction coincides with the chosen default value of $E = 100$ kPa for typical forward locomotion during free behaviour, which is also consistent with previous estimates using the same model mechanics only subject to rhythmic sinusoidal forcing rather than feedback [37]. Naively, this reasoning rules out the peak speed (achieved around $e \approx 10$, figure 1.3), but it is known that *C. elegans* can modulate its muscle tonus with a dramatic effect on stiffness. Using an estimate of $E = 380$ MPa from Park et al. [142] would easily allow the nematode to reach this maximum speed. Of course, any elasticity prediction of the real worm from this model relies on the accuracy of measured drag coefficients given in the work of Niebur and Erdös [137] and Boyle et al. [18]. For example, if these estimates were too low by a particular factor, this would imply that the above predictions should be increased by the same factor. Furthermore, the process of converting the nondimensional parameters back to their restored dimensions requires making a choice because the transformations between dimensional and nondimensional parameter sets is not a bijection. From the nondimensional parameters, e depends both on the worm's length and diameter through the scaling of the second moment of

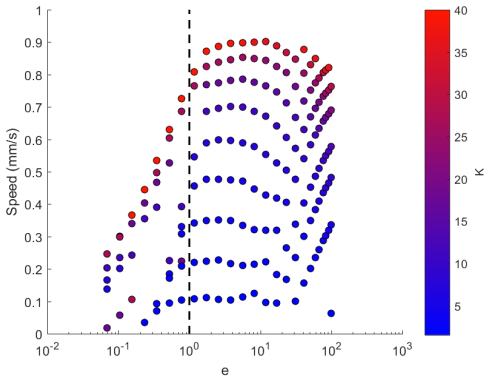

Figure 5.4: Locomotion speeds recorded over gait modulation sweep, coloured by ratio of drag coefficients K. Young's modulus set to default value ($E = 100\,\text{kPa}$).

inertia $I_c = 2\pi R^3 r_{\text{cuticle}}$ (section 4.1) [37]. The model could also make predictions about the elasticity of worms with different dimensions. For example, assuming the worm is 10% shorter with a radius 10% larger would yield a new upper bound of $E \leq 2.4\,\text{MPa}$, approximately half of the original estimate. However, this is only taking into account the differences in body dimensions without accounting for other likely important factors such as changes in internal pressure [142] or the ratio of body width to cuticle thickness.

5.1.3 Internal viscosity

So far I have focused on locomotion kinematics in worms absent of internal viscosity. However, biological tissue, including that of *C. elegans* possesses both solid and fluid properties [98]. An existing viscoelastic beam model by Sznitman et al. [170] estimated the effective internal viscosity of $\eta = -860.2 \pm 99.4$ Pa·s, along with a Young's modulus of $E = 3.77 \pm 0.62$ kPa by fitting the model worms posture to videos of swimming wild type worms. However, this model was driven in a feedforward sense, using an imposed muscle activation profile within a fixed environment. Fang-Yen et al. [55] use a similar model to replicate their own experiments in which worms were manipulated into a sharp body bend using micro-pipettes (reminiscent of Sauvage [159]) to match the rate of relaxation times in different fluid viscosities. Based on these experiments, the model predicts an upper bound of $\eta \leq 68$ kPa·s with corresponding Young's modulus 13 MPa. As with elasticity, the scale of the worm and the multiple layers of the outer shell (cuticle, hypodermis and muscle) make such measurements challenging in an experimental setting, and different experimental techniques may in reality measure the viscosity of one, or a combination of these layers. Note that the current model describes this outer shell as a uniform material of fixed thickness (as shown by equation 4.5) and therefore assumes that the material properties, elasticity and viscosity, occupy the outer shell uniformly.

In the elastic only case, the model is capable of qualitatively reproducing gait modulation, but undulation frequency in low viscosity environments is roughly double the experimentally observed values. Since viscosity describes a resistance of a fluid to deformation (to bending in this case) and has a velocity dependence, its inclusion may resolve this issue in water-like environments maintaining kinematics in higher viscosity environments at quantitatively correct values.

Internal elasticity-viscosity ratio determines kinematics in low viscosity media

Since I expect internal viscosity to have a greater effect in a less resistive medium, I choose to begin by placing the model worm in a water-like environment and sweep over elasticity and internal viscosity values, measuring their effect on locomotion in the usual way. Results show straight diagonal contours in (E, η) space for both frequency and wavelength, separated by the lines $\ln(\eta) = \ln(E) + \ln(\text{const})$. Reminiscent of the previous result regarding nondimensional parameter e, this indicates that, at least for dynamics dominated by internal timescales, it is not the absolute value of internal viscosity that predicts kinematics, but the ratio between elasticity and viscosity $r_{\text{mech}} = E/\eta$. This seems nontrivial since the effects of elasticity and viscosity are dependent on displacement and rate of displacement from equilibrium, respectively. However, ratio r_{mech} has the physical dimensions of a rate, specifically the highest permissible bending rate in absence of external constraint, and is the determining factor of the saturation frequency such that $f \to f_{\text{sat}}$ as $r_{\text{mech}} \to \infty$. Interestingly, wavelength displays a non-monotonic response to internal viscosity, which peaks at around $r_{\text{mech}} \approx 10$. One implication of this for material

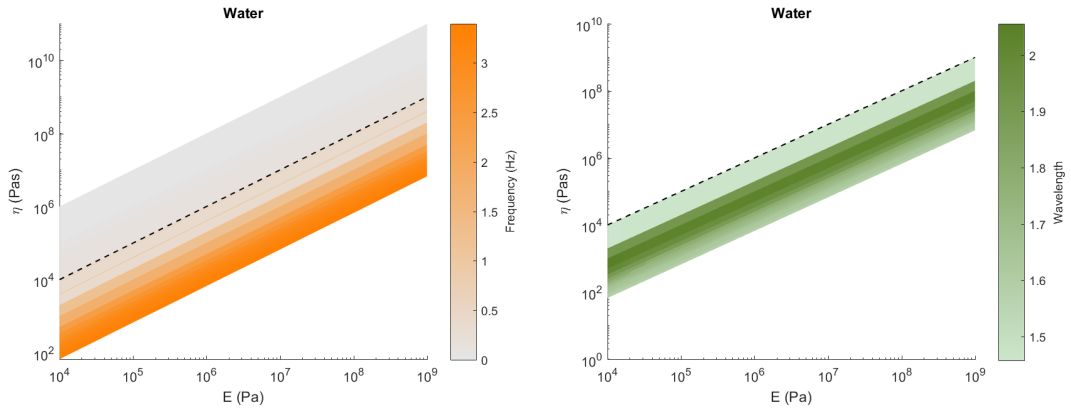

Figure 5.5: Parameter sweep of Young's modulus and internal viscosity of worms in a water-like environment ($K = 1.57$). Colors show frequency (left) and wavelength (right) which follow contours parallel to $\eta = E$ (black dashed line). No wavelengths are calculated above the dashed line since there were no consistent undulations for $\eta > E$.

parameter estimates made by fitting viscoelastic rod kinematics to swimming worm waveforms, is that a fixed elasticity values may correspond to multiple possible viscosity values (under the assumption of feedback driven control).

Viscosity returns frequency to quantitatively observed values

From the data in figure 5.5, I set the default viscosity value to $\eta = 10$ kPa·s (such that $r_{\text{mech}} = 10\ \text{sec}^{-1}$) to match the experimental data. Next I returned to the gait modulation tests which are displayed in figure 5.6, showing gait modulation for different viscosity values including the new default value. These tests confirm that internal viscosity limits undulation frequency in water-like conditions and has a less significant impact in agar (though not negligible) compared to water. These default values $E = 100$ kPa and $\eta = 10$ kPa·s show a good fit to experimental data since the overall effect is to shift undulation frequency downward proportionally to drag whilst largely maintaining wavelength values. However, for intermediate drag coefficients, close to the region of uncoordinated simulations, the inclusion of internal viscosity manifests in unusually large wavelengths (see discussion).

5.1.4 Uncoordinated behaviour

As previously mentioned, a small proportional of simulations result in uncoordination locomotion. These are common to both the current model and Boyle's neuromechanical model [18], and occur for almost identical sets of drag coefficient values. Mostly, they manifest as short periods of healthy wave propagation punctuated by dorsal or ventral kinks in the midbody, sometimes accompanied by higher frequency undulations in the tail (figure 5.1). Some cases

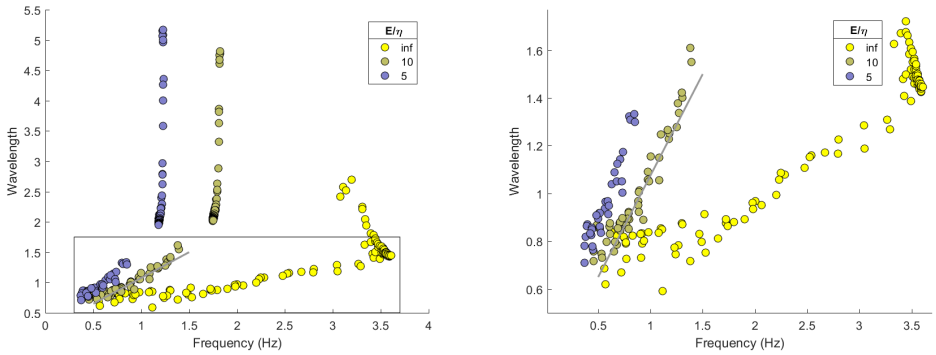

Figure 5.6: Gait modulation with varying values of internal viscosity with fixed Young's modulus. Left panel shows full sweep including unusally large wavelength measurements for intermediate drag coefficients. Right panel shows the same data, zoomed to show the line fit to Berri et al. data. [14]

are more severe, displaying chaotic disruptions in wave propagation, though generally wave propagation is still recognisable. Due to the feedback nature of the neural control, it is apparent that both mechanical and neural factors have some impact on this behaviour, though it remains to be determined which of these factors plays the more significant role.

For all simulations discussed thus far, simulations showing uncoordinated locomotion are displayed in figure 5.7 in terms of the nondimensional model parameters e and K. These plots show healthy locomotion across gait modulation when normal drag is comparatively high (i.e. for large K). It appears that an increasing proportion of simulations becoming uncoordinated as the normal drag component becomes comparable in magnitude to the tangential component and as environmental drag begins to dominate the body mechanics ($e < 1$). Under feedback driven control, this particular combination of effects results in phase skips and kinks in mid-body regions or unusually large undulation wavelengths, where the latter effect is further exaggerated by the inclusion of internal viscosity (figure 5.6 and figure 5.7). The same simulations driven in a feedforward sense (neural activation imposed by a travelling sine wave) results in no such behaviour, indicating that the instability is a direct consequence of the feedback driven undulations of the model. It is therefore necessary to characterise the neural effects on locomotion to gain further insight into the continuous interactions between both model components. Uncovering the source of this behaviour and suggesting mechanisms to improve robustness may have predictive power for experimentalists, since many mutant strains display similar locomotion defects.

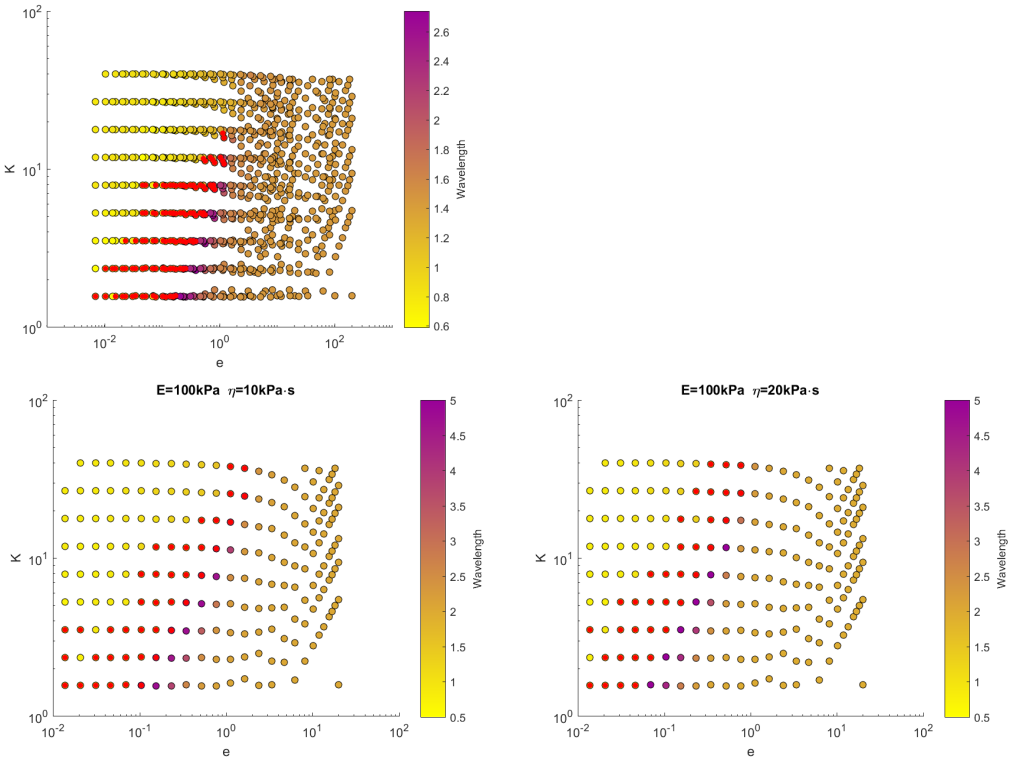

Figure 5.7: Location of uncoordinated simulations in nondimensional parameter space with $\eta = 0\,\text{kPa}\cdot\text{s}$ (purely elastic case), $\eta = 10\,\text{kPa}\cdot\text{s}$ and $\eta = 20\,\text{kPa}\cdot\text{s}$, with colour bar showing values of undulation wavelength. Note: the colorbar on the top row has a different scaling to those on the bottom to emphasize the higher wavelength values.

5.2 Neuronal modulation of gait

External, mechanical forcing aside, *C. elegans* is also capable of adapting its gait in a context-dependent manner within a homogeneous medium, which must therefore be regulated by internal mechanisms. Possible mechanisms include descending neural control (e.g. a modulation of the current input from locomotion command neurons [25]), a modulation of the motor circuit (e.g. the excitability of motor neurons [121]), and a modulation of the proprioceptive field (though no such mechanism has been documented to date). The neural model used here is simplified such that it is described by two fundamental parameters: (i) the proprioceptive threshold and (ii) the range over which body posture is perceived. An increased threshold could correspond to a reduced excitability of B-type motor neurons, reduced sensitivity to stretch, or a reduced tonic input current, for example from AVB command interneurons. Again, for simplicity I explore the case in which the body is assumed to be a purely elastic shell ($\eta = 0$).

5.2.1 Neural threshold

In the neural component of the model, the input to the B-type motor neurons triggers a neural state switch if either an on or off threshold is crossed by the total input, which consists of tonic AVB signal and proprioceptive feedback. Since the former is assumed to have constant magnitude during forward locomotion, it is absorbed into symmetric thresholds $\theta^V_{\text{on}} = \theta^D_{\text{off}}$ and $\theta^V_{\text{off}} = \theta^D_{\text{on}}$ (4.13). Therefore, a decrease in threshold could be interpreted either as an increase in upstream input current or an increase in B-type excitability.

Figure 5.8 shows the effect of threshold modulation on the gait of model worms, when embedded in environments spanning the full range of experimentally tested viscosities. In all environments, the majority of tested threshold values yield robust undulations. Consistently, a decrease in neural threshold results in a higher undulation frequency. Intuitively, a lower average bending amplitude is required over the chosen proprioceptive range before a state switch is initiated. In all tested environments, lower amplitudes take less time to reach which shortens the undulation period, with an exaggerated effect in less resistive environments in which threshold values lower than the default value ($\theta_j = \pm 3$) lead to a rapid frequency increase. A decreased threshold also manifests in decreased undulation wavelengths. The model therefore predicts that modulation of proprioceptive threshold manifests in an inverse relationship between wavelength and frequency. This presents a qualitative contrast to the gait modulation resulting from changes in either external drag or body elasticity. This inverse relationship is maintained across the full range of tested environments, suggesting that the nematode's ability to internally modulate its waveform does not qualitatively depend on its surroundings. This is a novel signature of proprioceptive control. Furthermore, in the majority of tested environments, threshold modulation appears to yield at most a two-fold change in frequency which shows a clear quantitative difference from the multi-fold frequency increase arising from external gait modulation. By contrast, internal modulation of wavelength appears to be dependent on the environment, with up to a

four-fold increase in less viscous media. This also shows a quantitative difference to external modulation alone while pointing to the constraints imposed on posture control by more viscous environments. For higher threshold values than those shown, the increase in time taken for the bending amplitude in the head to reach threshold becomes very long (≥ 40 s), resulting in large initial transients.

5.2.2 Proprioceptive range

The other free parameter in the neural model is the proprioceptive range δ_{p}, which determines the fraction of the body length over which body curvature is averaged in order to drive a change in neural state. By default this range is strictly posterior ($\delta_{\mathrm{a}} = 0$) for simplicity and to reflect the neuroanatomy of the worm. The default range is half of the body length in order to reproduce external gait modulation as observed, although this extended range is regarded as physiologically unrealistic. To date, no biological mechanism is known to dynamically alter proprioceptive range, however, the inverse frequency–wavelength relationship observed during threshold modulation prompts the question of whether other forms of neural modulation would give a similar relationship. To understand the importance of proprioceptive range during locomotion, I varied this parameter from an effectively local range of 5% to a maximum of 90% of the body length posterior, repeating this for the same environments as the above threshold test.

Assuming an approximately sinusoidal gait, intuition would suggest that altering the proprioceptive range would result in a wavelength dependence on the amplitude of proprioceptive feedback. Figure 5.9 demonstrates this by showing the amplitude of fictive proprioceptive feedback along the entire body, and at a single anterior body point, in the idealised case of perfect sinusoidal gait. This case assumes that the presence of feedback does not distort the waveform. If the undulation wavelength is an integer multiple of the proprioceptive range, positive and negative curvature (corresponding to contracted dorsal and ventral muscles, respectively) should cancel, resulting in a net zero drive to the motor neurons. However, a shorter range results in higher feedback amplitudes since the points of the body where proprioceptive range straddles the local peak in body curvature will result in higher average values the shorter the range. One therefore expects the shortest ranges to result in the highest frequencies. However, the rostro-caudal asymmetry in feedback amplitude due to the decreasing range towards the tail could cause the emergence of a more complex relationship.

Consistent with the above intuition, a shorter range tends to result in a higher undulation frequency. As the range is increased, the frequency decreases sharply before levelling out (figure 5.8). A longer proprioceptive range results in a longer undulatory wavelength which appears to broadly follow the relationship $\lambda = 2\delta_{\mathrm{p}}$, with small, environment-dependent variation about this line which maximizes at the default value $\delta_{\mathrm{p}} = 0.5$. Thus, range modulation also gives

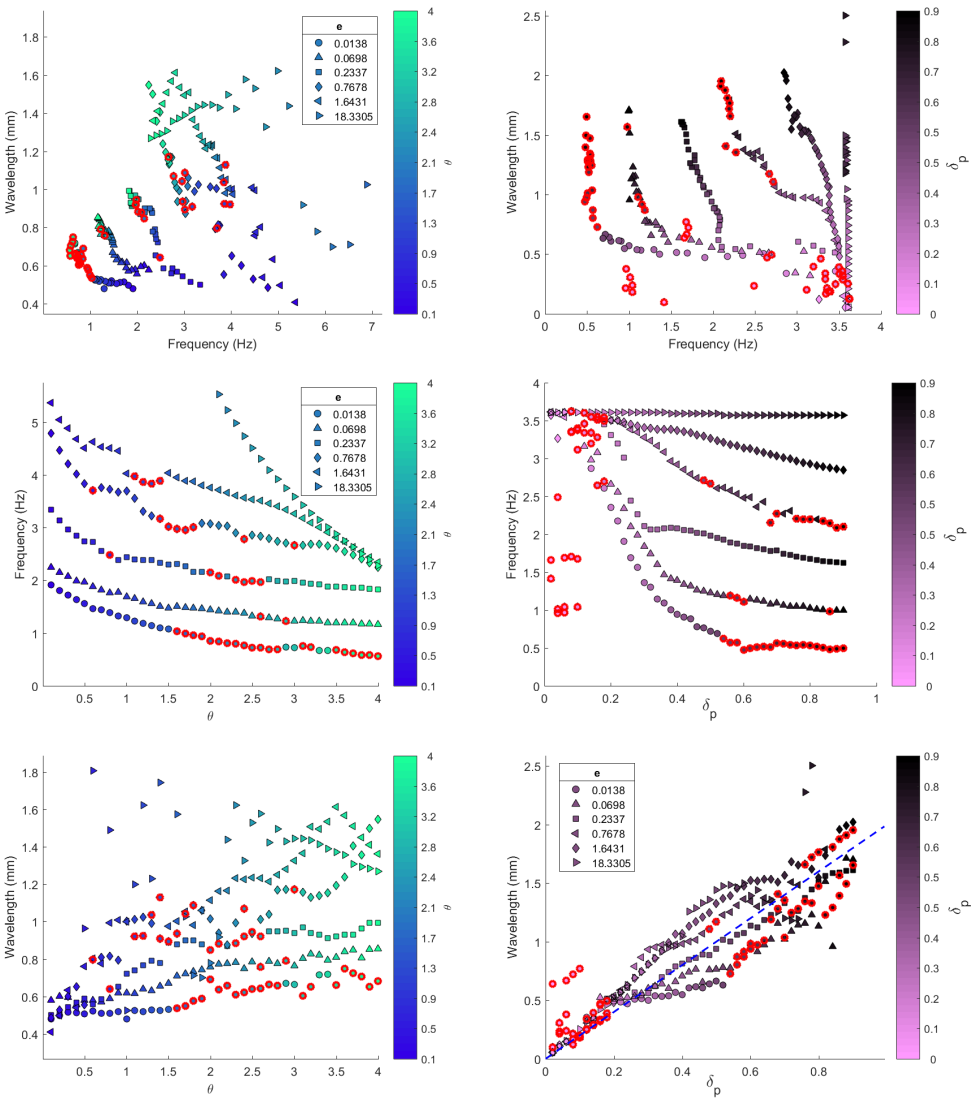

Figure 5.8: Changes in gait under modulation of neural mechanisms, proprioceptive threshold and range. Top panels show inverse frequency–wavelength relationship. Bottom four panels display kinematics separately against their respective neural parameter, in each of six different environments (note that axis ranges therefore vary). Red circles highlight simulated worms displaying uncoordinated locomotion. Blue dashed line (bottom right) highlights the relationship $\lambda = 2\delta_{\mathrm{p}}$.

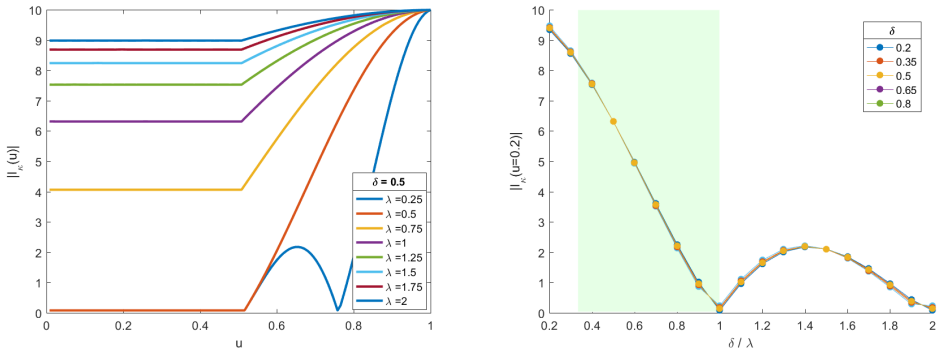

Figure 5.9: Proprioceptive feedback amplitude, assuming body curvature follows a perfect sinusoidal waveform in a feedforward manner with a curvature amplitude of 10 mm^{-1} and frequency 0.5 Hz, while varying wavelength (λ) and range (δ_p). Left: amplitude plotted against body coordinate with proprioceptive range fixed. Right: maximum feedback amplitude at body coordinate $u = 0.2$ plotted against ratio of range to undulation wavelength. Green band indicates the expected ratio values reached across experimentally observed wavelength modulation, assuming default proprioceptive range value $\delta_p = 0.5$.

rise to an inverse relationship between wavelength and frequency, qualitatively mirroring that of threshold modulation. The two methods of internal modulation also have their differences, both quantitatively and qualitatively. The impact of proprioceptive range on locomotion kinematics in a fixed environment is much larger than that of threshold. However, the saturation frequency (set by the relative strengths of the material parameters of the body) appears to also be determined by the threshold value, whereas even the higher frequencies induced by purely local proprioception do not exceed this limit (figure 5.8). Furthermore, the linear relationship between proprioceptive range and undulation wavelength, combined with frequency saturation under range modulation, indicates a decoupling between these kinematics. This indicates a possibility for the motor circuit to vary each kinematic parameter independently, showing a further contrast with external modulations, under which frequency and wavelength appear tightly coupled throughout the gait transition.

5.2.3 Anterior proprioceptive range

The processes of the B-type neurons do extend slightly anterior to their cell body. These anterior processes are shorter than the posterior extensions, ranging from 5% to 10% of the total body length and are thought to be strictly post-synaptic [188, 190, 191]. However, physical clamping experiments by Wen et al. [188] suggested that the stretch detected by the motor neurons may come from a region anterior to the cell body. In response, I opted to extend the proprioceptive range tests with the addition of an anterior proprioceptive region of 10% of the total body length such that $\delta_a = 0.1$. Note from equation (4.16) that the anterior range is assumed to contribute negatively to the total proprioceptive feedback, which could be interpreted as anterior stretch

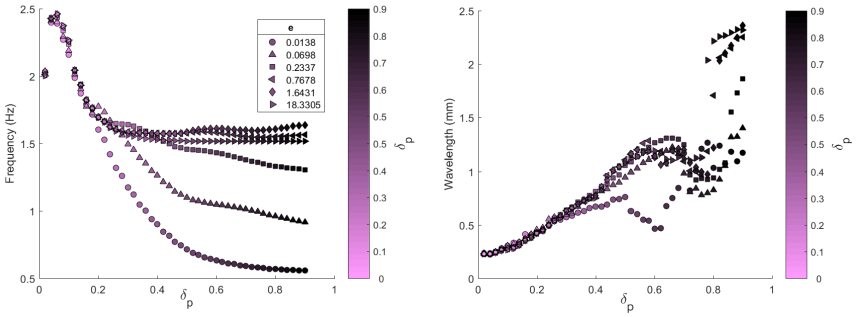

Figure 5.10: Relationship between kinematics and proprioceptive range, with additional anterior range of $\delta_a = 0.1$. Undulations are much more stable for all range values, but less responsive to environmental changes for shorter ranges.

causing a polarizing current to the cell, or an inhibitory response.

Upon re-running the proprioceptive range tests with the additional anterior receptors, the most apparent change is a lack of environment dependent modulation of both frequency and wavelength for shorter posterior range values. This is not an intuitive result since the previous tests suggest that extending the proprioceptive range further should result in higher kinematic variation under changing viscosity. Curiously, this new data set is completely absent of the uncoordinated behaviour observed in all previous tests, indicating that effective anterior range increases robustness of wave propagation to local body kinks and phase skips. In absence of any experimental evidence to support the notion that different motor neuron regions could have contrasting polarity, I would interpret this broadly as an effective mechanism, possibly due to connections between adjacent motor neurons. Nonetheless this represents an initial step towards a solution to the problems arising from both the Boyle et al. model [18] and the current model formulation.

5.3 Discussion

Inspired by a previous neuromechanical model of *C. elegans* locomotion [18], I have integrated a simplified version of *C. elegans* motor circuitry and musculature to a continuum description of the body mechanics to gain novel insights into the neural control of undulatory locomotion under the assumption of feedback-driven control. Firstly, this model is successful in quantitatively reproducing gait modulation which, in the absence of nonlinear muscle activation and rostro-caudally decreasing neural sensitivity [18], emphasises the potential role of an effectively extended proprioceptive field and bistability in VNC motor neurons. Furthermore, the model predicts that only a limited range of effective body elasticity can support the full range of observed gait modulation. Current estimates of the Young's modulus range over five orders of magnitude [142, 170]. By comparing the changes in available gait modulation under different

values of body elasticity with experimental data [14, 55], the model predicts a Young's modulus of $E \approx 100$ kPa, with an upper bound of $E \leq 5$ MPa. This estimate coincides with previous estimates of $E \in (10, 1000)$ kPa by Cohen and Ranner who use the same model mechanics to measured forward thrust generated by feedforward driven undulations [37].

Of course, the validity of these predictions are caveated by the model assumptions. Due to the simplistic modelling approach, some anatomical and material parameters are overloaded such as body diameter and elasticity in the prefactor I_2E, which appear together in the non-dimensional parameter e (equation (4.18)). Likewise, due to absence of data, the model assumes that the cuticle and muscles contribute equally to bulk elasticity by scaling curvature κ and preferred curvature β equally. This model could easily be extended in future to accommodate a more explicit separation of the muscle and cuticle contributions.

Taking advantage of the model nondimensionalisation reveals a more generalised picture of the permissible conditions for gait modulation. Assuming purely elastic body mechanics, body elasticity and external drag reduce to a single universal parameter (taking into account the worms dimensions) which separates a modulation regime ($e < 1$) from a saturation regime ($e > 1$). This clearly highlights the point where increased external forcing begins to dominate the neural and mechanical timescales.

Although the purely elastic model is sufficient to gauge the basic conditions for mechanical modulation, it fails to quantitatively capture the observed frequency-wavelength relationship. The model shows that the additional property of internal cuticle viscosity serves to limit undulation frequencies in low viscosity fluids while having relatively little impact on crawling kinematics, consistent with Boyle et al. [18]. Furthermore, a ratio of $E/\eta = 10$ sec^{-1}, equivalent to $E = 100$ kPa and $\eta = 10$ kPas nicely captures experimental data [14, 55]. From parameter sweeps in low viscosity media, the model suggests that lowering the ratio any further results in a decrease in undulation wavelength, while frequency continues to increase. This is, in fact, consistent with recent modelling efforts by Johnson et al. [92], who use a simplified viscoelastic rod model to demonstrate a non-monotonic undulation wavelength as the muscle timescale (set to $\tau_m = 0.1$ sec in my model) exceeds the mechanical timescale set by ratio E/η. With the viscosity of water well characterised, along with biological limits on muscle timescales, this places strict limits on the feasible relative contributions of the elasticity and internal viscosity of the worm.

The model worm permits control over gait via three fundamental targets: changes in elasticity due to muscle tone, the activation threshold of B-types and the spatial range of the proprioceptive field. Changes in activation threshold correspond to upstream activation from inter neurons AVB (or AVA) or the AVB-B (or AVA-A) gap junctions in forward (or backward) circuitry. Mechanical modulation, due to either increasing fluid viscosity or body elasticity yields

a tight positive relationship between undulation frequency and wavelength. By contrast, neural modulation yields a negative correlation, suggesting a novel signature of locomotion under feedback driven control. This result suggests the possibility to differentiate between the roles of feedback and feedforward mechanisms in the ventral nerve cord. Specifically, evidence of CPGs was shown in recent voltage clamp experiments [61] in the backward circuit. If CPGs do indeed drive the backward, but not forward circuits, modulating the activation of these circuits separately should reveal distinct kinematic relationships regardless of environment.

The advent of uncoordinated locomotion in the articulated Boyle et al. model [18] was partly the motivation for implementing a more numerically stable continuum mechanical model. However, my results have shown that this behaviour persists in the current implementation under both external and internal modulation. It would be insightful if this behaviour occurred at the extremes of such parameter sets, or combinations thereof, since it would indicate that uncoordinated locomotion is a result of, for example, the competition between muscle timescales and mechanical timescales. This does not appear to be the case. In model worms displaying less severe uncoordination, phase skips are isolated to the midbody, where the spatial profile of the proprioceptive feedback begins to increase in amplitude over a single undulation period. As this becomes more severe, some model worms display tail undulations of a higher frequency than head undulations, leading me to believe that the scaling of the feedback along the body may be the cause. However, as shown, adding anterior proprioceptive range immediately recovers healthy locomotion for all tested parameter sets, and a similar intervention aided wave propagation in a robot version of *C. elegans* (personal communication with J. Boyle). While non-smoothness in the body mechanics has been tested, non-smoothness in the neural switching has yet to be ruled out. Boyle et al. [17, 19] did compare the outputs of non-smooth circuit dynamics with physiologically grounded smooth circuit dynamics, finding no significant difference. However, to my knowledge both circuits were not tested during neuromechanical gait modulation.

Chapter 6

Methods II - Inhibition in the ventral nerve cord

6.1 Introduction and motivation

The following is related to a collaboration with the Haspel laboratory leading to the publication "Inhibition underlies fast undulatory locomotion in *C. elegans*" [46]. We investigated the role of inhibition using genetic and optogenetic manipulations, calcium imaging (organised and performed by Lan Deng, Charu Arya, Omer Yuval and Gal Haspel) and computational modelling (myself and Netta Cohen). For the purposes of the thesis, I will lay out the experimental results as a motivation for my contribution, which was the model implementation and testing of multiple hypotheses for the role of inhibition during locomotion. Unless otherwise stated, the model used here matches that described in Methods I (section 4.1).

6.2 The role of inhibition: experimental results

Deng et al. [46], sought to probe the roles of inhibition in *C. elegans* locomotion. It has previously been observed that mutants deficient in GABA transmission exhibited a shrinking phenotype following a head tap [132, 131, 160] in which dorsal and ventral muscles contract simultaneously along the body, resulting in a shortening of the body and no undulations. This is in contrast to wild type worms which exhibit rapid reversals following a head tap. To test this, Deng et al. [46] reproduced the head tap assay in wild type (N2) and three GABA deficient mutant strains: *unc-25* - lacking the GABA synthesis enzyme glutamic acid decarboxylase (GAD), *unc-46* - lacking a vesicular transporter, and *unc-49* - lacking ionotropic GABA receptors. For all four worm strains, a head tap caused temporary shrinking following by a reversal. However, wild type worms shrink less than the mutants, and their undulation frequencies were significantly higher. Moreover, the same was observed for responses to both head taps, leading

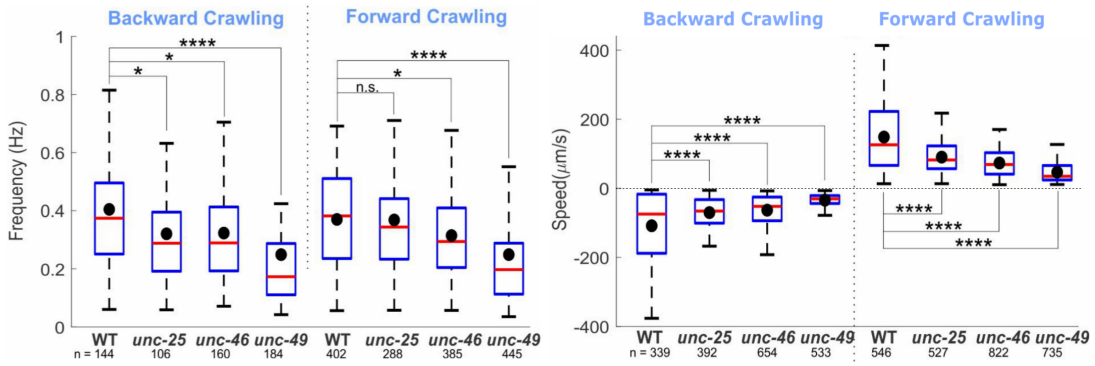

Figure 6.1: Locomotion speed and undulation frequency of wild type and GABA deficient worms, taken from Deng et al. 2020 [46]. Blue boxes range the first and third quartiles of each data set, and red lines show the median. Horizontal line marks speed = 0. Undulation frequency of GABA mutants was significantly lower than wild type, except in crawling *unc-25* mutants. ANOVA with Tukey pairwise comparison to wild type, n.s. $p > 0.05$, * $p < 0.05$, *** $p < 0.001$, **** $p < 0.0001$.

to backward undulations, and tail taps, leading to forward undulations. This suggests that inhibition affects undulation frequency in response to mechanical stimuli in both directions, rather than being essential for only backward undulations as previously suggested [132, 196].

To see if this held for freely moving worms, rather than solely in response to head or tail taps, Deng et al. placed the wild type and mutant worms on to agar plates and in buffer solution [46]. All worms were capable of crawling in both directions, although mutants showed lower undulation frequencies and speeds during forward and backward crawling (figure 6.1). However, a more distinct difference was observed during swimming, in which GABA mutants displayed much slower, less coordinated undulations (figure 6.2), qualitatively consistent with predictions from the Boyle et al. model [18, 17] (section 3.4). Furthermore, optogenetically inhibiting GABAergic neurons during swimming resulted in uncoordinated swimming, which returned to wild type locomotion after inhibition was released. These results suggest that the contribution from GABAergic motor neurons depends on undulation frequency and that they are particularly necessary for coordinated high frequency undulations.

This raises the question of whether the activation of the D-type neurons is fundamentally different depending on undulation frequency. To address this, Deng et al. [46] used calcium imaging of the D-type neurons in worms constrained by sinusoidal microfluidic channels following Lockery et al. (2008) [120]. The channel allowed control of the phase of neural activation over an undulation period, and was filled with either 3% methyl cellulose in nematode growth medium (NGM) buffer to induce low frequency undulations (0.28 ± 0.14 Hz), or 0.5% methyl cellulose to allow higher frequency undulations (0.74 ± 0.26 Hz) [46]. This setup allowed the calcium signal with the inhibitory neurons to be compared to the phase of undulation, with 90° translating to

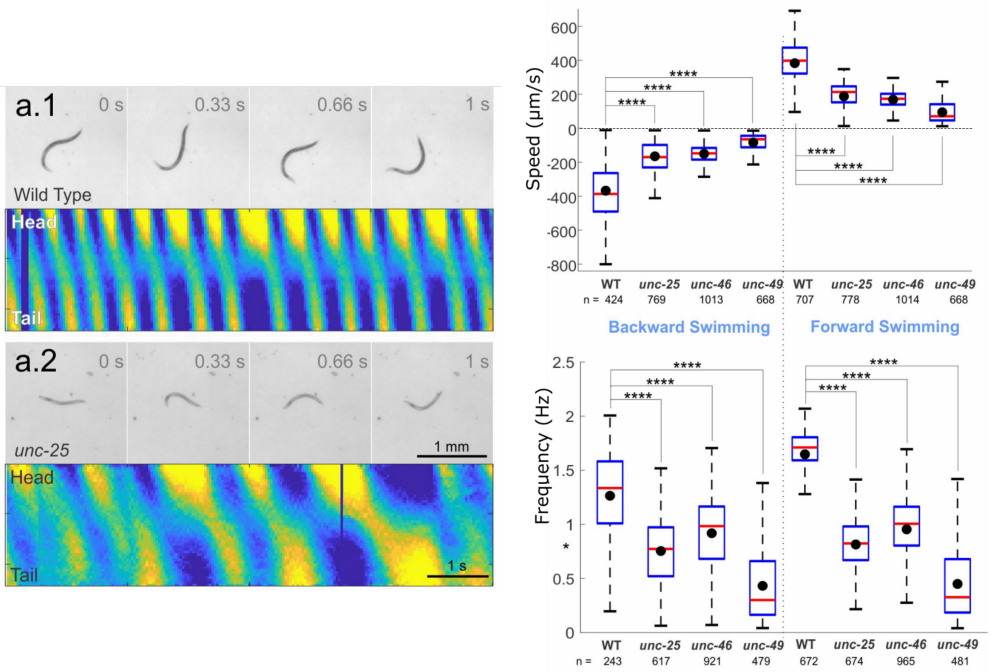

Figure 6.2: Swimming behaviour in wild type and mutant worms, taken from Deng et al. 2020 [46]. Left: Movie frames and kymograms from wild type and *unc-25* worms showing slower, uncoordinated undulations in the mutant. Right: Locomotion speed and undulation frequencies are significantly lower in swimming GABA deficient worms compared to wild type. ANOVA with Tukey pairwise comparison to wild type, **** $p < 0.0001$.

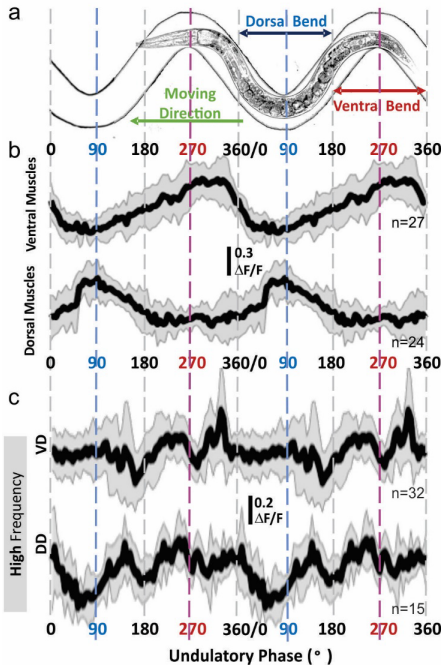

Figure 6.3: Calcium signals during low and high frequency undulations, taken from Deng et al. 2020 [46]. (a) worms were placed in a sinusoidal microfluidic channel to control the phases of dorsal and ventral bends. (b) Calcium traces in ventral and dorsal body wall muscles correspond to ventral and dorsal bending within the channel. (c) In 0.5% methyl cellulose solution (higher frequency undulations) VD shows troughs at roughly 180° and 270°, and DD at roughly 90° and 180°. Only VD showed a sharp increase at 300°, preceding inactivation of the ventral muscle. The sample size (n) indicates the number of analyzed cells. Solid lines and shaded areas in calcium traces are mean and the standard deviation [46].

a peak dorsal bend, and 270° a peak ventral bend (figure 6.3). Results showed a qualitatively different relationship between VD and DD activity and phase during low frequency undulations, compared to higher frequency undulations. During low frequency undulations, VD and DD became active at identical phases, with a wide band of inactivity between 90° and 270°, the transition from a dorsal to ventral bend. This apparent synchrony is surprising since conventional wisdom would suggest that D-type activity should match the activity of the opposite muscle, since they are both driven by the same excitatory neurons. During high frequency undulations, D-type activity is anticorrelated with adjacent muscle activity as one would expect. DD activity decreases at 90° as the dorsal muscle activates, and VD exhibits a sharp increase in activity just after 270°, as the ventral muscle reaches peak activation (figure 6.3). This qualitative difference in D-type activity between low and high frequency undulations supports the notion that inhibition particularly plays a role during high frequency undulations.

6.3 Neuromechanical model - three hypotheses for the role of inhibition

The experiments by Deng et al. [46] show clear phenotypic differences between wild type and numerous GABA deficient mutants. Based on these results, and taking into account the proposed core circuit for *C. elegans* locomotion [138, 24], we condensed the potential roles for inhibition within the VNC into three hypotheses. Firstly, the D-type neurons provide cross-inhibition to the opposite body wall muscles, ensuring opposing muscles are not activated simultaneously. Secondly, the sudden release of muscle inhibition leads to a sharp upstroke in muscle activation and therefore faster contraction compared to no disinhibition. Finally, neural inhibition of VB by VD serves to reset VB to prevent the simultaneous activation of VB and DB, and avoid prolonged shrinking or uncoordination. This hypothesis was put forward by Boyle et al. [18], who use their neuromechanical model to demonstrate that asymmetric neural inhibition is particularly important in low viscosity fluids. To test these hypotheses, we used the computational neuromechanical model outlined in the previous methods section 4.1 [47] with an additional alteration described in detail below.

Furthermore, we took the opportunity to test each hypothesis separately, assuming either purely feedforward (CPG) or purely proprioceptive neural control. In particular, the aim is to address the GABA deficient phenotypes during bouts of forward or backward locomotion, rather than changes in directional changes since the model does not include an explicit gating circuit. This is supported by the experimental finding that *vab-7* mutants (in which DB neurons differentiate as VA) and *unc-4* mutants (in which DA and VA differentiate as DB and VB) were not different from the wild type in their shrinking response to harsh head and tail touch, suggesting that the mechanism for the shrinking response is not caused by coactivation of forward and backward premotor interneurons (AVA and AVB) and is instead localized within the motor circuit.

CPG control

In the absence of detailed CPG mechanisms, it is assumed that feedforward control consists of a chain of central pattern generators, oscillating at some natural frequency. For simplicity, this form of neural activation is represented by a travelling sine wave of unit amplitude with period T_f, and wavelength, λ_f, that activates the muscles continuously along the body:

$$A(u,t) = \sin(2\pi uL/\lambda_f - 2\pi t/T_f). \tag{6.1}$$

While abstract, the CPG model does not prevent the testing of muscle inhibition, which has thus far been the main focus of research into the role of GABAergic motoneurons in *C. elegans* locomotion [132, 160]. This model is, however, agnostic to the role of neural inhibition in pattern generation itself. In this case, and in order to accommodate hypothesis 2, it is assumed that the muscle activation in the wild type polarizes more sharply than in GABA mutants. The

neural activation is therefore translated into muscle torque using a tanh function with steepness α as follows:

$$\beta(u,t) = \beta_0 \tanh(\alpha A(u,t))/\tanh(\alpha), \tag{6.2}$$

where the denominator normalizes the amplitude of the muscle activation.

Proprioceptive control

The proprioceptive model used throughout the thesis thus far has assumed that the state switches of VB and DB neurons are triggered at equal and opposite body curvature. This reductive assumption means that the neural circuit effectively only has one threshold. While this makes the model immune to the neural instabilities highlighted by the Boyle et al. model [18], it is highly unlikely that ventral and dorsal motor neurons switch state simultaneously in the real worm. In what follows, I will therefore drop this assumption and set distinct 'ON' and 'OFF' thresholds for ventral and dorsal neurons in order to accommodate hypothesis 3 (described below) and test the neural reset proposed by Boyle et al. [18].

In this version of the neural model, VB is inhibited by VD (when DB is active), producing an input current $I_{\mathrm{VD}}(u,t) = wV_{\mathrm{VD}}(u,t)$ for some inhibition strength w. However, as before, the D-type activity is absorbed into the B-type state, so if DB (or VB) is ON at some point along the body, VD (or DD) is activated. The VB and DB state switches are therefore given by the following relations:

$$\begin{aligned}
V_{\mathrm{DB}}(u,t) &\to 1 \quad \text{if} \quad I_{\mathrm{AVB}} + I_\kappa > \theta_{\mathrm{D}}^{\mathrm{ON}} \\
V_{\mathrm{VB}}(u,t) &\to 1 \quad \text{if} \quad I_{\mathrm{AVB}} - I_\kappa - I_{\mathrm{VD}} > \theta_{\mathrm{V}}^{\mathrm{ON}} \\
V_{\mathrm{DB}}(u,t) &\to 0 \quad \text{if} \quad I_{\mathrm{AVB}} + I_\kappa < \theta_{\mathrm{D}}^{\mathrm{OFF}} \\
V_{\mathrm{VB}}(u,t) &\to 0 \quad \text{if} \quad I_{\mathrm{AVB}} - I_\kappa - I_{\mathrm{VD}} < \theta_{\mathrm{V}}^{\mathrm{OFF}}
\end{aligned}$$

Clearly, the neural inhibition is a piecewise constant function in time because the neural states are binary. It is therefore reasonable to absorb the AVB current and VD current into the thresholds, meaning that the ventral thresholds effectively become dependent on the DB state since it is assumed that DB ON instantly activates VD. This would result in effective thresholds which can be directly compared to proprioceptive input with $\tilde{\theta}_{\mathrm{D}} = \theta_{\mathrm{D}} - I_{\mathrm{AVB}}$ and $\tilde{\theta}_{\mathrm{V}} = \theta_{\mathrm{V}} - I_{\mathrm{AVB}} + I_{\mathrm{VD}}$. The distinction between the motor circuit with or without neural reset essentially becomes the difference between effective ventral threshold values (see figure 7.3). In the feedback driven case, the activation to the muscles is defined as the difference between the neural inputs to the muscles:

$$A(u,t) = V_{\mathrm{DB}} - V_{\mathrm{VB}}, \tag{6.3}$$

	Description	Label	Value
Constants			
(wild type → mutant)	Muscle cross-inhibition strength	c (hyp-1)	$1.0 \rightarrow 0.8$
	Activation steepness	α (hyp-2)	$3.0 \rightarrow 2.4$
	Muscle timescale	τ_m (hyp-2)	$100 \rightarrow 120$ ms
	VD inhibition strength	w (hyp-3)	$1.0 \rightarrow 0.0$
	Curvature amplitude	β_0	10 mm^{-1}
	Frequency (ff- water, agar)	f_f	$1.6, 0.5$ Hz
	Wavelength (ff - water, agar)	λ_f	$1.5, 0.6$
Neural thresholds			
	DB ON	$\theta_\text{D}^\text{ON}$	-3.0
	DB OFF	$\theta_\text{D}^\text{OFF}$	3.0
	VB ON	$\theta_\text{V}^\text{ON}$	2.9
	VB OFF	$\theta_\text{V}^\text{OFF}$	-3.05

Table 6.1: Default parameters used in model, with changes under corresponding hypothesis where applicable.

such that positive activation encourages dorsal bending and negative activation encourages ventral bending.

Hypothesis 1 - cross inhibition

Cross inhibition of the opposing body wall muscle ensures that the excited muscle undergoes minimal resistance during contraction, which increases the overall torque experienced about the midline. In the model, the muscle forcing on both sides of the body is combined into a single muscle activation function acting along the midline of the body. Therefore, the elimination of muscle cross-inhibition effectively results in reduced activation on the bending side. To represent this, a multiplicative constant is applied to the preferred midline curvature:

$$\beta(u,t) \rightarrow c\beta(u,t) \tag{6.4}$$

with $c = 1$ in the wild type and $c = 0.8$ in the default perturbation, indicating that the muscle on the stretched side remains partially activated, providing additional bending resistance and decreasing overall torque.

Hypothesis 2 - muscle disinhibition

Disinhibition of body wall muscles increases the muscle forcing immediately after inhibition is released, which results in a sharper polarization of the muscles upon activation. To represent a lack of inhibition in GABA deficient mutants experiencing feedforward control, the sharpness of the muscle activation function is decreased by lowering the steepness parameter α in equation (6.2). By default, this value is decreased by 20% to approximately match the average difference in undulation frequency observed between wild type and GABA deficient worms during crawling.

By the same reasoning, lack of muscle disinhibition was represented in the case of feedback driven control by decreasing the timescale of muscle contraction τ_m:

$$\tau_m^{\mathrm{hyp2}} \frac{d\beta(u,t)}{dt} = \beta(u,t) + \beta_0 A(u,t) \tag{6.5}$$

where $\tau_m^{\mathrm{hyp2}} = 1.2\tau_m$.

Hypothesis 3 - neural reset

Boyle et al. (2012) [18] hypothesized that worms lacking neural inhibition will fail to undulate in water-like environments, in which wild type worms undulate at higher frequency. In this model, VB activation depends on the state of DB via the DB→VD→VB connectivity. Elimination of neural inhibition means that VB neurons are not inhibited when DB neurons are active. Worms lacking this neural inhibition are modelled by setting $I_{\mathrm{VD}} = 0$ at all times, which effectively positively shifts both VB thresholds (figure 7.3). Since the feedforward control is not modelled at the level of individual neurons, this hypothesis is only implemented in the feedback circuit. Unless otherwise stated, only one form of inhibition is removed from the model in a given simulation.

Chapter 7

Results II - The role of inhibition during locomotion

Based on the experimental results, the three hypotheses for the role of inhibition in *C. elegans* locomotion were implemented in the neuromechanical model. The first hypothesis, that D-type neurons provide cross-inhibition of the body wall muscles, was recognised in very early experimental and modeling work [132, 138, 25]. The second hypothesis, that disinhibition of the innervated body wall muscles increases muscle activation, has not previously been directly demonstrated in *C. elegans* to my knowledge. However, post-inhibitory rebound is a commonly known phenomenon in neurons capable of firing action potentials, which have been observed in *C. elegans* body wall muscles [62]. Although the current model only implements linear muscles, a proxy for the effect of a sharp increase in muscle activation upon disinhibition has been implemented. Thirdly, the hypothesis that asymmetric, phase-dependent neural inhibition promotes high frequency undulation was tested, inspired by results from the Boyle et al. model [18]. All three hypotheses were tested under proprioceptive control, however, only muscle cross-inhibition and muscle disinhibition were tested in the feedforward model, since individual neurons are not included. For both control paradigms, these hypotheses were tested in both agar-like and water-like environments, consistent with experiments [46], along with wild type simulations (with no manipulations) as a control. Since the experiments showed no qualitative difference between the mutants during forward and backward locomotion, it suffices to only test the model manipulations for forward locomotion. Moreover, changing the orientation of the stretch receptors to mimic A-type neurons produces identical locomotion in the backward direction [47], and reversing the wave speed of the feedfoward control would lead to otherwise identical results.

Under proprioceptive control, both perturbations of muscle inhibition induced a substantial decrease in undulation frequency (figure 7.1). Of these the larger frequency reduction was

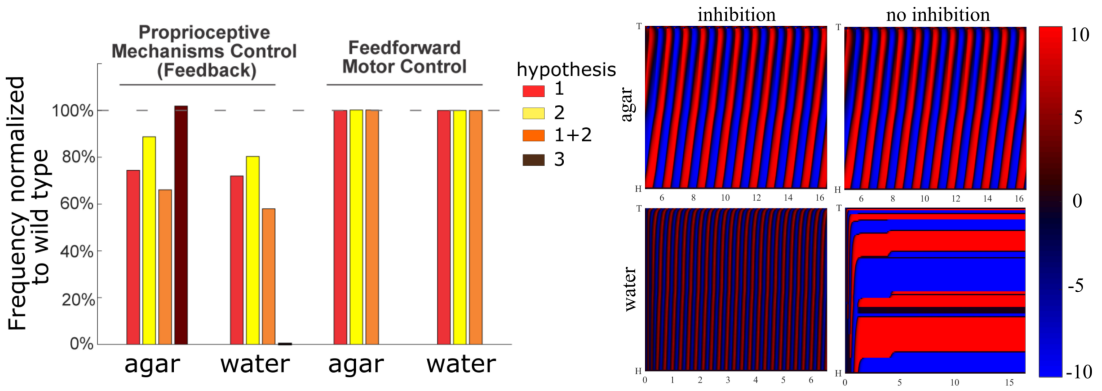

Figure 7.1: Left: Frequency of model GABA deficient worms normalised by model wild type frequency under feedback and feedforward control. Under feedback control, lack of muscle inhibition, but not neural inhibition, leads to a decrease in frequency. Feedforward control yields no significant change in frequency. Right: Kymograms showing the contribution of the neural reset in agar- and water-like environments, suggesting that neural inhibition provides robustness during high frequency undulations.

induced by disrupting cross-inhibition, with a 25% reduction in agar and a 28% reduction in water, with muscle torque reduced by 20%. However, a similar frequency reduction was shown in model mutants lacking disinhibitory rebound, with a 22% reduction in agar and a 20% reduction in water when muscle timescale was reduced by 20%. Double mutants, lacking both forms of muscle inhibition simultaneously, displayed a further decrease in undulation frequency compared to wild type (34% and 42% reduction in agar-like and liquid-like environments, respectively - figure 7.1). These results conform with intuition under the assumption of feedback driven control. Without cross-inhibition, low levels of activity in the antagonist muscle increases resistance to body bending in the agonist direction, slowing a body bend and delaying the next neural state switch. Note that this is not the same as increasing overall body stiffness, which would be associated with an increase in frequency under feedback control (section 5.2) [47]. Likewise, the initial sharp upswing in muscle activation caused by disinhibition causes neural state switches to be reached in less time compared with an uninhibited muscle. These simulations also showed a decrease in locomotion speed, which is also qualitatively consistent with experiment [46].

Reduced speeds were also observed under CPG driven undulations in response to lack of cross-inhibition. However, a lack of muscle disinhibition resulted in increased speeds, indicating that a smoother muscle activation profile over time may be beneficial in generating overall thrust. In contrast with feedback control, CPG driven simulations showed no change in undulation frequency (figure 7.1). These results suggest that the observed frequency-speed dependence is a signature of proprioceptively driven neural control.

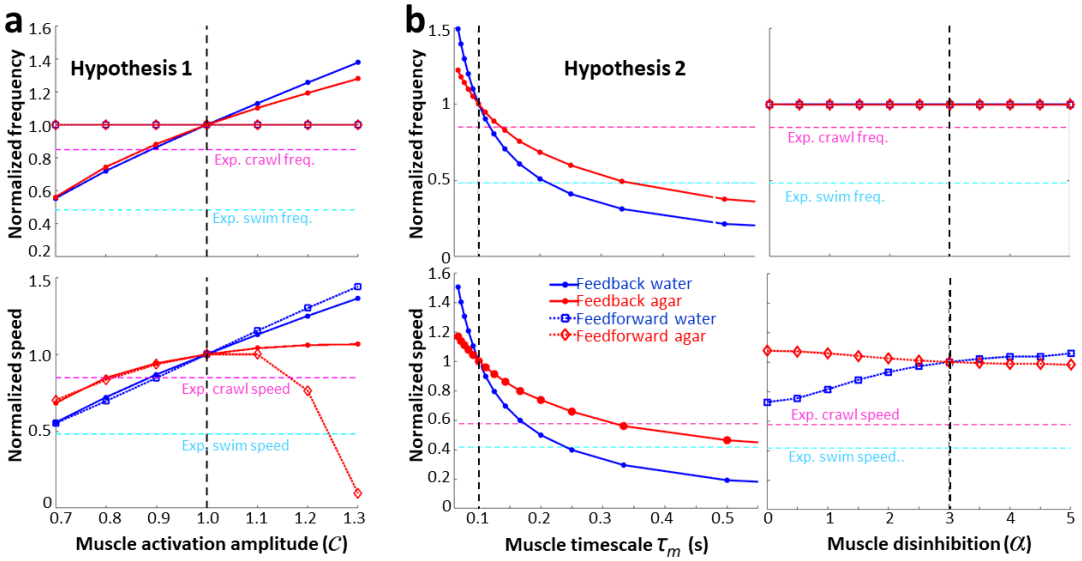

Figure 7.2: Sweeps of inhibition-related model parameters under feedback (blue) and feedforward (red) control. Vertical dashed lines indicate the default wild type value. Horizontal dashed lines represent the values measured in experiment in low viscosity (magenta) and high viscosity (cyan) environments [46]. (a) Lack of cross-inhibition effectively reduces the overall torque generated by the muscles, represented by decreasing muscle strength c. (b) Decrease in the muscle rebound due to disinhibition is represented by an increase in muscle timescale τ_m (for feedback control) or steepness in the muscle response function α (for feedforward control).

Although the muscle inhibition results qualitatively matched experiment, we were curious as to how strong inhibition would need to be to quantitatively match. I therefore performed parameter sweeps for hypotheses 1 and 2, subjecting each model to a range of inhibition strengths in water and agar-like environments. Results are shown in figure 7.2 and compared to recordings taken from *unc-25* mutants. Suppression of cross-inhibition by $\approx 8\%$ and $\approx 30\%$, respectively, quantitatively matches the decrease in undulation frequency and speed on agar observed in experiment [46]. Suppression of cross-inhibition by $\approx 33\%$ provides a quantitative match in the frequency decrease in water, possibly hinting at additional roles of inhibition. Speed and frequency changes are similar in the feedforward and feedback models under modulation of cross-inhibition strength. However, the feedforward driven model shows a slightly stronger speed modulation, despite the frequency being fixed. Increasing the effect of muscle disinhibition is modelled by increasing the timescale of muscle contraction in the proprioceptively driven model. This predicts that timescales of 120 ms and 250 ms accounts for the observed drop in frequency and speed in agar, respectively, and a timescale of 200 ms matches both measurements in water. Disinhibition in the feedforward model was modulated through changes in the steepness of the muscle activation function, with higher values steepness parameter α leading to a squarer activation pattern over time. Changes in steepness lead to opposite effects on locomotion speed in water and agar, with only small changes in agar but up to a 30% speed increase in water going from a smooth sinusoidal muscle activation to an almost square wave.

Removing the neural inhibition resulted in no significant change in undulation frequency during crawling compared to wild type (figure 7.1). However, model worms swimming in water were significantly impacted, failing to undulate and becoming frozen in an "s"-shaped posture, consistent with Boyle et al. [18]. Some body regions were frozen with either only VB activated, while others had only DB activated. However, these regions were consistently separated by thin bands for which both the ventral and dorsal B-type neurons were activated simultaneously, stalling the mechanical wave. To explain this, consider the bottom panel of the neural state schematic shown in figure 7.3. As the body undergoes a ventral bend, the DB neuron also becomes activated, causing the body to straighten out before reaching the $\theta_{\mathrm{V}}^{\mathrm{OFF}}$ threshold. With the neural inhibition intact, VD would immediately inhibit VB, allowing a smooth transition to a dorsal bend. Without this reset, some other mechanism must allow the body to continue to bend, else the model worm becomes frozen. It is likely that high viscosity environments impose a sufficient neuromechanical phase lag to delay the change in neural signal from being actuated by the muscle, long enough for the ventral OFF threshold to be reached, whereas low viscosity environments impose negligible phase lag, allowing the body to straighten quickly and become stuck. Although real worms were not completely paralysed and instead showed slow, severely uncoordinated undulations [46], this result supports the requirement of a neural reset mechanism to sustain robust high-frequency undulations.

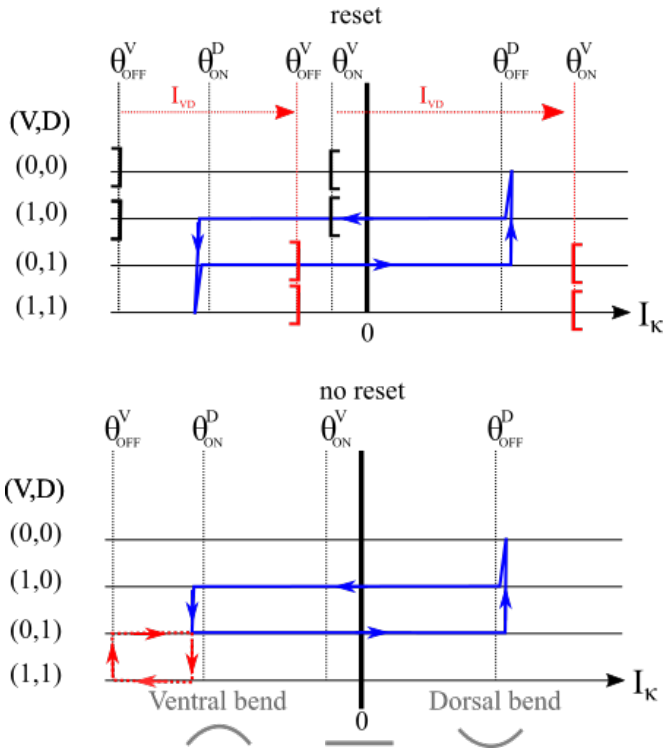

Figure 7.3: Schematic showing neural state changes of ventral and dorsal B-type neurons in response to proprioceptive input I_κ. Blue, directed trajectories illustrate the evolution of stretch input local to a neuron pair. Top: An undulation cycle including the neural reset where black and red square brackets indicate the shift in effective threshold due to VD inhibition when DB becomes activated. Bottom: The same undulation cycle without the reset. Here, some additional mechanism is required to allow the body to continue the ventral bend and deactivate the ventral neuron (highlighted in red).

7.1 Discussion

The model shows a significant decrease in undulation frequency when either muscle cross-inhibition or the effect of muscle disinhibition are reduced, assuming proprioceptively driven control. This comes with a decrease in locomotion speed, consistent with experiment. However, a lack of neural inhibition does not result in a significant change in frequency, rather a failure to support high frequency undulations while resulting in little change to crawling. The qualitative effects of the neural reset are the same as that shown by Boyle et al. [18], suggesting that this result does not depend on a decay in muscle strength along the body. Together, these results suggest markedly different roles for inhibition depending on the location within the motor circuit. GABAergic motor neurons may influence undulation frequency via neuromuscular junctions, but provide stability via asymmetric neural inhibition.

The model also shows qualitative differences between feedforward and feedback control, both in frequency modulation under muscle inhibition and speed modulation in water and agar under perturbations in disinhibitory rebound. This model does not, however, rule out any additional mechanisms for frequency modulation. In particular, the feedforward model is quite simplistic and future models could attempt to combine feedforward and feedback control to various degrees since both control paradigms have been demonstrated in the ventral nerve cord [59, 61].

The motor circuit as presented in the model assumes that the D-type neurons are activated by

the opposite B-type neurons and inhibit adjacent muscles to provide cross inhibition. This is the conventional view of their role given observed connectivity patterns [52, 191] and has been used as such in many previous models [18, 25, 47, 89, 92, 137]. However, the experimental results presented by Deng et al. [46] suggest that the activity of D-type neurons are antiphase during high frequency but correlated during low frequency undulation. This seems to suggest that their role may not purely be to follow the activation of upstream B-types, and that their activity depends on either undulation frequency or mechanical load. Indeed, recent findings do suggest that at least some D-type neurons possess mechanosensitive channels [119]. This therefore brings to question the validity of results produced by current models of *C. elegans* locomotion. The modelling results presented here, consistent with experiment [46], suggest that the D-type neurons play a more significant role during high frequency undulations where conventional wisdom seems to hold. Indeed, in the biological and model worms, the D-type neurons do not appear to be required to produce coordinated crawling but are required for faster undulations. Furthermore, it is not clear how the dorsoventral phase differences in the D-type neurons evolve over the smooth gait transition when subjected to increased mechanical load. Future modelling effort could look into the phase relationship over the course of the gait transition, and compare results for linearly responsive and mechanosensitive inhibitory neurons.

Chapter 8

Methods III - Decoupling of anterior and posterior undulations

8.1 Background

8.1.1 Research statement

The research that follows is preliminary and unpublished. It is an initial modelling response to the novel observation of simultaneous undulations of multiple frequency in *C. elegans*, and the implications of this discovery on underlying neural mechanisms. I begin by recapping experimental methodology, findings and interpretation, before using two different modelling approaches in parallel to address the findings. The first approach implements simple coupled phase oscillators, and the second adapts the full neuromechanical model used throughout this thesis to accommodate an abstraction of experimental procedures.

8.1.2 Literature recap

The smooth sinusoidal gait exhibited by *C. elegans* is ubiquitous among swimmers with elongated bodies. The question of the neural mechanisms underlying the generation and coordination of such characteristic mechanical waves remains a topic of scrutiny. In leech, electrophysiology has demonstrated endogenous rhythms in isolated ganglia whose frequency is close to that of swimming [187, 51, 106, 126]. Similarly, interneurons in the lamprey nerve cord have shown an ability to generate robust rhythms when isolated, though do not match swimming frequency [104]. In some cases additional sensory mechanisms such as stretch feedback assists in coordinating CPG activity, facilitating adjustments in gait depending on sensory cues [135].

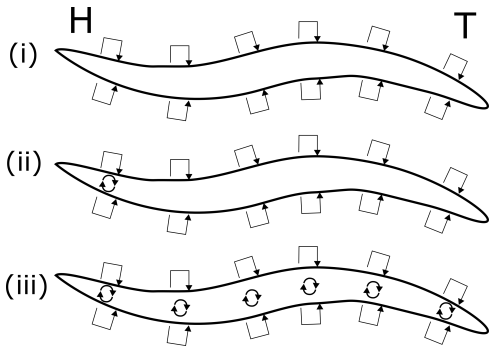

Figure 8.1: Schematics of the three neural control hypotheses for *C. elegans* forward locomotion, adapted from Gjorgjieva et al. [66]. Squared arrows represent proprioceptive feedback and cyclic arrows represent endogenous oscillators.

The source of rhythm generation during *C. elegans* locomotion remains a topic of discussion, and endogenous rhythms have not yet been demonstrated in the forward circuit. Three competing hypotheses for *C. elegans* motor control paradigms were put forward by Gjorgjieva et al. [66] as follows; (i) the motor circuit is driven and coordinated by proprioceptive feedback (ii) a head CPG initiates a bending wave which is propagated by proprioceptive feedback (iii) multiple CPGs along the body generate body bends which are then coordinated by proprioceptive mechanisms (figure 8.1). The recent finding by Gao et al. [61] that forward undulations can occur in worms lacking premotor interneurons or A-type neurons suggests that forward undulations occur due to non-A ventral nerve cord (VNC) neuron activity or the muscles. In 2017, Fouad et al. [59] sought to test the hypothesis that proprioceptive mechanisms are responsible for wave propagation along the body, reasoning that if proprioception is solely responsible for head to tail propagation, disrupting wave propagation would inhibit posterior bending. In contrast, a multiple oscillator model would manifest local wave disruption but anterior and posterior undulations would continue, perhaps less synchronously.

Fouad et al. used optogenetic manipulations to inhibit the VNC cholinergic neurons, or body wall muscles, in the neck in order to inhibit propagating body bends in that region [59]. This revealed the novel observation that the region posterior to the inhibition undulated at a significantly higher frequency than the anterior region, with both regions not matching the unperturbed frequency. This result, coined two-frequency undulations (2FU), was reproduced in multiple different ways: inhibiting the muscles, cholinergic neurons or B-type motor neurons in slightly different areas of the head and neck. The authors suggest that these results weaken hypothesis (ii) in which a head oscillator initiates a wave, which is then propagated by proprioceptive mechanisms, in favour of a hypothesis in which multiple, independent oscillators drive local undulations, increasing in frequency along the body. Furthermore, systematic ablations of motor neuron classes in the VNC (ablating, A-, VC- and D-types separately) suggest that the B-type neuron class are sufficient to produce 2FU. Occurences of 2FU were also greatly

reduced in inhibited worms in which groups of 2-6 B-type neurons were ablated, particularly in the mid body. The authors therefore suggest that B-type activity drives multiple independent oscillators whose natural frequency increases down the body and may be entrained via proprioception. However, it is difficult to conclude that such oscillators are endogenous while the motor circuits remain embodied.

Finally, the reduced head frequency and increased tail frequency during optogenetic inhibition suggest that frequency entrainment arises through bidirectional coupling, though the relative effects of the neural circuitry and body mechanics on the entrainment are unknown. Although B-type neurons alone may be responsible for primitive forward undulations [61], their processes extend strictly posterior to their cell body. However, experiments by Wen et al. involving physical clamping showed that posterior body sections match the imposed curvature in anterior sections [188], indicating the existence of an anterior proprioceptive field. Xu et al. tested the role of environment by optogenetically inhibiting the midbody of worms locomoting through Newtonian fluids of different viscosities [194], finding that the difference in undulation frequency between freely moving and inhibited worms was larger in more viscous environments. They observed a posterior frequency of 0.8 Hz in unperturbed worms in viscosities of 10^3 mPas, which rose to 1.6 Hz when optogenetically silencing anterior B-type neurons, compared to a much smaller difference in water ($\approx$ 1 mPas), in which frequency rose from 1.6 Hz to 1.7 Hz. In a proprioceptive model this decrease in frequency difference may simply arise when mechanical and neural timescales become comparable [92]. Alternatively, the relatively small change in posterior frequency over a range of viscosities may be explained by an intrinsic oscillator which slows in response to anterior B-type neuron activity [194].

These experiments provide an opportunity to explore the hypotheses of *C. elegans* neural control using a computational model. In this section I intend to reproduce some of the experimental methods mentioned above under the assumption of purely proprioceptive control (independent of central pattern generators) to understand if any of the described results may be explained. I will introduce additional methodology in order to implement muscle inhibition over various body regions of the neuromechanical model (section 8.3), but first I will provide further context to my approach using a simple phase oscillator model example.

8.2 Oscillator model

The purpose of this section is to demonstrate the concept of synchrony versus detuning which is key to understanding the experimental results discussed in the previous section, and will facilitate my interpretation of the neuromechanical model manipulations in the following sections. Here, I use two coupled Kuramoto oscillators as the most simplistic and tractable model of coupled oscillators (See section A.2 and references therein for more background on phase oscillators including the Kuramoto model).

The experiments of Fouad et al. [59] described in section 8.1.2 suggest a model of the motor circuit in which two or more oscillators drive undulations, and that their uncoupled frequencies (when separated by inhibition) increase from head to tail. I will therefore consider the oscillating body regions anterior and posterior to an inhibited region as individual oscillators with independent natural frequencies described by periodic phases ψ_{A} and ψ_{P}, respectively. To maintain the assumption of the neuromechanical model that body bends are driven by posterior body curvature or stretch due to the directionality of the proprioceptive field, I will assume that the anterior oscillator is being driven by the posterior oscillator. The natural frequency of the posterior oscillator, ω_{P}, is set to that of the anterior frequency, ω_{A}, plus some detuning δ such that $\omega_{\mathrm{P}} = \omega_{\mathrm{A}} + \delta$ and the coupling function takes the form $\sin(\psi_A - \psi_P)$. The *detuning* δ pulls the anterior oscillator away from it's natural frequency. This system can then be written as

$$\begin{aligned}\frac{d\psi_A}{dt} &= \omega_A + \epsilon \sin(\psi_P - \psi_A)\\ \frac{d\psi_P}{dt} &= \omega_P.\end{aligned}$$

Immediately, this can be re-written in terms of phase difference $\phi = \psi_A - \psi_P$, so the equations reduce to

$$\frac{d\phi}{dt} = \delta - \epsilon \sin(\phi). \tag{8.1}$$

Fixed points of equation (8.1) correspond to frequency locked states where the difference between phases remains constant for all time. The fixed point $\phi^* = -\sin^{-1}(\frac{\delta}{\epsilon})$ is stable if $-\epsilon\cos(\phi^*)) < 0$ and unstable otherwise, so the synchronous state is stable when it exists. Therefore the key parameter is the ratio of detuning to coupling strength for a given coupling function. If detuning is stronger than coupling ($\delta > \epsilon$), no fixed point exists and the oscillators fail to entrain. This can be seen in figure 8.2 where predicted and simulated fixed points fail to match, and the oscillator frequencies drift away from one another. Note that if the coupling were bidirectional, the fixed point equation (8.1) would take the general same form, except that the coupling strength would effectively double.

Phase models such as this are a simple way to study interactions between oscillators due to their coupling. Often the coupling is calculated using a more biologically grounded model of an individual oscillator (see section A.2). Note that here the coupling function is *not* calculated via measurements taken from the full neuromechanical model. However, using a sine function and keeping $\epsilon > 0$ ensures that the stable state is synchronous, corresponding to the fact that the anterior and posterior body regions oscillate at the same frequency if coupling is strong enough compared to the detuning (for example, no inhibition in the midbody). It may be possible to relate this result to our neuromechanical model when the anterior and posterior

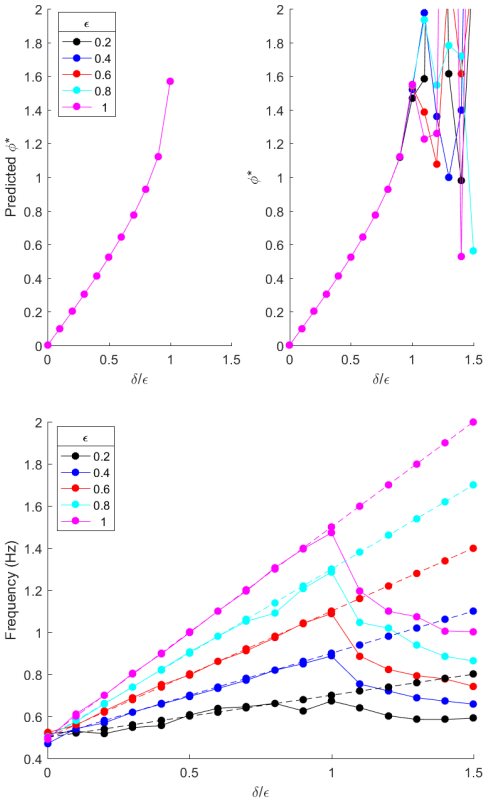

Figure 8.2: Numerical simulations of the coupled phase oscillators. Left: predicted vs actual fixed points in anterior to posterior phase difference. Right: output frequency of anterior (solid lines) and posterior (dashed lines) oscillators. Loss of entrainment between the two oscillators occurs when detuning becomes stronger than coupling.

sections of the simulated worm undulate at different natural frequencies. The body elasticity and proprioception respectively act as mechanical and neural coupling between body regions, and detuning of anterior frequency comes from a decrease in neural threshold θ along the body, leading to higher frequency in the posterior. Thus I can investigate the relationship between coupling and detuning in the full model and attempt to compare conditions of entrainment to experimental data.

8.3 Neuromechanical model

8.3.1 Optogenetic inhibition of the muscles

In experiment, optogenetic methods were used to inhibit either cholinergic neurons in the ventral nerve cord, B-type neurons, or body wall muscles. Inhibiting any of these targets in the 'neck' region resulted in 2FU to varying degrees, however, the largest differences in head and tail frequency were consistently reported when inhibiting the body wall muscles. For this reason I will focus on the case of locomotion under muscle inhibition in this preliminary investigation. In the neuromechanical model, the spatiotemporal function $\beta(u,t)$ imposes a desired midline curvature due to the torque applied about the midline by the relative contraction and relaxation of dorsal and ventral muscles. In order to inhibit the muscles of the model worm within some body region, I assume that the dorsal and ventral muscles are no longer capable of producing an overall torque. I apply a multiplicative constant $\beta(u,t) \rightarrow c(u)\beta(u,t)$ which is set to zero in a desired region $u \in [C_A, C_P]$, and $c = 1$ otherwise. Here, C_A and C_P represent the anterior and posterior limits of the inhibited region, respectively. I will also maintain the nomenclature of a previous section (section 5.2) in which the anterior and posterior proprioceptive range are represented by δ_a and δ_p, respectively. Throughout, I will refer to anterior (or head) frequency and posterior (or tail) frequency as the undulation frequency measured at $u = 0.1$ and $u = 0.9$, respectively.

8.3.2 Threshold modulation as a neural mechanism for detuning

The section on neural modulation of gait (section 5.2) demonstrated the dependence of undulation frequency on neural threshold; higher threshold leads to lower frequency undulations. So far, neural threshold has been a constant parameter along the body. However, in order to investigate the relationship between coupling strength and frequency detuning in the inhibited and freely moving worm, this parameter can be made dependent on body coordinate $\theta = \theta(u)$. This will be done in two different ways, as shown in figure 9.3, both of which maintain the default threshold value at the anterior limit, $\theta(0) = 3$: Firstly, a graded threshold which decays linearly along the body, and reaches some posterior threshold at the tip of the tail according to the rule $\theta(u) = \theta - u(\theta - \theta_\mathrm{P})$ such that $\theta(1) = \theta_\mathrm{P}$. Secondly, a step threshold profile which takes some point along the body u^* (ideally within the inhibited region) and sets $\theta(u) = \theta$ for

$u \leq u^*$ and $\theta(u) = \theta_{\mathrm{P}}$ for $u > u^*$.

The graded thresholds can be interpreted as AVB signal decay along the body, or increased neuron sensitivity. In either case, the result is feedback driven oscillations with gradually increasing natural frequency along the body. An argument can also be made that, for proprioceptively driven locomotion, this decay in threshold could reflect a decay in muscle efficacy along the body since feedback amplitude is reduced by lower body curvature. Indeed *C. elegans* does display decaying undulation amplitude during forward locomotion. The step threshold case is more similar to the coupled oscillator model of the above section 8.2, in which anterior and posterior regions possess distinct natural frequencies dictated by their own respective neural threshold. Unless otherwise stated, all parameters take their default values as given in table 4.1 with drag coefficients set to that of an agar like environment.

Chapter 9

Results III - Multiple frequency undulations

9.1 The relationship between proprioceptive range and width of inhibited region

In the above mentioned experiments [59, 194] the majority of optogenetic inhibition was directed at anterior regions of the body, with anterior limits between $15 - 25\%$ and posterior limits between $30 - 45\%$ of the body length, with a typical width of 15% or 20%. No significant behavioural difference was reported when comparing optogenetic inhibition of body wall muscles, cholinergic motor neurons or B-type motor neurons within these ranges: all manipulations resulted in two-frequency undulations (2FU) [59]. As an initial test, I inhibited the muscles of the model worm starting at 20% and 30% the body length, for regions of varying widths and simulated locomotion for one minute. All simulations were performed in an agar-like environment using the default parameter set given in the methods section 4.1, unless otherwise stated. So far the model worm has had a default proprioceptive range of $\delta_{\mathrm{p}} = 0.5$ since this range best reproduces gait modulation, but the effective proprioceptive field of *C. elegans* is not well understood. Wen et al. [188] suggest that body curvature is influenced by a receptive field of $\approx 10\%$ of the body length in the anterior direction, although the B-type processes extend roughly 20% of the body length posterior to the cell body. Since the receptive field will likely influence the effect of the inhibition, these simulations were repeated for multiple proprioceptive ranges $\delta_{\mathrm{p}} \in [0.1, 0.5]$, with results shown in figure 9.1.

Unsurprisingly, if the width of the inhibited region exceeds the proprioceptive range then anterior undulations fail. If the range exceeds this width, undulations take place either side of the inhibited region with weak passive waves propagating through this region despite the inhibition, as reported in Fouad et al. [59]. This intuitive range-width relationship is broken for

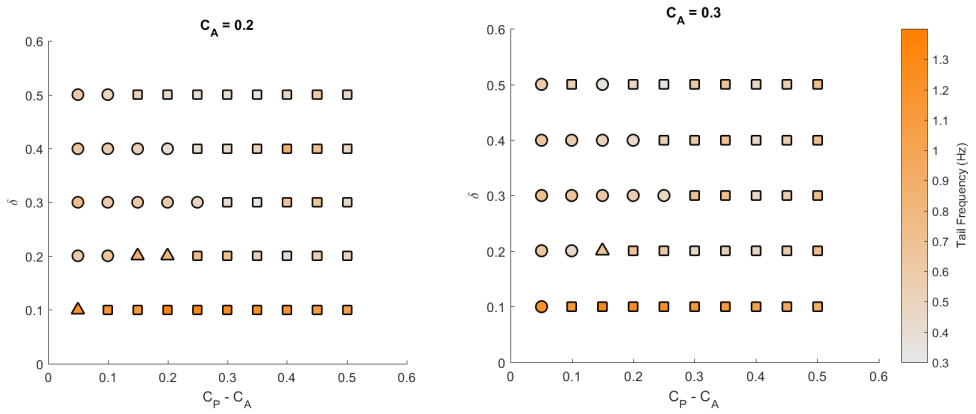

Figure 9.1: Results from muscle inhibition with different widths of inhibited region (x-axis) and posterior proprioceptive range (y-axis), for inhibited regions starting at 20% (left) and 30% (right) down the body length, coloured by posterior frequency. Markers represent simulations in which anterior regions display healthy undulations (circle), uncoordinated undulations (triangles) and no undulations (squares). Posterior regions always displayed healthy undulations.

longer proprioceptive ranges, for which anterior undulations fail despite receiving some input from the posterior region (figure 9.2). This may be because distal input from the posterior to the anterior region is out of phase with local input, so anterior and posterior contributions cancel, (with little contribution from the inhibited region) so neural threshold is never reached. Consequently, the behaviour of worms with long and short effective proprioceptive ranges under inhibition are difficult to distinguish, except for their differences in undulation frequency.

Since the anterior most limit of inhibition does not effect model behaviour (consistent with experiment), I will set $C_A = 0.2$ with a width of 20% in all following model tests. I will also set a new proprioceptive range of one fifth of a body length ($\delta_p = 0.2$, unless otherwise stated) which matches the length of the B-type processes in the biological worm while resulting in higher frequency undulations towards the tail, more closely matching the observations of Fouad et al. [59].

9.2 Model exhibits bidirectional frequency entrainment

After choosing which region of the body to apply inhibition, I sought to test the response of the model to various frequency detuning strengths. Frequency detuning in the neuromechanical model can be quantified by considering the undulation frequency imposed by values of the neural threshold, calculated in the previous section (section 5.2), as the natural frequency. Deviations from this frequency are due to the influence of coupling from neighbouring body regions. Of course, the optogenetic inhibition also contributes to detuning. I am most interested in cases that show frequency entrainment between anterior and posterior body regions

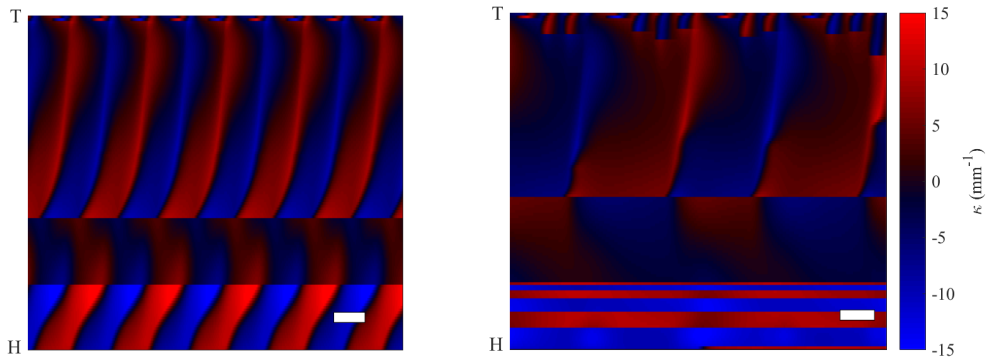

Figure 9.2: Kymograms showing simulations of locomoting worms with proprioceptive range $\delta_{\mathrm{p}} = 0.4$ for inhibited regions [$\mathrm{C_A}$,$\mathrm{C_P}$] = [0.2, 0.4] and [0.2, 0.45], showing no anterior undulations for the latter.

in the absence of inhibition, but a clear separation of frequencies when the inhibition is applied [59]. Coupling strength is more difficult to quantify directly but can be inferred by the strength of detuning at which frequency entrainment fails, as demonstrated in the phase oscillator example (section 8.2). Intuitively there are multiple contributing factors to the coupling of oscillations between body regions including proprioceptive coupling (the drive of motor neurons from posterior, and possibly anterior, body bends), mechanical coupling e.g. higher body stiffness strengthens coupling between nearby body regions, and forces imposed by high viscosity environments. The latter of these may not be as relevant here. Since we model environmental drag using resistive force theory, the forces applied to each 'point' along the body are considered independent. In other words, the drag imposed on one body region does not affect that imposed on distal body regions.

To compare frequency detuning for different coupling strengths, I ran minute long simulations in which the crawling model worm is inhibited for the final 45 seconds in the region 20%-40% for worms with a graded neural threshold and step threshold. In each case, the posterior threshold θ_{P} was incrementally increased to strengthen the frequency detuning in the anterior and posterior of the body (figure 9.3). In freely moving worms with both graded and stepwise threshold profiles, the undulation frequency in the anterior and posterior are synchronised for sufficiently weak detuning. Intuitively, the step profile provides the weaker coupling since a lesser detuning is required to decouple anterior and posterior undulations. In both cases, the synchronous frequency is above that of the control case in which a constant threshold takes the default value ($\theta = 3$), indicating that the higher frequency in the posterior can entrain anterior undulations, even with a strictly posterior proprioceptive field. This is indicative of a role played by the body mechanics during entrainment. However, the coupled frequency is also below the control frequency for corresponding posterior threshold values, indicating that

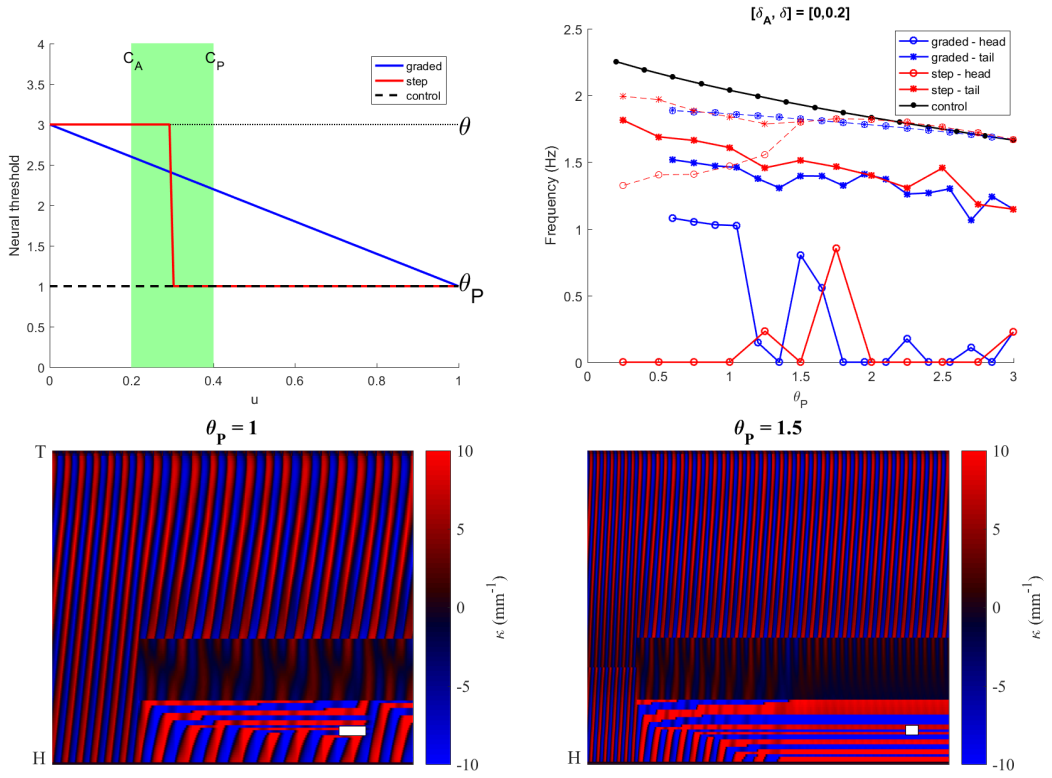

Figure 9.3: Top left: schematic of graded and step threshold profiles along midline index u, including control threshold $\theta(u) = \theta_{\mathrm{P}}$. Top right: head and tail frequency from freely moving (dashed lines) and inhibited (solid lines) worms with a strictly posterior proprioceptive field. Solid black line shows control frequency for corresponding posterior neural threshold. Bottom: Curvature kymograms showing graded (left) and step (right) thresholds, initially freely moving before onset of muscle inhibition. White bars indicate one second. Simulations corresponding to these kymograms are shown in Movies 3a and 3b (Appendix (section A.4).)

anterior undulations also entrain posterior undulations. This suggests a phase-locking through bidirectional coupling, qualitatively matching experimental results [59].

Upon inhibition, head undulations cease in almost all cases due to the strictly posterior proprioceptive range, which matches the width of the inhibited region. Tail undulations continue, but with a lower frequency than that of identical but freely moving worms. For worms with graded thresholds at sufficiently high detuning, both head and tail undulations are maintained and are decoupled. This is a partial qualitative match to experimental observations, but even in these cases the undulation frequency both sides of the inhibited region is lower than in freely moving worms.

9.3 Muscle inhibition qualitatively reproduces 2FU

To address the failure in anterior undulations, it is possible that a head oscillator initiates a bending wave which maintains head movement during inhibition. However, the current purpose is to ask how much can be achieved purely through proprioceptive drive. An extended posterior proprioceptive range is not supported by the anatomy, but there is some evidence supporting the existence of anterior stretch sensitivity [188]. Because of this, I chose to shift the proprioceptive field toward the head by one tenth of a body length making the new receptive field 10% either side of the B-type soma ($[\delta_{\mathrm{a}}, \delta_{\mathrm{p}}] = [0.1, 0.1]$), which incorporates Wen et al's results [188] while maintaining the overall proprioceptive range. I then repeated the above tests, the results of which are displayed in figure 9.4.

With a bidirectional proprioceptive field, all undulations appear more robust, with no body regions failing to propagate a wave. Both the graded and step threshold profiles show anterior-posterior synchrony for almost all detuning strengths absent of inhibition. The synchronised, uninhibited frequency is a closer match to the control simulations with default threshold value $\theta = 3$ than the corresponding posterior threshold (θ_{P}), indicating that the posterior body region is much more strongly entrained by the anterior region than vice versa. Comparing this result to the model worms with a strictly posterior proprioceptive range suggests that neural coupling has a stronger effect than mechanical coupling.

Imposing the muscle inhibition clearly shows the strengthened frequency coupling resulting from a partially anterior proprioceptive range, since body regions anterior and posterior to the inhibited region remain synchronised for weak detuning. In the graded threshold case, a posterior threshold of at most $\theta_{\mathrm{P}} = 1.7$ causes desynchronisation, indicating that the natural frequency in the tail must be 20% higher than the head to achieve 2FU. The step threshold profile desynchronises upon minimal detuning such that the tail frequency is higher than an identical freely moving worm, and the head frequency is lower, qualitatively matching the observations of Fouad et al [59]. From this, the model suggests that proprioceptively driven motor neurons can reproduce multiple frequency undulations under inhibition, and that a stepwise difference in either upstream input or neural sensitivity between body regions accentuate the detuning.

9.4 Discussion

In the combined works of Wen et al. [188] and Fouad et al. [59] numerous effective clamping techniques have been demonstrated including physical clamping of the body and optogenetic inhibition of the muscles and various excitatory motor neurons. All optogenetic inhibition appears to result in the emergence of multiple frequency undulations whereas physical clamping reportedly does not, even if the clamp width exceeds the proposed stretch receptive range [188].

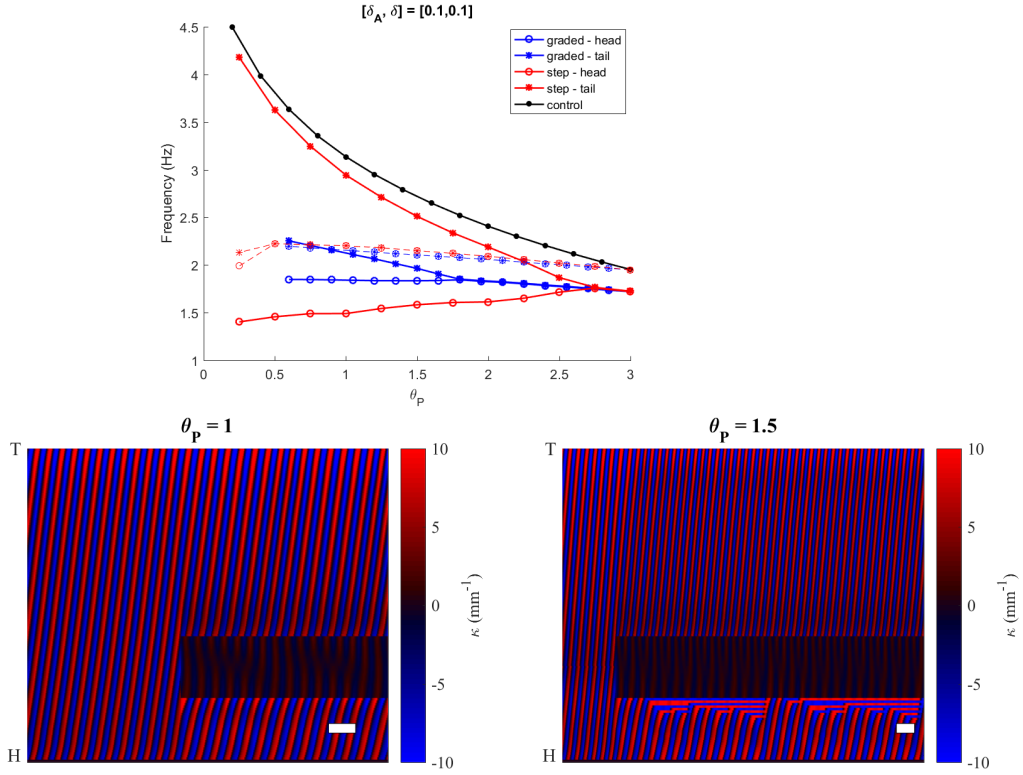

Figure 9.4: Top: Head and tail frequency from freely moving (dashed lines) and inhibited (solid lines) worms with both anterior and posterior proprioceptive field. Solid black line shows control frequency for corresponding posterior neural threshold. Bottom: Curvature kymograms showing graded (left) and step (right) thresholds, initially freely moving before onset of muscle inhibition. In the step threshold case, head frequency is reduced upon inhibition and tail frequency is increased. Simulations corresponding to these kymograms are shown in Movies 4a and 4b (Appendix (section A.4).)

It may be that the disruption of non-proprioceptive neuromuscular signaling contributes to wave propagation. However, Fouad reports 2FU even in worms with ablated premotor interneurons other than AVB (PVC, AVE, AVA and AVD) and in unc-7 unc-9 cross mutants in which AVB to B-type gap junctions and inter-muscle gap junctions are disrupted. Furthermore, an electrophysiological model by Boyle et al. [19] suggests that inter-muscle gap junctions do not significantly contribute to wave generation or propagation. One should also consider that this difference in experimental outcome may be due to flaws in the methodology itself. For example, it may be the case that physical clamping allows the worm to slip as it undulates, effectively shortening the clamping width or unintentionally changing the location of clamping along the body over an undulation. This reasoning, however, does not explain the absence of tail undulations under physical clamping.

Three competing hypotheses for *C. elegans* motor control were put forward by Gjorgjieva et al. [66]; (i) the motor circuit is driven and coordinated by proprioceptive feedback (ii) a head CPG initiates a bending wave which is propagated by proprioceptive feedback (iii) multiple CPGs along the body generate body bends which are then coordinated by proprioceptive mechanisms. The preliminary results shown here indicate that disruption of undulations via muscle inhibition does not necessarily lead to propagation failure, even in absence of intrinsic oscillators. Even if the width of the inhibited region exceeds the proprioceptive range, both anterior and posterior wave propagation may continue, though these undulations are more robust if the proprioceptive field is bidirectional. If the B-type motor neurons are the sole generators of bending waves during forward locomotion, this model suggests that inhibiting the neck may lead to anterior paralysis since the B-type processes are strictly posterior facing. This may be saved however, with the addition of a head CPG. It may be enlightening to repeat the above simulations with an additional rudimentary head oscillator to test hypothesis (ii) more explicitly.

Many other experiments were performed in the above studies which may help narrow down the possibilities of motor control paradigms in *C. elegans*, which have not yet been tested in the model. Future modelling work should implement different methods of wave disruption administered to the real worm including physical clamping. Wen et al. shows that physical clamping of the midbody results in tail paralysis [188], and Fouad et al. report tail paralysis under optogenetic inhibition between 50%-65% of the body length (though this data was not shown). My model results thus far do not predict tail paralysis assuming the worm is performing forward locomotion, though head paralysis is shown. However, given the morphological symmetry of the forward and backward circuitry, A-type motor neurons extend similar processes in the anterior direction. Thus, if physical clamping triggers a reversal, proprioceptive drive could explain tail paralysis. Furthermore, a chain of CPGs would not be expected to exhibit tail paralysis during either forward or backward locomotion when the midbody is clamped. It may also be possible to investigate ventral nerve cord lesioning in the model by cutting off proprioceptive feedback and AVB input (perhaps in the form of neural threshold reduction) at various body

points. Fouads lesioning generally lead to anterior paralysis and posterior undulations with the caveat that the head was damaged using a hot platinum wire to silence head undulations. This neuromechanical model is extensible and robust enough to complement such rich experimental results and shed further light on *C. elegans* neural control.

Chapter 10

Conclusions and future work

Animal locomotion requires coordinated motor output to drive a sequence of internal forces which in turn depend both on active and passive mechanical material properties, and the surrounding environment. It is therefore appropriate to integrate each of these factors in order to gain an overall picture of locomotion. *C. elegans'* simple anatomy and nervous system provides an excellent opportunity to combine each component within a modeling framework, drawing on knowledge of the connectome and our current understanding of the body mechanics and neuronal properties. The neural mechanisms are not fully understood, but modelling and experimental evidence for both central pattern generated and sensory driven control have been demonstrated in the ventral and dorsal nerve cords. In this thesis, I mostly focused on proprioceptively driven control to reproduce existing observations and generate new experimental predictions.

10.1 Conclusions

By increasing external drag coefficient from water-like, through intermediate to agar-like conditions, I demonstrated that a simplified neuromuscular model embedded in a continuous elastic shell is capable of qualitatively reproducing gait adaptation, with a quantitative match to experiment with the addition of internal viscosity. By comparing the saturation of kinematic parameters in the model with those observed in experiment, I was able to estimate the Young's modulus of the worms outer shell ($E \approx 100$ kPa), which turns out to be in line with a similar feedforward driven model [37]. The model highlights a key relationship between external drag and body elasticity, depending on the body dimensions, which provides more general picture of the conditions required for mechanical gait modulation ($e < 1$), or saturation ($e > 1$). I also highlight a non-monotonic relationship with the ratio of elasticity and internal viscosity and undulation wavelength, with maximum wavelength resulting when this ratio matches time scale of muscle contraction, consistent with predictions from another recent model [92]. This

ratio is shown to be another key parameter, which limits undulation frequency when mechanical timescales dominate physical timescales, with a quantitative experimental match when $E/\eta \approx 10$ sec^{-1}.

By modulating characteristics of proprioceptive motor neurons in different environments, I drew a novel qualitative distinction between mechanically induced and neurally induced modulation of gait. Specifically, mechanical modulation, either by changing drag coefficients or muscle tone, reliably produces a positive frequency-wavelength relationship, whereas neural modulation, either by upstream command input, stretch sensitivity or adjustments in the proprioceptive field, produces a negative relationship. In particular, this highlights an experimental prediction that the frequency-wavelength relationship upon neural stimulation of the forwards and backwards circuits (perhaps by optogenetic manipulation of AVB and AVA inter neurons, respectively), may be different if their primary driving mechanisms are in fact different. Testing of the proprioceptive field also gave way to a bonus result, that an effectively bi-directional proprioceptive field appears to abolish the uncoordinated simulations shown by both the Boyle et al. [18] model and the current model. However, this does appear to have an impact on the available range of postures over different environments. Nonetheless, this represents a key step in the right direction for future models to perfect and further understand the gait transition.

By specifically targeting different locations of GABAergic inhibition in the nerve cord, the model shows that inhibitory connections at the neuromuscular junctions may also be a mechanism for frequency control, by which stronger inhibition encourages higher undulation frequencies in both water and agar. Again, this is a potential indicator of proprioceptive control since a reduction in overall muscle torque due to lack of cross-inhibition of the muscles results in a decrease in bending amplitude, which has some equivalency to switching threshold in the model. The model also suggests that the role of muscle inhibition and neural inhibition of cholinergic motor neurons are fundamentally different. While the former supports higher frequency undulation, the latter appears to be essential for robust wave propagation in low viscosity media, qualitatively consistent with experiment [46]. I have postulated that the magnitude of neuromechanical phase lag may be key in understanding why the neural reset is essential. In more viscous environments, this phase lag is much larger such that the body may spend more time bending after dorsal and ventral neurons become simultaneously activated, allowing for VB to turn off and reset the undulation cycle. However, further work is required in order to further explore this line of thinking.

Recent experiments optogenetically inhibiting neurons and muscles in the anterior portion of the body result in multiple frequency undulations along the worm [59, 61, 194]. This may indicate the existence of multiple distributed oscillators, driving body bends at increasing natural frequencies along the body. Testing inhibition of the muscles in anterior regions of the model worm indicate that multiple frequency undulation can arise under feedback driven control. Furthermore, this model behaviour qualitatively matches that of experimental observations. These

preliminary results indicate that although endogenous oscillators may exist in the backward circuit [61], they are not necessarily required to produce two-frequency undulations during forward crawling.

This thesis was presented as three broad parts, presenting results on neuromechanical gait modulation, neural inhibition and multiple frequency undulations, respectively. It should be noted that the latter two parts introduced subtle yet key changes to the model. The question then arises as to whether these changes would affect the initial results on gait modulation. In order to study neural inhibition (part II), I introduced a 'neural reset' mechanism into the motor circuit based on the model of Boyle et al. [18]. This implementation essentially made the on and off VB thresholds dependent on the state of DB neurons since the inhibition from D-type neurons, which were modelled implicitly throughout, effectively increases the ventral thresholds such that a stronger excitatory current would be required to cause a state change. Before this was implemented (in part I) the dorsal neurons were assumed to be dominant such that DB switching on/off instantly lead to VB switching off/on. The difference in output between each model during locomotion is only apparent in the absence of the neural reset (as shown in figure 7.1). With the neural reset present, both crawling and swimming behaviours are readily reproducible with a smooth transition through intermediate environments. As for the model used in part III to study multiple frequency undulations, both linearly graded and stepwise spatial profiles were introduced in place of the constant neural threshold along the body. The graded threshold does not qualitatively alter any of the gait modulation results (not shown), although clearly the frequency is slightly, but not significantly, increased. This addition would in fact improve the appearance of locomotion in the model, for example, the Boyle et al. model included a similar graded function described as "decreasing muscle efficacy" which provided the more realistic decaying amplitude seen during locomotion in the real worm [18]. Such an addition could well appear in future model iterations. The abrupt change imposed by the stepwise threshold does not guarantee stable, coordinated oscillations throughout the gait transition. Preliminary testing with this threshold profile (not included in the thesis) suggest a failure to entrain anterior and posterior undulations specifically in a low viscosity medium. It was shown in Section I that the difference in undulation frequency between low and high neural threshold is much greater in less viscous environments, so it is not so surprising to see detuning here.

10.2 Future work

The current model has been used to explore a wide variety of experimental assays and results, and has great potential to incorporate much more. For example, the mechanical model component has recently been extended to 3D by including a description of body twist [154], which enables the potential for a detailed study of 3D steering circuitry in the head and neck. There is, however, plenty left to explore within the 2D model framework.

Although the model quantitatively captures modulation of frequency and wavelength, the reader will notice from the supplementary movies that wave amplitudes appear to be slightly too high. This is most likely due to the simplifications made to the circuitry in order to study locomotion in a maximally reductive setting. As a consequence, the speed of model worm locomotion also tends to be on the high end. I imagine that incrementally reintroducing the additional neuromuscular functionality present in the Boyle et al. model [18] would recover these additional locomotive metrics.

A caveat shared by both models is the requirement for the extended, and physiologically unrealistic, proprioceptive range of half the nematode's body length to reproduce the full range of gaits observed. It is possible that the simplistic assumptions of instantaneous and linear proprioceptive feedback is responsible for such a requirement. In which case, implementing spatiotemporal feedback, or some nonlinear stretch response may allow for a reduction in the range while maintaining the locomotion kinematics. Alternatively, the current formulation could be loosely interpreted as an effective range approximating an amalgam of different stretch sensitive neurons. This could be tested by introducing additional connections between adjacent proprioceptive neurons along the long body axis, possibly including known proprioceptive neurons outside the core circuit such as DVA.

So far the model has proved quite successful in offering novel signatures of proprioceptive control. However, numerous interesting mutations exists whose effects are local to neurons thought to possess stretch receptors. For example, in *vab-7* mutants the processes of only the dorsal B-type neurons extend anterior, rather than posterior to the soma, which results in an overall ventral bending bias exclusively towards the tail [188]. The *unc-4* mutation causes A-type motor neurons to differentiate as B-type motor neurons. An investigation into the *vab-7* mutation may prove insightful, but this may require a minor extension to the muscle control to allow for independent activation on the ventral and dorsal sides, rather than absorbing the relative contributions in an overall torque about the midline. Furthermore, while the model is readily capable of incorporating both forward and backward locomotion circuits, there is no dedicated gating circuit in the head to mediate switching between the two circuits. Multiple experiments have highlighted the potential role of both reciprocal inhibition and mixed electrical-chemical synapses between AVA and A-type neurons to provide a forward locomotion bias [118, 117]. It is possible to accommodate such a mechanism in the neuromechanical model in order to work toward a complete picture of both forward and backward locomotion in *C. elegans*.

Finally, both spatial and temporal manipulations in the drag coefficients could be used to reproduce experimental assays such as placing worms in microfluidic channels [46] or physical clamps [188]. For example, setting the normal drag component to a high value over specific body regions may reproduce the effects of physical clamping, which Wen et al. [188] show does not lead to two-frequency undulations whereas neuromuscular manipulations over the same

regions do [59]. Worms places in sinusoidal channels which manipulate the worms body to produce shorter wavelength, show corresponding lower frequencies, even when the channels are filled with low viscosity buffer solution. This is a new scenario demonstrating the kinematic coupling, and it would be interesting to see if the model worm produces the same result.

Appendices

Appendix A

Appendix

A.1 Computing kinematic parameters

For convenience, simulation inputs and outputs are converted to dimensional units, as appropriate. All simulations were performed for 60 seconds using integration time steps of 0.3 ms for feed-forward control and 0.03 ms for proprioceptive control. The transients in some simulations were negligible (<1 s) but others varied significantly with model parameters. Before analysis, all transients were truncated to limit the data to only periodic activity.

Frequency:

The period of undulations, T, was computed from curvature kymograms (see figure below). The period was defined as the mean time interval between zero crossing of the body curvature $\kappa(u,t)$ at body coordinate $u = 0.1$ (from negative to positive values). This is acceptable since during coordinated locomotion, the period of undulation does not depend on the position along the body, and even in uncoordinated simulations, anterior frequency appears stable. The frequency of undulations is then given by $f = 1/T$. The same process is applied to measure tail frequency, only at body coordinate $u = 0.9$, 10% of a body length from the tail tip.

Wavelength:

In the feedback driven model (as in experimental observations), the undulation wavelength increases along the body (from head to tail). Undulation wavelength if defined as the distance along the midline required to span a full cycle of body curvatures [14]. This does not necessarily align with the more conventional definition of a wavelength, which is the distance between successive crests of a wave. Note that for sufficiently low viscosity environments, the wavelength is longer than the body length. Wavelength is measured by calculating the gradient of the curvature $\kappa(u,t)$ as a function of body coordinate u and time t within a section of the body. Towards the tip of the tail the value of the wavelength changes. This may be due to a combination of boundary effects and decreasing proprioceptive range. The posterior third of the body is therefore excluded in the measuring of wavelength, which is defined as

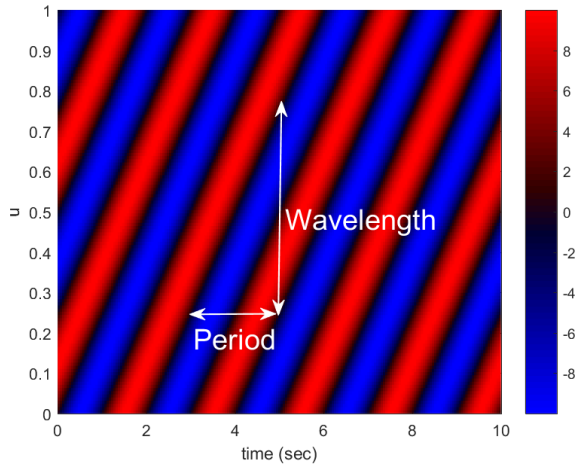

$$\lambda = T \frac{\partial \kappa / \partial u}{\partial \kappa / \partial t} \tag{A.1}$$

over the region $u \in (0.1, 2/3)$. A small amount of filtering of the curvatures ensured that the derivatives are well approximated using a finite difference. An average was taken across u and time t using a histogram mode with logarithmically distributed bins.

Speed:

Speed was computed by tracking the midpoint of the nematode's body ($u = 0.5$) over time, and performing a straight line fit over the midpoint trajectory to remove side-to-side displacement arising from the undulatory movement. The speed was then defined as the distance travelled along the straight line over the corresponding time interval.

A.2 Phase oscillators

Phase oscillators are a popular class of model which describe the state of an oscillating system using only the phase of the cycle. Consider an autonomous system with n variables:

$$\frac{d\mathbf{x}}{dt} = F(\mathbf{x}) \qquad \text{where} \qquad \mathbf{x}(t) = (x_1(t), x_2(t), ..., x_n(t)), \tag{A.2}$$

and assume that this system exhibits stable oscillations with period Δ. During oscillation, the trajectory through phase space forms a single closed loop (topologically a circle) embedded in n-dimensional space which attracts nearby trajectories. Assuming that the system remains on this closed cycle, it is possible to fully describe the state through only one variable; the phase of oscillation $\psi \in [0, 2\pi)$. This allows for a reduction from the full n-dimensional system to one dimension [109, 124, 149], viewing $\psi(\mathbf{x})$ as a mapping from a given position in space $\mathbf{x}$ to the angle on cycle such that

$$\frac{d\psi}{dt} = \omega \tag{A.3}$$

where ω is the natural frequency of oscillation, often chosen to be $\omega = 2\pi/\Delta$.
Now consider adding an input to the system in the form of an instantaneous 'kick' called $\delta\mathbf{x}$. This kick is weak enough to not knock the system off cycle, but enough to perturb the system to leave the cycle for a few oscillations before returning. The sensitivity of the system to the kick depends on the current position on cycle and the geometry of the local phase space, which will determine where the system rejoins the cycle compared to an un-perturbed but otherwise identical system. Mathematically, this phase difference can be expressed to first order using a Taylor expansion as follows:

$$\begin{aligned} \psi(\mathbf{x} + \delta\mathbf{x}) &= \psi(\mathbf{x}) + \nabla_x \psi(\mathbf{x}) \cdot ((\mathbf{x} + \delta\mathbf{x}) - \mathbf{x}) + ... \\ \psi(\mathbf{x} + \delta\mathbf{x}) - \psi(\mathbf{x}) &= Q \cdot \delta\mathbf{x} \end{aligned}$$

where the Δ-periodic function $Q = \nabla_x \psi(\mathbf{x})$ describes the sensitivity of the system to perturbation, and is referred to as the *infinitesimal phase response curve* (iPRC). If the system receives the kick at some phase $\psi = \psi^*$, when $Q(\psi^*)$ is positive (negative), then the phase will be advanced (delayed) in response to the kick compared to an identical, unperturbed system.

A.2.1 Coupled phase oscillators

Consider, rather than an instantaneous kick, the n-dimensional system is given some continuous T-periodic forcing $G(\mathbf{x}, t)$, for example an oscillating neuron may be influenced by a pre-synaptic neuron, such that

$$\frac{d\mathbf{x}}{dt} = F(\mathbf{x}) + \varepsilon G(\mathbf{x}, t) \tag{A.4}$$

for some small coupling strength ε. Note also, that the forcing may not necessarily have the same period as the oscillation of the system being forced. The effect on the phase evolution on cycle can be determined using the chain rule:

$$\begin{aligned}\frac{d\psi}{dt} &= \nabla_x \psi \cdot (F(\mathbf{x}) + \varepsilon G(\mathbf{x}, t)) \\ &= Q \cdot F(\mathbf{x}) + \varepsilon Q \cdot G(\mathbf{x}, t) \\ &= \omega + \varepsilon Q \cdot G(\mathbf{x}, t).\end{aligned}$$

This tells us that the evolution of phase on, or near, the periodic orbit is equal to the natural frequency of the oscillator plus any advances or delays in phase due to the weak forcing. The second term in the above equation combines the sensitivity of the system at all points on the cycle with the external forcing to determine the resulting change in phase. Often, this equation can be quite complicated and difficult to analyse, so a further step known as *averaging* can be taken. Here, this term is averaged over a single period of forcing, giving the following simplifying approximation:

$$\frac{d\psi}{dt} \simeq \omega + \varepsilon H(\psi). \tag{A.5}$$

This new function defined as $H(\psi) = \frac{1}{T}\int_0^T Q(\mathbf{x}(\psi)) \cdot G(\mathbf{x}(\psi, s)\, ds$ is the *phase interaction function* (PIF). In a network of coupled oscillators, $H = H(\psi_i, \psi_j)$ is often defined in terms of the phase variables, and describes the influence of the j^{th} oscillator on the i^{th} oscillator.

A.2.2 Kuramoto oscillator

A well known example of a phase oscillator is the Kuramoto model, which is a simplistic example designed to explore synchronisation in large groups of weakly coupled oscillators. A system of n Kuramoto oscillators can be written simply as follows,

$$\frac{d\psi_i}{dt} = \omega_i + \frac{\varepsilon}{n}\sum_{j=1}^{n} \sin(\psi_j - \psi_i), \tag{A.6}$$

where the PIF is chosen to be the sine function of the pairwise difference between phases. By taking the large n limit, Kuramoto re-formulated this system in terms of an *order parameter* $R = \sum_j e^{i\psi_j}$ to elucidate the conditions for spontaneous network synchrony, assuming that the natural frequencies are selected from a Gaussian distribution [109].

A.3 Code availability

The model code is publicly available and can be found at the following address: https://bitbucket.org/leedswormlab/curve-worm-royal-society-paper

A.4 Supplemental movies

Supplemental worm movies can be found at the following address: shorturl.at/jAMPW

with the following contents:

- Movie1a - Crawling on agar
- Movie1b - Worm undulating in environment with intermediate viscosity
- Movie1c - Worm undulating in environment with intermediate viscosity
- Movie1d - Swimming in water
- Movie2a - Uncoordinated locomotion: figure 5.1(d.i)
- Movie2b - Uncoordinated locomotion: figure 5.1(d.ii)
- Movie2c - Uncoordinated locomotion: figure 5.1(d.iii)
- Movie2d - Uncoordinated locomotion: figure 5.1(d.iv)
- Movie3a - Clamping with graded threshold: figure 9.3 (left)
- Movie3b - Clamping with step threshold: figure 9.3 (right)
- Movie4a - Clamping with step threshold and anterior proprioception: figure 9.4 (left)
- Movie4b - Clamping with step threshold and anterior proprioception: figure 9.4 (right)

Bibliography

[1] D. Acemoglu, V. Chernozhukov, I. Werning, and M.D. Whinston. A multi-risk SIR model with optimally targeted lockdown. Technical report, National Bureau of Economic Research, 2020.

[2] A. Albeg, C.J. Smith, M. Chatzigeorgiou, D.G. Feitelson, D.H. Hall, W.R. Schafer, D.M. Miller III, and M. Treinin. C. elegans multi-dendritic sensory neurons: morphology and function. *Molecular and Cellular Neuroscience*, 46(1):308–317, 2011.

[3] Z.F. Altun and D.H. Hall. Wormatlas. *url http://www. wormatlas. org*, 1384, 2002.

[4] L. Avery, C.I. Bargmann, and H.R. Horvitz. The *C. elegans unc-31* gene affects multiple nervous system-controlled functions. *Genetics*, 134(2):455–464, 1993.

[5] A. Azuma. *The biokinetics of flying and swimming.* American Institute of Aeronautics and Astronautics, 2006.

[6] M. Backholm, A.K.S. Kasper, R.D. Schulman, W.S. Ryu, and K. Dalnoki-Veress. The effects of viscosity on the undulatory swimming dynamics of *C. elegans*. *Physics of Fluids*, 27(9):091901, sep 2015.

[7] M. Backholm, W.S. Ryu, and K. Dalnoki-Veress. Viscoelastic properties of the nematode *C. elegans*, a self-similar, shear-thinning worm. *Proceedings of the National Academy of Sciences*, 110(12):4528–4533, 2013.

[8] M. Backholm, W.S. Ryu, and K. Dalnoki-Veress. The nematode *C. elegans* as a complex viscoelastic fluid. *The European Physical Journal E*, 38(5), may 2015.

[9] N.T.J. Bailey et al. *The mathematical theory of infectious diseases and its applications.* Charles Griffin & Company Ltd, 5a Crendon Street, High Wycombe, Bucks HP13 6LE., 1975.

[10] C.I. Bargmann. Genetic and cellular analysis of behavior in C. elegans. *Annual review of neuroscience*, 1993.

[11] C.I. Bargmann. Neurobiology of the *C. elegans* genome. *Science*, 282(5396):2028–2033, 1998.

[12] C.I. Bargmann and E. Marder. From the connectome to brain function. *Nature Methods*, 10(6):483, 2013.

[13] M.W. Berns. Partial cell irradiation with a tunable organic dye laser. *Nature*, 240(5382):483–485, 1972.

[14] S. Berri, J.H. Boyle, M. Tassieri, I.A. Hope, and N. Cohen. Forward locomotion of the nematode *C. elegans* is achieved through modulation of a single gait. *HFSP Journal*, 3(3):186–193, 2009.

[15] A. Borgmann, S.L. Hooper, and A. Büschges. Sensory feedback induced by front-leg stepping entrains the activity of central pattern generators in caudal segments of the stick insect walking system. *Journal of Neuroscience*, 29(9):2972–2983, 2009.

[16] E.S. Boyden, F. Zhang, E. Bamberg, G. Nagel, and K. Deisseroth. Millisecond-timescale, genetically targeted optical control of neural activity. *Nature neuroscience*, 8(9):1263–1268, 2005.

[17] J.H. Boyle. *C. elegans locomotion: an integrated approach*. PhD thesis, University of Leeds, 2009.

[18] J.H. Boyle, S Berri, and N Cohen. Gait modulation in *C. elegans*: an integrated neuromechanical model. *Frontiers in Computational Neuroscience*, 6:10, 2012.

[19] J.H. Boyle and N. Cohen. *C. elegans* body wall muscles are simple actuators. *Biosystems*, 94(1-2):170–181, 2008.

[20] J.H. Boyle, S. Johnson, and A.A. Dehghani-Sanij. Adaptive undulatory locomotion of a C. elegans inspired robot. *IEEE/ASME Transactions on Mechatronics*, 18(2):439–448, 2012.

[21] O.D. Broekmans, J.B. Rodgers, W.S. Ryu, and G.J. Stephens. Resolving coiled shapes reveals new reorientation behaviors in *C. elegans*. *eLife*, 5:e17227, 2016.

[22] A. Brown. *In the Beginning Was the Worm: Finding the Secrets of Life in a Tiny Hermaphrodite*. Simon & Schuster, Limited, 2004.

[23] A.E.X. Brown, E.I. Yemini, L.J. Grundy, T. Jucikas, and W.R. Schafer. A dictionary of behavioral motifs reveals clusters of genes affecting *C. elegans* locomotion. *Proceedings of the National Academy of Sciences*, 110(2):791–796, 2013.

[24] J.A. Bryden and N. Cohen. A simulation model of the locomotion controllers for the nematode *C. elegans*. In *From Animals to Animats 8: Proceedings of the Eighth International Conference on the Simulation of Adaptive Behavior*, pages 183–192. MIT Press, 2004.

[25] J.A. Bryden and N. Cohen. Neural control of *C. elegans* forward locomotion: the role of sensory feedback. *Biological Cybernetics*, 98(4):339–351, 2008.

[26] A.H.J. Burr and C. Gans. Mechanical significance of obliquely striated architecture in nematode muscle. *The Biological Bulletin*, 194(1):1–6, 1998.

[27] A.H.J. Burr and A.F. Robinson. Locomotion behaviour. *Nematode behaviour*, pages 25–62 in R. Guagler, A.L. Bilgrami, eds. Nematode Behaviour. CABL., 2004.

[28] J. Cang and W.O. Friesen. Sensory modification of leech swimming: rhythmic activity of ventral stretch receptors can change intersegmental phase relationships. *Journal of Neuroscience*, 20(20):7822–7829, 2000.

[29] M. Cantarelli, B. Marin, A. Quintana, M. Earnshaw, R. Court, P. Gleeson, S. Dura-Bernal, R.A. Silver, and G. Idili. Geppetto: a reusable modular open platform for exploring neuroscience data and models. *Philosophical Transactions of the Royal Society of London B: Biological Sciences*, 373(1758), 2018.

[30] S.H. Chalasani, N. Chronis, M. Tsunozaki, J.M. Gray, D. Ramot, M.B. Goodman, and C.I. Bargmann. Dissecting a circuit for olfactory behaviour in *C. elegans*. *Nature*, 450(7166):63–70, 2007.

[31] M. Chalfie, J.E. Sulston, J.G. White, E. Southgate, J.N. Thomson, and S. Brenner. The neural circuit for touch sensitivity in *C. elegans*. *Journal of Neuroscience*, 5(4):956–964, 1985.

[32] M. Chalfie, Y. Tu, G. Euskirchen, W.W. Ward, and D.C. Prasher. Green fluorescent protein as a marker for gene expression. *Science*, 263(5148):802–805, 1994.

[33] B.L. Chen, D.H. Hall, and D.B. Chklovskii. Wiring optimization can relate neuronal structure and function. *Proceedings of the National Academy of Sciences*, 103(12):4723–4728, 2006.

[34] N. Chronis, M. Zimmer, and C.I. Bargmann. Microfluidics for in vivo imaging of neuronal and behavioral activity in *C. elegans*. *Nature methods*, 4(9):727–731, 2007.

[35] N. Cohen and J.H. Boyle. Swimming at low reynolds number: a beginners guide to undulatory locomotion. *Contemporary Physics*, 51(2):103–123, 2010.

[36] N. Cohen and J.E. Denham. Whole animal modeling: piecing together nematode locomotion. *Current Opinion in Systems Biology*, 13:150–160, 2019.

[37] N. Cohen and T. Ranner. A new computational method for a model of *C. elegans* biomechanics: Insights into elasticity and locomotion performance. *arXiv e-prints 1702.04988*, url https://arxiv.org/abs/1702.04988, 2017.

[38] N. Cohen and T. Sanders. Nematode locomotion: dissecting the neuronal–environmental loop. *Current Opinion in Neurobiology*, 25:99–106, 2014.

[39] K.S. Cole. Dynamic electrical characteristics of the squid axon membrane. *Archives des sciences physiologiques*, 3(2):253–258, 1949.

[40] K.M. Collins, A. Bode, R.W. Fernandez, J.E. Tanis, J.C. Brewer, M.S. Creamer, and M.R. Koelle. Activity of the *C. elegans* egg-laying behavior circuit is controlled by competing activation and feedback inhibition. *eLife*, 5:e21126, 2016.

[41] L. Conforti and N. Sperelakis. *The patch-clamp technique for measurement of K+ channels in Xenopus oocytes and mammalian expression systems.* Springer, 2001.

[42] International Human Genome Sequencing Consortium et al. Finishing the euchromatic sequence of the human genome. *Nature*, 431(7011):931, 2004.

[43] I. Cooper, A. Mondal, and C.G. Antonopoulos. A SIR model assumption for the spread of COVID-19 in different communities. *Chaos, Solitons & Fractals*, 139:110057, 2020.

[44] G.N. Cox, M. Kusch, and R.S. Edgar. Cuticle of *C. elegans*: its isolation and partial characterization. *The Journal of cell biology*, 90(1):7–17, 1981.

[45] K. Deisseroth. Optogenetics. *Nature methods*, 8(1):26–29, 2011.

[46] L. Deng, J.E. Denham, C. Arya, O. Yuval, N. Cohen, and G. Haspel. Inhibition underlies fast undulatory locomotion in *C. elegans*. *Eneuro*, 2020.

[47] J.E. Denham, T. Ranner, and N. Cohen. Signatures of proprioceptive control in *C. elegans* locomotion. *Philosophical Transactions of the Royal Society of London B: Biological Sciences*, 373(1758):20180208, 2018.

[48] J.C. Doll, N. Harjee, N. Klejwa, R. Kwon, S.M. Coulthard, B. Petzold, M.B. Goodman, and B.L. Pruitt. Su-8 force sensing pillar arrays for biological measurements. *Lab on a Chip*, 9(10):1449–1454, 2009.

[49] J.L. Donnelly, C.M. Clark, A.M. Leifer, J.K. Pirri, M. Haburcak, M.M. Francis, A.D.T. Samuel, and M.J. Alkema. Monoaminergic orchestration of motor programs in a complex *C. elegans* behavior. *PLoS Biology*, 11(4):e1001529, 2013.

[50] J. Duysens and H.W.A.A. Van de Crommert. Neural control of locomotion; part 1: The central pattern generator from cats to humans. *Gait & posture*, 7(2):131–141, 1998.

[51] F.J. Eisenhart, T.W. Cacciatore, and W.B. Kristan Jr. A central pattern generator underlies crawling in the medicinal leech. *Journal of Comparative Physiology A*, 186(7-8):631–643, 2000.

[52] Erdös, P. and Niebur, E. The neural basis of the locomotion of nematodes. In *Statistical Mechanics of Neural Networks*, pages 253–267. Springer, 1990.

[53] B. Esmaeili, J.M. Ross, C. Neades, D.M. Miller, and J. Ahringer. The *C. elegans* even-skipped homologue, *vab-7*, specifies db motoneurone identity and axon trajectory. *Development*, 129(4):853–862, 2002.

[54] C.L. Essmann, D. Martinez-Martinez, R. Pryor, K-Y Leung, K.B. Krishnan, P.P. Lui, N.D.E. Greene, A.E.X. Brown, V.M. Pawar, M.A. Srinivasan, et al. Mechanical properties measured by atomic force microscopy define health biomarkers in ageing *C. elegans*. *Nature communications*, 11(1):1–16, 2020.

[55] C. Fang-Yen, M. Wyart, J. Xie, R. Kawai, T. Kodger, S. Chen, Q. Wen, and A.D.T. Samuel. Biomechanical analysis of gait adaptation in the nematode *C. elegans*. *Proceedings of the National Academy of Sciences USA*, 107(47):20323–20328, 2010.

[56] S. Faumont, G. Rondeau, T.R. Thiele, K.J. Lawton, K.E. McCormick, M. Sottile, O. Griesbeck, E.S. Heckscher, W.M. Roberts, C.Q. Doe, et al. An image-free opto-mechanical system for creating virtual environments and imaging neuronal activity in freely moving *C. elegans*. *PloS one*, 6(9), 2011.

[57] W. Fiers, R. Contreras, F. Duerinck, G. Haegeman, D. Iserentant, J. Merregaert, W M. Jou, F. Molemans, A. Raeymaekers, A Van den Berghe, et al. Complete nucleotide sequence of bacteriophage ms2 rna: primary and secondary structure of the replicase gene. *Nature*, 260(5551):500–507, 1976.

[58] C. Fieseler, J. Kunert-Graf, and J.N. Kutz. The control structure of the nematode *C. elegans*: neuro-sensory integration and propioceptive feedback. *Journal of Biomechanics*, 74:1–8, 2018.

[59] A.D. Fouad, S. Teng, J.R. Mark, A. Liu, P. Alvarez-Illera, H. Ji, A. Du, P.D. Bhirgoo, E. Cornblath, S.A. Guan, et al. Distributed rhythm generators underlie *C. elegans* forward locomotion. *eLife*, 7:e29913, 2018.

[60] E. Fuchs, P. Holmes, T. Kiemel, and A. Ayali. Intersegmental coordination of cockroach locomotion: adaptive control of centrally coupled pattern generator circuits. *Frontiers in neural circuits*, 4:125, 2011.

[61] S. Gao, S.A. Guan, A.D. Fouad, J. Meng, T. Kawano, Y-C Huang, Y. Li, S. Alcaire, W. Hung, Y. Lu, et al. Excitatory motor neurons are local oscillators for backward locomotion. *Elife*, 7:e29915, 2018.

[62] S. Gao and M. Zhen. Action potentials drive body wall muscle contractions in *C. elegans*. *Proceedings of the National Academy of Sciences*, 108(6):2557–2562, 2011.

[63] M.B. Gerstein, Z.J. Lu, E.L. Van Nostrand, C. Cheng, B.I. Arshinoff, T. Liu, K.Y. Yip, R. Robilotto, A. Rechtsteiner, K. Ikegami, et al. Integrative analysis of the *C. elegans* genome by the modencode project. *Science*, 330(6012):1775–1787, 2010.

[64] D.D. Ghosh, T. Sanders, S. Hong, L.Y. McCurdy, D.L. Chase, N. Cohen, M.R. Koelle, and M.N. Nitabach. Neural architecture of hunger-dependent multisensory decision making in *C. elegans*. *Neuron*, 92(5):1049–1062, 2016.

[65] W. Gilpin, S. Uppaluri, and C.P. Brangwynne. Worms under pressure: bulk mechanical properties of *C. elegans* are independent of the cuticle. *Biophysical journal*, 108(8):1887–1898, 2015.

[66] J. Gjorgjieva, D. Biron, and G. Haspel. Neurobiology of *C. elegans* locomotion: where do we stand? *Bioscience*, 64(6):476–486, 2014.

[67] P. Gleeson, D. Lung, R. Grosu, R. Hasani, and S.D. Larson. c302: a multiscale framework for modelling the nervous system of *C. elegans*. *Philosophical Transactions of the Royal Society of London B: Biological Sciences*, 373(1758), 2018.

[68] C.F. Glenn, D.K. Chow, L. David, C.A. Cooke, M.S. Gami, W.B. Iser, K.B. Hanselman, I.G. Goldberg, and C.A. Wolkow. Behavioral deficits during early stages of aging in *C. elegans* result from locomotory deficits possibly linked to muscle frailty. *The Journals of Gerontology Series A: Biological Sciences and Medical Sciences*, 59(12):1251–1260, 2004.

[69] A. Goffeau, B.G. Barrell, H. Bussey, R.W. Davis, B. Dujon, H. Feldmann, F. Galibert, J.D. Hoheisel, C. Jacq, M. Johnston, et al. Life with 6000 genes. *Science*, 274(5287):546–567, 1996.

[70] M.B. Goodman and E.M. Schwarz. Transducing touch in Caenorhabditis elegans. *Annual review of physiology*, 65(1):429–452, 2003.

[71] J. Gray and G.J. Hancock. The propulsion of sea-urchin spermatozoa. *Journal of Experimental Biology*, 32(4):802–814, 1955.

[72] J. Gray and H. W. Lissmann. The locomotion of nematodes. *Journal of Experimental Biology*, 41(1):135–154, 1964.

[73] S. Grillner and P. Wallen. Cellular bases of a vertebrate locomotor system–steering, intersegmental and segmental co-ordination and sensory control. *Brain research reviews*, 40(1-3):92–106, 2002.

[74] Z.V. Guo and L. Mahadevan. Limbless undulatory propulsion on land. *Proceedings of the National Academy of Sciences*, 105(9):3179–3184, 2008.

[75] D.H. Hall. The role of gap junctions in the *C. elegans* connectome. *Neuroscience Letters*, 695:12–18, 2017.

[76] G.J. Hancock. The self-propulsion of microscopic organisms through liquids. *Proceedings of the Royal Society of London. Series A. Mathematical and Physical Sciences*, 217(1128):96–121, 1953.

[77] G. Haspel and M.J. O'Donovan. A perimotor framework reveals functional segmentation in the motoneuronal network controlling locomotion in *C. elegans*. *Journal of Neuroscience*, 31(41):14611–14623, 2011.

[78] G. Haspel and M.J. O'Donovan. A connectivity model for the locomotor network of *C. elegans*. *Worm*, 1(2):125–128, 2012.

[79] E.M. Hedgecock and R.L. Russell. Normal and mutant thermotaxis in the nematode Caenorhabditis elegans. *Proceedings of the National Academy of Sciences*, 72(10):4061–4065, 1975.

[80] J.E. Hewitt, R. Laranjeiro, M. Norouzi, R. Ellwood, A. Antebi, N.J. Szewczyk, M. Driscoll, and S.A. Vanapalli. Multi-environment phenotyping of *C. elegans* for robust evaluation of physical performance. *bioRxiv*, 2020.

[81] J.E. Hewitt, A.K. Pollard, L. Lesanpezeshki, C.S. Deane, C.J. Gaffney, T. Etheridge, N.J. Szewczyk, and S.A. Vanapalli. Muscle strength deficiency and mitochondrial dysfunction in a muscular dystrophy model of *C. elegans* and its functional response to drugs. *Disease models & mechanisms*, 11(12), 2018.

[82] A.V. Hill. The heat of activation and the heat of shortening in a muscle twitch. *Proceedings of the Royal Society of London. Series B-Biological Sciences*, 136(883):195–211, 1949.

[83] A. L. Hodgkin and A. F. Huxley. Propagation of electrical signals along giant nerve fibres. *Proceedings of the Royal Society of London B: Biological Sciences*, 140(899):177–183, 1952.

[84] A.M. Horner and B.C. Jayne. The effects of viscosity on the axial motor pattern and kinematics of the African lungfish (*Protopterus annectens*) during lateral undulatory swimming. *Journal of Experimental Biology*, 211(10):1612–1622, 2008.

[85] R.H. Horvitz, S. Brenner, J. Hodgkin, and R.K. Herman. A uniform genetic nomenclature for the nematode *C. elegans*. *Molecular and General Genetics MGG*, 175(2):129–133, 1979.

[86] Y. Iino and K. Yoshida. Parallel use of two behavioral mechanisms for chemotaxis in *C. elegans*. *Journal of Neuroscience*, 29(17):5370–5380, 2009.

[87] A.J. Ijspeert. Central pattern generators for locomotion control in animals and robots: a review. *Neural networks*, 21(4):642–653, 2008.

[88] E.J. Izquierdo and R.D. Beer. An integrated neuromechanical model of steering in *C. elegans*. In *Artificial Life Conference Proceedings 13*, pages 199–206. MIT Press, 2015.

[89] E.J. Izquierdo and R.D. Beer. From head to tail: a neuromechanical model of forward locomotion in *C. elegans*. *Philosophical Transactions of the Royal Society of London B: Biological Sciences*, 373(1758):1–12, 2018.

[90] E.J. Izquierdo and S.R. Lockery. Evolution and analysis of minimal neural circuits for klinotaxis in *C. elegans*. *Journal of Neuroscience*, 30(39):12908–12917, 2010.

[91] T.A. Jarrell, Y. Wang, A.E. Bloniarz, C.A. Brittin, M. Xu, J.N. Thomson, D.G. Albertson, D.H. Hall, and S.W. Emmons. The connectome of a decision-making neural network. *science*, 337(6093):437–444, 2012.

[92] C.L. Johnson, T.J. Lewis, and R.D. Guy. Neuromechanical mechanisms of gait adaptation in *C. elegans*: Relative roles of neural and mechanical coupling. *https://arxiv.org/abs/2006.10122*, 2020.

[93] R.E. Johnson and C.J. Brokaw. Flagellar hydrodynamics. A comparison between resistive-force theory and slender-body theory. *Biophysical journal*, 25(1):113–127, 1979.

[94] I.L. Johnstone. The cuticle of the nematode *C. elegans*: a complex collagen structure. *Bioessays*, 16(3):171–178, 1994.

[95] Y. Kagawa-Nagamura, K. Gengyo-Ando, M. Ohkura, and J. Nakai. Role of tyramine in calcium dynamics of GABAergic neurons and escape behavior in *C. elegans*. *Zoological Letters*, 4(1):19, 2018.

[96] E. Kalogeropoulou. *Role of the SAA and SMB neurons in locomotion in the nematode C. elegans, with a focus on steering*. PhD thesis, University of Leeds, 2018.

[97] H.S. Kaplan, A.L.A. Nichols, and M. Zimmer. Sensorimotor integration in *C. elegans*: a reappraisal towards dynamic and distributed computations. *Philosophical Transactions of the Royal Society of London B: Biological Sciences*, 373(1758), 2018.

[98] J. Karbowski, C.J. Cronin, A. Seah, J.E. Mendel, D. Cleary, and P.W. Sternberg. Conservation rules, their breakdown, and optimality in Caenorhabditis sinusoidal locomotion. *Journal of theoretical biology*, 242(3):652–669, 2006.

[99] J. Karbowski, G. Schindelman, C.J. Cronin, A. Seah, and P.W. Sternberg. Systems level circuit model of *C. elegans* undulatory locomotion: mathematical modeling and molecular genetics. *Journal of Computational Neuroscience*, 24(3):253–276, 2008.

[100] S. Kato, H.S. Kaplan, T. Schrödel, S. Skora, T.H. Lindsay, E. Yemini, S. Lockery, and M. Zimmer. Global brain dynamics embed the motor command sequence of *C. elegans*. *Cell*, 163(3):656–669, 2015.

[101] T. Kawano, M.D. Po, S. Gao, G. Leung, W.S. Ryu, and M. Zhen. An imbalancing act: gap junctions reduce the backward motor circuit activity to bias *C. elegans* for forward locomotion. *Neuron*, 72(4):572–586, 2011.

[102] R. Kerr, V. Lev-Ram, G. Baird, P. Vincent, R.Y. Tsien, and W.R. Schafer. Optical imaging of calcium transients in neurons and pharyngeal muscle of *C. elegans*. *Neuron*, 26(3):583–594, 2000.

[103] O. Kiehn. Development and functional organization of spinal locomotor circuits. *Current opinion in neurobiology*, 21(1):100–109, 2011.

[104] O. Kiehn. Decoding the organization of spinal circuits that control locomotion. *Nature Reviews Neuroscience*, 17(4):224, 2016.

[105] J.S. Kim and M. Kaiser. From *C. elegans* to the human connectome: a specific modular organization increases metabolic, functional and developmental efficiency. *Philosophical Transactions of the Royal Society B*, 369:20130529, 2014.

[106] W.B. Kristan Jr, R.L. Calabrese, and W.O. Friesen. Neuronal control of leech behavior. *Progress in neurobiology*, 76(5):279–327, 2005.

[107] J. Kunert, E. Shlizerman, and J.N. Kutz. Low-dimensional functionality of complex network dynamics: Neurosensory integration in the *C. elegans* connectome. *Physical Review E*, 89(5):052805, 2014.

[108] J.M. Kunert, J.L. Proctor, S.L. Brunton, and J.N. Kutz. Spatiotemporal feedback and network structure drive and encode *C. elegans* locomotion. *PLoS Computational Biology*, 13(1):e1005303, 2017.

[109] Y. Kuramoto. *Chemical oscillations, waves, and turbulence*. Courier Corporation, 2003.

[110] F. Lebois, P. Sauvage, C. Py, O. Cardoso, B. Ladoux, P. Hersen, and J.M. Di Meglio. Locomotion control of *C. elegans* through confinement. *Biophysical Journal*, 102(12):2791–2798, 2012.

[111] R.Y.N. Lee, L. Lobel, M. Hengartner, H.R. Horvitz, and L. Avery. Mutations in the α1 subunit of an L-type voltage-activated Ca2+ channel cause myotonia in Caenorhabditis elegans. *The EMBO journal*, 16(20):6066–6076, 1997.

[112] J.A. Lewis, C-H Wu, H. Berg, and J.H. Levine. The genetics of levamisole resistance in the nematode *C. elegans*. *Genetics*, 95(4):905–928, 1980.

[113] W. Li, Z. Feng, P.W. Sternberg, and X.Z.S. Xu. A *C. elegans* stretch receptor neuron revealed by a mechanosensitive trp channel homologue. *Nature*, 440(7084):684–687, 2006.

[114] W. Li, L. Kang, B.J. Piggott, Z. Feng, and X.Z.S. Xu. The neural circuits and sensory channels mediating harsh touch sensation in *C. elegans*. *Nature communications*, 2(1):1–9, 2011.

[115] J. Lighthill. Flagellar hydrodynamics. *SIAM review*, 18(2):161–230, 1976.

[116] R.J. Linden. *Recent advances in physiology*. Number 9. Churchill Livingstone, 1974.

[117] P. Liu, B. Chen, R. Mailler, and Z-W Wang. Antidromic-rectifying gap junctions amplify chemical transmission at functionally mixed electrical-chemical synapses. *Nature communications*, 8:14818, 2017.

[118] P. Liu, B. Chen, and Z-W Wang. SLO-2 potassium channel is an important regulator of neurotransmitter release in *C. elegans*. *Nature Communications*, 5:5155, 2014.

[119] P. Liu, B. Chen, and Z-W. Wang. Gabaergic motor neurons bias locomotor decision-making in *C. elegans*. *Nature communications*, 11(1):1–19, 2020.

[120] S.R. Lockery, K.J. Lawton, J.C. Doll, S. Faumont, S.M. Coulthard, T.R. Thiele, N. Chronis, K.E. McCormick, M.B. Goodman, and B.L. Pruitt. Artificial dirt: microfluidic substrates for nematode neurobiology and behavior. *Journal of Neurophysiology*, 99(6):3136–3143, 2008.

[121] K. Lüersen, D-C Gottschling, and F. Döring. Complex locomotion behavior changes are induced in *C. elegans* by the lack of the regulatory leak K+ channel TWK-7. *Genetics*, 204(2):683–701, 2016.

[122] L. Luo, C.V. Gabel, H-I Ha, Y. Zhang, and A.D.T. Samuel. Olfactory behavior of swimming *C. elegans* analyzed by measuring motile responses to temporal variations of odorants. *Journal of neurophysiology*, 99(5):2617–2625, 2008.

[123] T. Majmudar, E.E. Keaveny, J. Zhang, and M.J. Shelley. Experiments and theory of undulatory locomotion in a simple structured medium. *Journal of The Royal Society Interface*, page rsif20110856, 2012.

[124] I.G. Malkin. *Some problems in the theory of nonlinear oscillations*, volume 1. US Atomic Energy Commission, Technical Information Service, 1959.

[125] A. Marck, G. Berthelot, V. Foulonneau, A. Marc, J. Antero-Jacquemin, P. Noirez, A.M. Bronikowski, T.J. Morgan, T. Garland Jr, P.A. Carter, et al. Age-related changes in locomotor performance reveal a similar pattern for *C. elegans*, mus domesticus, canis familiaris, equus caballus, and homo sapiens. *Journals of Gerontology Series A: Biomedical Sciences and Medical Sciences*, 72(4):455–463, 2017.

[126] E. Marder, D. Bucher, D.J. Schulz, and A.L. Taylor. Invertebrate central pattern generation moves along. *Current Biology*, 15(17):R685–R699, 2005.

[127] H. Markram. The blue brain project. *Nature Reviews Neuroscience*, 7(2):153, 2006.

[128] G. Marmont. Studies on the axon membrane. i. a new method. *Journal of cellular and comparative physiology*, 34(3):351–382, 1949.

[129] P.D. McClanahan, J.H. Xu, and C. Fang-Yen. Comparing *C. elegans* gentle and harsh touch response behavior using a multiplexed hydraulic microfluidic device. *Integrative Biology*, 9(10):800–809, 2017.

[130] P.W. McDonald, S.L. Hardie, T.N. Jessen, L. Carvelli, D.S. Matthies, and R.D. Blakely. Vigorous motor activity in *C. elegans* requires efficient clearance of dopamine mediated by synaptic localization of the dopamine transporter dat-1. *Journal of Neuroscience*, 27(51):14216–14227, 2007.

[131] S.L. Mclntire, E. Jorgensen, and H.R. Horvitz. Genes required for GABA function in *C. elegans*. *Nature*, 364(6435):334–337, 1993.

[132] S.L. Mclntire, E. Jorgensen, J. Kaplan, and H.R. Horvitz. The GABAergic nervous system of *C. elegans*. *Nature*, 364(6435):337–341, 1993.

[133] J.E. Mellem, P.J. Brockie, D.M. Madsen, and A.V. Maricq. Action potentials contribute to neuronal signaling in *C. elegans*. *Nature Neuroscience*, 11(8):865, 2008.

[134] D. Meunier, R. Lambiotte, and E.T. Bullmore. Modular and hierarchically modular organization of brain networks. *Frontiers in Neuroscience*, 4:200, 2010.

[135] O.J. Mullins, J.T. Hackett, J.T. Buchanan, and W.O. Friesen. Neuronal control of swimming behavior: comparison of vertebrate and invertebrate model systems. *Progress in neurobiology*, 93(2):244–269, 2011.

[136] E. Neher, B. Sakmann, and J.H. Steinbach. The extracellular patch clamp: a method for resolving currents through individual open channels in biological membranes. *Pflügers Archiv*, 375(2):219–228, 1978.

[137] E. Niebur and P. Erdös. Theory of the locomotion of nematodes: dynamics of undulatory progression on a surface. *Biophysical journal*, 60(5):1132–1146, 1991.

[138] E. Niebur and P. Erdös. Theory of the locomotion of nematodes: control of the somatic motor neurons by interneurons. *Math. Biosci.*, 118(1):51–82, 1993.

[139] E.O. Olivares, E.J. Izquierdo, and R.D. Beer. Potential role of a ventral nerve cord central pattern generator in forward and backward locomotion in *C. elegans*. *Network Neuroscience*, 2(3):323–343, 2018.

[140] A. Palyanov, S. Khayrulin, and S.D. Larson. Application of smoothed particle hydrodynamics to modeling mechanisms of biological tissue. *Advances in Engineering Software*, 98:1–11, 2016.

[141] A. Palyanov, S. Khayrulin, and S.D. Larson. Three-dimensional simulation of the *C. elegans* body and muscle cells in liquid and gel environments for behavioural analysis. *Philosophical Transactions of the Royal Society of London B: Biological Sciences*, 373(1758), 2018.

[142] S-J Park, M.B. Goodman, and B.L. Pruitt. Analysis of nematode mechanics by piezoresistive displacement clamp. *Proceedings of the National Academy of Sciences*, 104(44):17376–17381, 2007.

[143] L. Pereira, P. Kratsios, E. Serrano-Saiz, H. Sheftel, A.E. Mayo, D.H. Hall, J.G. White, B. LeBoeuf, L.R. Garcia, U. Alon, and O. Hobert. A cellular and regulatory map of the cholinergic nervous system of *C. elegans*. *eLife*, 4:e12432, 2015.

[144] C.I. Petersen, T.R. McFarland, S.Z. Stepanovic, P. Yang, D.J. Reiner, K. Hayashi, A.L. George, D.M. Roden, J.H. Thomas, and J.R. Balser. In vivo identification of genes that modify ether-a-go-go-related gene activity in *C. elegans* may also affect human cardiac arrhythmia. *Proceedings of the National Academy of Sciences*, 101(32):11773–11778, 2004.

[145] B.C. Petzold, S-J Park, E.A. Mazzochette, M.B. Goodman, and B.L. Pruitt. Mems-based force-clamp analysis of the role of body stiffness in *C. elegans* touch sensation. *Integrative Biology*, 5(6):853–864, 2013.

[146] Petzold, B.C. and Park, S-J and Ponce, P. and Roozeboom, C. and Powell, C. and Goodman, M.B. and Pruitt, B.L. *C. elegans* body mechanics are regulated by body wall muscle tone. *Biophysical Journal*, 100(8):1977–1985, Apr 2011.

[147] J.T. Pierce-Shimomura, B.L. Chen, J.J. Mun, R. Ho, R. Sarkis, and S.L. McIntire. Genetic analysis of crawling and swimming locomotory patterns in *C. elegans*. *Proceedings of the National Academy of Sciences USA*, 105(52):20982—20987, 2008.

[148] B.J. Piggott, J. Liu, Z. Feng, S.A. Wescott, and X.Z.S. Xu. The neural circuits and synaptic mechanisms underlying motor initiation in *C. elegans*. *Cell*, 147(4):922–933, 2011.

[149] A. Pikovsky, J. Kurths, M. Rosenblum, and J. Kurths. *Synchronization: a universal concept in nonlinear sciences*, volume 12. Cambridge university press, 2003.

[150] J.N. Pitt, N.L. Strait, E.M. Vayndorf, B.W. Blue, C.H. Tran, B.E.M. Davis, K. Huang, B.J. Johnson, K.M. Lim, S. Liu, et al. Wormbot, an open-source robotics platform for survival and behavior analysis in C. elegans. *GeroScience*, 41(6):961–973, 2019.

[151] A.A. Prinz, D. Bucher, and E. Marder. Similar network activity from disparate circuit parameters. *Nature Neuroscience*, 7:1345–1352, 2004.

[152] E.M. Purcell. Life at low Reynolds number. *American journal of physics*, 45(1):3–11, 1977.

[153] M. Rahman, J.E. Hewitt, F. Van-Bussel, H. Edwards, J. Blawzdziewicz, N.J. Szewczyk, M. Driscoll, and S.A. Vanapalli. Nemaflex: a microfluidics-based technology for standardized measurement of muscular strength of *C. elegans*. *Lab on a Chip*, 18(15):2187–2201, 2018.

[154] T. Ranner. A stable finite element method for low inertia undulatory locomotion in three dimensions. *Applied Numerical Mathematics*, 156:422–455, 2020.

[155] J.E. Richmond and E.M. Jorgensen. One GABA and two acetylcholine receptors function at the *C. elegans* neuromuscular junction. *Nature neuroscience*, 2(9):791–797, 1999.

[156] M. Rönkkö and G. Wong. Modeling the *C. elegans* nematode and its environment using a particle system. *Journal of theoretical biology*, 253(2):316–322, 2008.

[157] B. Sakmann and E. Neher. Patch clamp techniques for studying ionic channels in excitable membranes. *Annual review of physiology*, 46(1):455–472, 1984.

[158] G.P. Sarma, C.W. Lee, T. Portegys, V. Ghayoomie, T. Jacobs, B. Alicea, M. Cantarelli, M. Currie, R.C. Gerkin, S. Gingell, et al. Openworm: overview and recent advances in integrative biological simulation of *C. elegans*. *Philosophical Transactions of the Royal Society B: Biological Sciences*, 373(1758):20170382, 2018.

[159] P. Sauvage. *Etude de la locomotion chez C. elegans et perturbations mecaniques du mouvement*. PhD thesis, PhD dissertation, Laboratoire Matiere et Systemes Compiexes (Paris, France, 2007.

[160] K. Schuske, A.A. Beg, and E.M. Jorgensen. The GABA nervous system in *C. elegans*. *Trends in neurosciences*, 27(7):407–414, 2004.

[161] D.D. Shaye and I. Greenwald. Ortholist: a compendium of *C. elegans* genes with human orthologs. *PloS one*, 6(5):e20085, 2011.

[162] R.N. Singh and J.E. Sulston. Some observations on moulting in Caenorhabditis elegans. *Nematologica*, 24(1):63–71, 1978.

[163] L. Stein, P. Sternberg, R. Durbin, J. Thierry-Mieg, and J. Spieth. Wormbase: network access to the genome and biology of *C. elegans*. *Nucleic acids research*, 29(1):82–86, 2001.

[164] G.J. Stephens, B. Johnson-Kerner, W. Bialek, and W.S. Ryu. Dimensionality and dynamics in the behavior of *C. elegans*. *PLoS Computational Biology*, 4(4):e1000028, 2008.

[165] A.O.W. Stretton, R.E. Davis, J.D. Angstadt, J.E. Donmoyer, and C.D. Johnson. Neural control of behaviour in ascaris. *Trends in Neurosciences*, 8:294–300, 1985.

[166] J.E. Sulston. Neuronal cell lineages in the nematode Caenorhabditis elegans. In *Cold Spring Harbor symposia on quantitative biology*, volume 48, pages 443–452. Cold Spring Harbor Laboratory Press, 1983.

[167] J.E. Sulston and H.R. Horvitz. Post-embryonic cell lineages of the nematode, Caenorhabditis elegans. *Developmental biology*, 56(1):110–156, 1977.

[168] J.E. Sulston, E. Schierenberg, J.G. White, and J.N. Thomson. The embryonic cell lineage of the nematode *C. elegans*. *Developmental Biology*, 100(1):64 – 119, 1983.

[169] J. Sznitman, P.K. Prashant, P. Krajacic, T. Lamitina, and P.E. Arratia. Material properties of *C. elegans* swimming at low Reynolds number. *Biophysical Journal*, 98(4):617–626, 2010.

[170] J. Sznitman, P.K. Purohit, P. Krajacic, T. Lamitina, and P.E. Arratia. Material Properties of *C. elegans* Swimming at Low Reynolds Number. *Biophysical Journal*, 98:617–626, 2010.

[171] G.I. Taylor. Analysis of the swimming of microscopic organisms. *Proceedings of the Royal Society of London. Series A. Mathematical and Physical Sciences*, 209(1099):447–461, 1951.

[172] G.I. Taylor. Analysis of the swimming of long and narrow animals. *Proceedings of the Royal Society of London. Series A. Mathematical and Physical Sciences*, 214(1117):158–183, 1952.

[173] O. Tolstenkov, P. Van der Auwera, W.S. Costa, O. Bazhanova, T.M. Gemeinhardt, A.C.F. Bergs, and A. Gottschalk. Functionally asymmetric motor neurons contribute to coordinating locomotion of *C. elegans*. *Elife*, 7:e34997, 2018.

[174] E.K. Towlson, P.E. Vértes, S.E. Ahnert, W.R. Schafer, and E.T. Bullmore. The rich club of the *C. elegans* neuronal connectome. *Journal of Neuroscience*, 33(15):6380–6387, 2013.

[175] E.K. Towlson, P.E. Vértes, G. Yan, Y.L. Chew, D.S. Walker, W.R. Schafer, and A.L. Barabási. *C. elegans* and the network control framework–FAQs. *Philosophical Transactions of the Royal Society of London B: Biological Sciences*, 373(1758):20170372, 2018.

[176] E.L. Tsalik and O.H. Hobert. Functional mapping of neurons that control locomotory behavior in *C. elegans*: mathematical modeling and molecular genetics. *Journal of Neurobiology*, 56(2):178–197, 2003.

[177] E.D. Tytell, C-Y Hsu, T.L. Williams, A.H. Cohen, and L.J. Fauci. Interactions between internal forces, body stiffness, and fluid environment in a neuromechanical model of lamprey swimming. *Proceedings of the National Academy of Sciences USA*, 107(46):19832–19837, 2010.

[178] M.P. van den Heuvel and O. Sporns. Rich-club organization of the human connectome. *Journal of Neuroscience*, 31(44):15775–15786, 2011.

[179] L.R. Varshney, B.L. Chen, E. Paniagua, D.H. Hall, and D.B. Chklovskii. Structural properties of the *C. elegans* neuronal network. *PLoS Computational Biology*, 7(2):e1001066, 2011.

[180] T. Wakabayashi, I. Kitagawa, and R. Shingai. Neurons regulating the duration of forward locomotion in *C. elegans*. *Neuroscience research*, 50(1):103–111, 2004.

[181] H.R. Wallace. Movement of eelworms: I. the influence of pore size and moisture content of the soil on the migration of larvae of the beet eelworm, Heterodera schachtii schmidt. *Annals of applied Biology*, 46(1):74–85, 1958.

[182] H.R. Wallace. Wave formation by infective larvae of the plant parasitic nematode *Meloidogyne javanica*. *Nematologica*, 15(1):65–75, 1969.

[183] A. Ward, J. Liu, Z. Feng, and X.Z.S. Xu. Light-sensitive neurons and channels mediate phototaxis in C. elegans. *Nature neuroscience*, 11(8):916–922, 2008.

[184] S. Ward. Chemotaxis by the nematode *C.* elegans: identification of attractants and analysis of the response by use of mutants. *Proceedings of the National Academy of Sciences USA*, 70(3):817–821, 1973.

[185] S. Ward and J.S. Carrel. Fertilization and sperm competition in the nematode *C. elegans*. *Developmental biology*, 73(2):304–321, 1979.

[186] D. Watts and S. Strogatz. An undirected, unweighted network representing the topology of the western states power grid of the united states. *Nature*, 393:440–442, 1998.

[187] J.C. Weeks. Neuronal basis of leech swimming: separation of swim initiation, pattern generation, and intersegmental coordination by selective lesions. *Journal of Neurophysiology*, 45(4):698–723, 1981.

[188] Q. Wen, M.D. Po, E. Hulme, S. Chen, X. Liu, S.W. Kwok, M. Gershow, A.M. Leifer, V. Butler, and C. Fang-Yen. Proprioceptive coupling within motor neurons drives *C. elegans* forward locomotion. *Neuron*, 76(4):750–761, 2012.

[189] P.D. Wes and C.I. Bargmann. *C. elegans* odour discrimination requires asymmetric diversity in olfactory neurons. *Nature*, 410(6829):698–701, 2001.

[190] J.G. White, E. Southgate, J.N. Thomson, and S. Brenner. The structure of the ventral nerve cord of *C. elegans*. *Philosophical Transactions of the Royal Society of London B: Biological Sciences*, 275:327–348, 1976.

[191] J.G. White, E. Southgate, J.N. Thomson, and S. Brenner. The structure of the nervous system of the nematode *C. elegans*. *Philosophical Transactions of the Royal Society of London B: Biological Sciences*, 314:1–340, 1986.

[192] J.Q. White, T.J. Nicholas, J. Gritton, L. Truong, E.R. Davidson, and E.M. Jorgensen. The sensory circuitry for sexual attraction in C. elegans males. *Current Biology*, 17(21):1847–1857, 2007.

[193] S.R. Wicks, C.J. Roehrig, and C.H. Rankin. A dynamic network simulation of the nematode tap withdrawal circuit: predictions concerning synaptic function using behavioral criteria. *Journal of Neuroscience*, 16(12):4017–4031, 1996.

[194] T. Xu, J. Huo, S. Shao, M. Po, T. Kawano, Y. Lu, M. Wu, M. Zhen, and Q. Wen. Descending pathway facilitates undulatory wave propagation in *C. elegans* through gap junctions. *Proceedings of the National Academy of Sciences USA*, 115(19):E4493–E4502, 2018.

[195] G. Yan, P.E. Vértes, E.K. Towlson, Y.L. Chew, D.S. Walker, W.R. Schafer, and A.L. Barabási. Network control principles predict neuron function in the *C. elegans* connectome. *Nature*, 550(7677):519, 2017.

[196] M.F. Yanik, H. Cinar, H.N. Cinar, A.D. Chisholm, Y. Jin, and A. Ben-Yakar. Functional regeneration after laser axotomy. *Nature*, 432(7019):822–822, 2004.

[197] E. Yemini, T. Jucikas, L.J. Grundy, A.E.X. Brown, and Schafer W.R. A database of *C. elegans* behavioral phenotypes. *Nature Methods*, 10:877–879, 2013.

[198] M. Zhen and A.D.T. Samuel. *C. elegans* locomotion: small circuits, complex functions. *Current opinion in neurobiology*, 33:117–126, 2015.